Automated Peripheral Sensory Neuropathy Assessment of Diabetic Patients Using Optical Imaging and Binary Processing Techniques

A thesis submitted in partial fulfilment of the requirements for the Degree of Doctor of Philosophy

BY

Hafeez Ur Rehman Siddiqui

Student ID 2720024

Supervised by

Dr Sandra Dudley

School of Engineering, London South Bank University

January, 2016

DECLARATION

I hereby declare that the content presented in this dissertation, except where references are given, is original and has not been submitted in whole or in part for consideration for any other degree or qualification awarded by an institution other than this university (London South Bank University).

DEDICATION

I would like to dedicate this thesis to my teachers and especially Dr. Sandra Dudley, whose support, encouragement and guidance enabled me to complete it.

ACKNOWLEDGEMENTS

First and foremost, I would say **Alhamdulillah** "Praise be to God". I would like to offer my sincere thanks to my parents for their continuous support and to London South Bank University for sponsoring my PhD. I would also like to extend my gratitude to Director of Research Dr Sandra Dudley for her timely suggestions, coordination and persistent supervision. I would additionally like to thank Dr Steve Alty and Dr Michelle Spruce for their support.

Finally, I must thank all of my colleagues for their valuable encouragement and moral support.

CONTENTS

CONTENTS

CONTENTS

LIST OF FIGURES

LIST OF FIGURES

LIST OF FIGURES

LIST OF TABLES

PROJECT STATUS

- *University patent has been lodged.*
- *One conference paper has been presented and published by IEEE (January 2013).*
  "Automated peripheral neuropathy assessment of diabetic patients using optical imaging and binary processing techniques"
- *A journal paper has been published to IEEE (October 2014).*
  "Automated Peripheral Neuropathy Assessment Using Optical Imaging and Foot Anthropometry"
- *A second IEEE conference paper has been presented and published (April 2015).*
  "Automated Semmes Weinstein monofilament examination replication using optical imaging and mechanical probe assembly"
- *A second journal paper has been submitted to IEEE Transactions on Biomedical Circuits and Systems*
- *Another journal paper has been written and u der review*

ABSTRACT

A large proportion of individuals who live with type2 diabetes suffer from plantar sensory neuropathy (PSN). Regular testing and assessment for the condition is required to avoid ulceration or other damage to patients' feet. Currently accepted practice involves a trained podiatrist testing patients' feet manually with a hand-held nylon monofilament probe. The procedure is time consuming and labour intensive, requires training, is susceptible to error and is difficult to repeat.

This thesis presents the first investigation into a novel automated approach to automatically identify the pressure points on a given patient's foot for the examination of sensory neuropathy via optical image processing via RGB and HSV colour space incorporating plantar anthropometry. The developed system effectively automates the traditional Semmes–Weinstein monofilament examination (SWME).

Further work presented demonstrates the development and demonstration of a generic automated lesion detection algorithms to recognise and avoid probe application on a plantar surface. A combination of local binary pattern and support vector machine methods in layered combination are used to avoid probe application where lesion and chosen pressure points overlap. The trained lesion detection and avoidance method was 100% effective on the lesions used.

ABSTRACT

CHAPTER 1. Introduction

Diabetes is a common metabolic disorder and may lead to different complications, such as heart disease, kidney failure, dementia, retinopathy, neuropathy and limb amputation, if not properly treated and self-managed. Diabetes is concomitant with disability and death through its associated complications such as kidney disease, blindness and cardiovascular disease, as well as through the development of chronic wounds, especially the diabetic foot ulcer (DFU) and diabetic peripheral neuropathy [1].

This thesis presents the first investigation into a novel automated approach to automatically identify the pressure points on a given patient's foot for the examination of sensory neuropathy via optical image processing via RGB and HSV colour space incorporating plantar anthropometry. The developed system effectively automates the traditional Semmes–Weinstein monofilament examination (SWME).

Further work presented demonstrates the development and demonstration of a generic automated lesion detection algorithms to recognise and avoid probe application on a plantar surface. A combination of local binary pattern and support vector machine methods in layered combination are used to avoid probe application where lesion and chosen pressure points overlap. The trained lesion detection and avoidance method was 100% effective on the lesions used.

The Thesis structured as follows

Chapter 1 discusses Diabetes and one of its complications namely Peripheral Sensor Neuropathy (PSN), its assessment techniques and high plantar pressure areas. Chapter 2 covers flaws in existing Semmes Weinstein Monofilament Examination (SWME), a semi mechanical approach to exercise SWME, plantar pressure measuring devices and optical image processing background. Chapter 3 discusses the proposed system architecture and the first algorithm to select suitable pressure test point using optical imaging and binary processing technique. Chapter 4 presents improved algorithms using foot stopper and subsequently using sectorisation and foot anthropometry. Chapter 5 discusses the methodology to avoid plantar lesion to be probed using

the combination of Local Binary Pattern (LBP) and Support Vector Machine (SVM). The PerSeNT evaluation in terms of efficiency and accuracy by comparing PerSeNT with a trained podiatrist and with commercial pressure plate and signal detection theory followed by test-retest Pearson coefficient reliability are discussed in chapter 6. Chapter 7 end the thesis with conclusion and chapter 8 contains appendix.

The contribution and achievements are given below

1. A University patent has been lodged.
2. "Automated Peripheral Neuropathy Assessment of Diabetic Patients using Optical Imaging and Binary Processing Techniques", Hafeez U. R. Siddiqui Michelle Spruce, Stephen R. Alty, Sandra Dudley, International IEEE Conference on IEEE Point-of-Care Healthcare Technologies (PHT) Bangalore, India, 16 - 18 January, 2013.
3. "Automated Peripheral Neuropathy Assessment Using Optical Imaging and Foot Anthropometry", Hafeez U. R. Siddiqui Michelle Spruce, Stephen R. Alty, Sandra Dudley, IEEE Transactions on Biomedical Engineering (Volume:62 , Issue: 8) Page(s):1911 – 1917, 24 February 2015 DOI: 10.1109/TBME.2015.2407056
4. "Automated Semmes Weinstein monofilament examination replication using optical imaging and mechanical probe assembly", Hafeez U. R. Siddiqui Michelle Spruce, Stephen R. Alty, Sandra Dudley, Biomedical Imaging (ISBI), 2015 IEEE 12th International Symposium on, New York, 16-19 April 2015, pp. 552 – 555, DOI: 10.1109/ISBI.2015.7163933.
5. "Plantar Surface Lesion Avoidance using LBP and SVM for Automated Peripheral Neuropathy Assessment Techniques", Hafeez-Ur-Rehman. Siddiqui, Sandra Dudley, IEEE Transactions on Biomedical Circuits and Systems (submitted).
6. "PerSenT Performance Evaluation", Hafeez-Ur-Rehman. Siddiqui, Russo Riccardo, Sandra E. Dudley. (under review).

1.1 The Diabetic Epidemic

Diabetes is a major health challenge currently affecting more than 8% of the population of the developed world, with much higher growth rates in developing countries such as China and India. The prevalence of diabetes in adults within the 20–79 age range was estimated at 382 million worldwide for 2012 and it is expected to affect 592 million people by 2035 [2].

It is assessed that 175 million people have undiagnosed type 2 diabetes. According to the International Diabetes Federation (IDF), in 2013 five countries had more than 10 million people with diabetes: China, India, the United States of America, Brazil, and the Russian Federation [2]. The statistics are shown graphically in Figure 1 and 2.

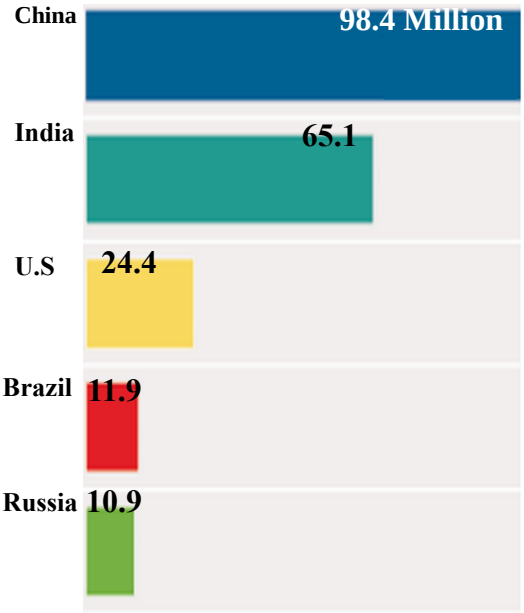

Figure 2: *Top five countries by number of people with diabetes in 2013 aged 20 to 79 [2]*

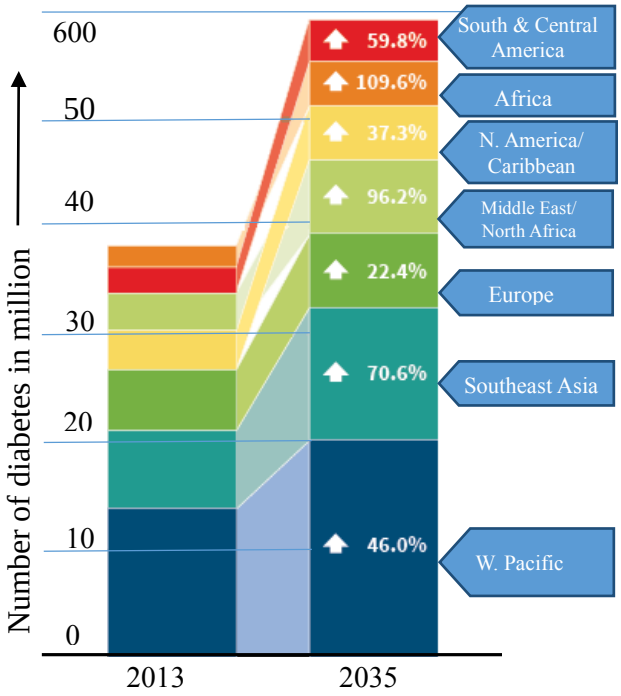

Figure 1: *Current and projected cases of diabetes by region [2]*

Further, the report showed that in 2013 the 10 countries with the highest diabetes prevalence in the adult population were Tokelau (37.5%), Micronesia, Marshall Islands, Kiribati, Cook Islands, Vanuatu, Saudi Arabia, Nauru, Kuwait and Qatar (22.9%). Diabetes affects people in both urban and rural settings worldwide, with 64% of cases in urban areas and 36% in rural areas [2].

Roughly 27 million diabetics are registered in Europe alone and the majority of these individuals,

around half of whom are aged 60 or over (>80%), present with type2 diabetes. It is estimated that more than one in 17 people in the UK have diabetes (diagnosed or undiagnosed). It is estimated that there are around 630,000 people in the UK who have diabetes but have not been diagnosed [2].

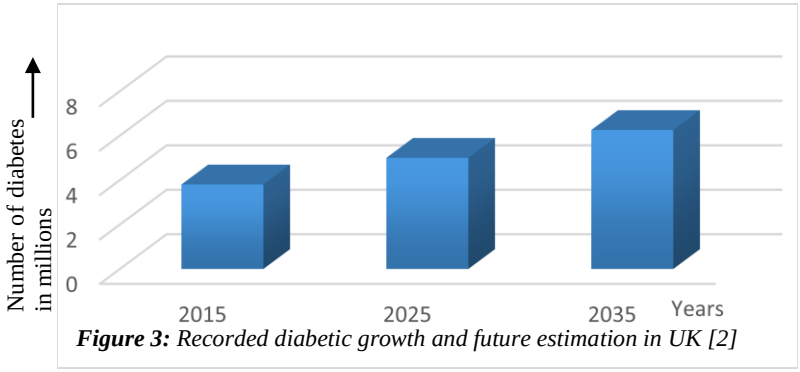

Figure 3: *Recorded diabetic growth and future estimation in UK [2]*

In the UK there are currently approximately 3.8 million people living with diabetes and that number will reach five million by 2025[2] and potentially 6.25 million by 2035/36.

This is equivalent to:

- More than 400 people every day (410)
- Over 17 people every hour (17.12)
- Around three people every 10 minutes (2.85)

The Department of Health estimates that up to 24,000 people with diabetes are dying each year from causes that could be avoided through better management of their condition [3]. Diabetes causes one death every six seconds globally, and is responsible for 8.4% of all global mortality in the 20–79 age group. 48% of deaths occur in those under 60 years of age [2].

This projected increase is likely to have a significant impact on the National Health Service's (NHS) resources. Of course, this is not simply a UK problem, since it is an enormous global issue.

1.2 Neuropathy

Peripheral sensory neuropathy (PSN) is one the many complications of type2 diabetes that affects the peripheral extremities of the body. Typically, around 60% of all type2 diabetics will develop

this condition within 10 years of being first diagnosed.

It manifests as sharp, shooting pain, burning, tingling, a feeling of being pricked with pins, throbbing and numbness in extremities [4]. PSN is commonly regarded as a key factor in the development of ulcerations. It is often termed stocking-glove neuropathy, damaging the longest nerves before progressing proximally [5]. In such a condition, the central nerves wouldn't know what's happening at extremities; this is more often the case in patients with long-standing diabetes [6]. Controlling the blood glucose level is considered key to minimising the risk of neuropathy development and its severity [2]. Neuropathy may affect up to 50% of diabetic sufferers [2].

The frequency of diabetic neuropathies is noticeably increasing with the enormous growth of type2 diabetes, but the actual number remains undisclosed [1]. The statistics are recorded variably in reports on diabetic patients, depending mostly on the criteria and methods used to identify neuropathy [1].

Chronic painful PSN is the most common type of neuropathy and is estimated to affect up to 26% of people with diabetes [2]. It reduces sensation in the lower extremities and contributes to the increased possibility of ulceration and amputation in diabetes sufferers. Autonomic neuropathy can have rigorously devastating effects on various body functions. Gastroparesis (delayed emptying of the stomach leading to abdominal pain, nausea and vomiting) affects up to 50% of people with diabetes at some time [2]. Cardiovascular autonomic neuropathy (CAN) affects the nerves that control the heart and blood vessels. This can lead to a rapid heartbeat, exercise intolerance, sudden low blood pressure on standing, and even a silent heart attack [2].

More complications arise when the nerve damage leads to a loss of sensation in the feet of a patient with diabetes, so that injuries due to trauma or the damage caused by ill-fitting footwear, which would normally be painful, go undetected [4]. The loss of sensation can lead to a psychological disconnect with the affected limb to which the patient with diabetes can become uncaring and which may reduce compliance with preventative or therapeutic treatments.

Additionally, a subordinate impediment of the neuropathy is abnormal and persistent muscular contractures in the feet, which causes disfigurements and high-pressure zones in footwear,

affecting the individual's gait or causing loss of mobility, resulting in a greater risk of trauma and chronic ulceration. This degenerative process has an obvious dramatic impact on their quality of life [6].

PSN leads to DFU that can go unnoticed due to the lack of sensation. If DFU develops, the wound can deepen and become infected; in this scenario, healing wouldn't help much because the originating cause of the DFU remains. Such infection has serious consequences for limb survival and can be life threatening [6].

Diabetes sufferers in England and Wales are 37.5% more likely to die earlier than their peers in other countries. For type 1 diabetes, mortality is 129.5% greater than expected and it is 34.5% greater for type 2 diabetes. The greatest increase in risk of death is in younger age groups and females [7].

With type 1 diabetes, the remaining life expectancy figures between those with type 1 diabetes and those without reduce as the age range increases. In men, the difference between the 20 to 24 age groups is 11 years, whereas it is five years in the 65 to 69 age groups. Similarly, in women the difference is 14 years between the 20 to 24 age groups, and seven years in the 65 to 69 age groups [2].

In type 2 diabetes, the average reduced life expectancy for someone diagnosed in their fifties is about six years [2]. Data from the National Diabetes Audit (NDA) for the last few years suggest that more than 20,000 people with diabetes die before their time each year in England and Wales [2].

1.3 Amputation

Any diabetes sufferer can be affected by foot problems. A lack of proper care and health management can lead sufferers to nerve impairment, devastated muscles, sweat glands and poor blood circulation in the feet and legs, which subsequently, ends in amputation.

Reviewing the feet of people with diabetes regularly and keeping blood glucose, blood fats and blood pressure under control can prevent some of the complications associated with the feet [8].

ABSTRACT

Patients with diabetes have a 15 to 40times greater risk of leg amputations than those without diabetes, due to a loss of protective sensation, ulceration, infection, and gangrene [9]. Diabetes is the most common cause of lower limb amputations and over 6,000 leg, toe or foot amputations happen each year in England alone [7]. There are over 100 amputations a week amongst people with diabetes [2].

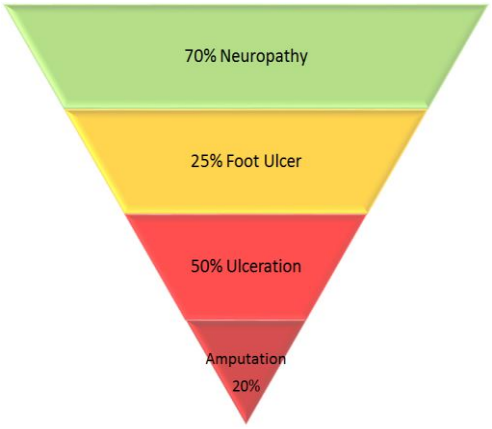

Figure 4: *Amputation sufferers' ratio out of total number of neuropathy sufferers*

According to some studies, amputation carries with it a significantly higher mortality rate at follow-up, ranging from 13–40% at one year to 39–80% at five years [10]. Many amputations are preceded by foot ulceration caused by a combination of impaired circulation and nerve damage. Various studies suggest that about 2.5% of people with diabetes have foot ulcers at any given time [2]. This would suggest that there are about 80,000 people with foot ulcers across the UK [2].

A multi-disciplinary team of diabetes specialists of wound care, vascular and musculoskeletal disease cover the diverse treatment options and match these to the specific needs of individual patients [5]. However, during the whole process to figure out the specific needs of individual patients, DFUs can worsen and become infected and this infection can lead to amputation.

Typically, of the 70% of patients that present to the multi-disciplinary clinic with neuropathy, 25% will go on to develop a foot ulcer. Among those foot ulcer sufferers, around 50% will become infected; 20% of those with infected ulcers will unfortunately undergo varying degrees of amputation [11].

Thus early diagnosis, correct assessment and patient self-management are important factors that permit remedial action to be taken earlier and manage the condition properly, identifying higher risk patients. Sufferers lose mobility and this degenerative process has an obvious dramatic impact on their quality of life. If not carefully monitored and treated in a timely fashion, lower limb amputation is unfortunately commonly prescribed [12].

1.4 Costs

The maintenance of healthy feet is clearly fundamental in enabling sufferers to preserve an active and healthy lifestyle and reduces sufferers' risk of falling. One of the main causes of ulceration is diabetic neuropathy [13, 14]. Foot complications are, indeed, some of the most frequent problems of diabetic mellitus, a key contributor to medical costs, as 50% of all inpatient admissions for diabetes are due to foot complications [15]. The current direct patient care cost (which includes treatment, intervention and assistance with complications) for those living with diabetes is estimated at £10 billion [1, 2]; in other words, 10% of the NHS budget is spent on diabetes. This works out at around £286 a second [2]. The total cost (direct care and indirect costs) associated with diabetes in the UK is presently at £23.7 billion and is anticipated to rise to £39.8 billion by 2035/6 [2].

One in ten hospital beds is occupied by someone who has diabetes [10]. People with diabetes are twice as likely to be admitted to hospital [10]. One out of four people admitted to hospital with heart failure, a heart attack or a stroke has diabetes [2]. In 2012, 42.2 million prescriptions were distributed in primary care units across England at a net ingredient cost of nearly £768 million. This is an increase in cost of 7.7% over 2010 [2].

One out of twenty people with diabetes incurs social services costs. More than three-quarters of these costs were associated with residential and nursing care, while home-help services accounted for a further one-fifth [2]. Consequently, the presence of complications increases social services costs four-fold [2].

1.5 Peripheral Neuropathy Assessments

The noteworthy morbidity and mortality associated with PSN have provided a driving force for the development of better means to screen, diagnose and assess the condition. Screening for loss of sensation helps to prevent foot ulcerations and amputations [1]. Clinical practice guidelines recommend annual screening for neuropathy [16]. Currently accepted techniques for the assessment of peripheral neuropathy such as the vibration, neurometer and SWME methods, used to identify insensitive regions on the plantar surface of the patient, are considered quite

rudimentary [17]. Several different methods are commonly used to screen for and assess DPN. Descriptions of these methods are below.

1.5.1 Reflex Testing

The inability to perceive ankle reflexes is associated with increased risk of foot ulceration [4]. In neurology, it is traditional to test all reflexes for the DPN assessment but it is most common to test only the ankle reflexes. The examiner gently strikes the Achilles tendon of the subject with a reflex hammer while he/she is in a sitting position; if no reflex occurs, the process is repeated with reinforcement [1, 4]. However, the test is a poor predictor of ulceration [1].

1.5.2 Pinprick Sensation

Pain sensation can be tested with a sterile safety pin. The inability of a subject to perceive pinprick sensation has been associated with an increased risk of ulceration [4]. The site of the testing varies with the specific algorithm, but may include the dorsum of the greater toe or the plantar aspect of the distal first, third, and fifth toe of each foot [1]. The pin is applied just proximal to the toenail on the dorsal surface of the hallux with a force that is enough to deform the skin. The inability to perceive a pinprick, when it is applied, is regarded as an abnormal test result [4]. The assessment of neuropathy using pinpricks is highly subjective and is thus poorly reproducible [1].

1.5.3 Vibration Testing

The tuning fork is widely used in clinical practice and provides an easy and inexpensive test of vibratory sensation. Traditionally, vibration perception has been measured with a 64, 128 or 256 Hz tuning fork [1]. The tuning fork provides an easy and inexpensive test of vibratory sensation, but tuning fork results are less predictive of ulceration than results from tests using monofilament [17]. Vibratory sensation should be tested over the tip of the great toe bilaterally. An abnormal response can be defined as when the patient loses vibratory sensation and the examiner still perceives it while holding the fork on the tip of the toe [4]. The test relies on examiner experience, which has a variable correlation with quantitative tests [1]. Although vibration testing can be a highly subjective measure of the severity of neuropathy and may be poorly reproducible, the absence of vibration sensation at the great toe is significantly associated with development of foot

ulcers [1].

1.5.4 Neurometer Testing

In this test a painless electrical stimulus is applied to a specific location on the foot that can be

detected by the patient. The Neurometer generates a constant current stimulus by monitoring and compensating for tissue impedance variations [18]. Common metabolic/toxic and progressive neuropathies affect sensory nerves and the subsequently affected sensory nerves pass through reversible stages of hyperesthesia (often sub-clinical) followed by hypoesthesia and anaesthesia [18]. The Neurometer detects hyperaesthetic sensory neuropathy in non-diabetics with impaired glucose tolerance and in non-diabetic overweight individuals [18]. This ability to detect abnormalities in conditions potential to a high risk of polyneuropathy is a great clinical diagnostic advantage [18]. It also detects the hypoesthesia of advanced neuropathic conditions as well as nerve regeneration.

Electrodes are placed at the agreed test site and held in place with tape. The subject is instructed to press a button, releasing it when a stimulus is detected at the site of the electrode(s). At this point the CPT measure is verified. This effectively monitors responses for consistency [18].

A different range of AC frequencies is applied on a different spot [19]. At each frequency (2000, 250 and 5 Hz), an R-CPT value was generated from one to 25. A value from six to 13 is categorised as normal, while a value from one to five is known hyperesthesia (increased sensation). The rest of the value, i.e. from 14 and 25, showed hypoesthesia (decreased sensation). Hyperesthesia and hypoesthesia show the presence of sensory neuropathy.

1.5.5 Sympathetic Skin Response

The sympathetic skin response is a reflex that happens in response to a variation in the electrical potential of the skin. It is transient in nature, and can be caused by a variety of stimuli [20]. Measurement requires special equipment that is not typically available in most physicians' offices [20].

1.5.6 Quantitative Sensory Testing

Quantitative sensory testing is an extension of the sensory portion of the neurological evaluation. It is the determination of the absolute sensory threshold, which is useful when assessing the integrity of the axons that form the peripheral nervous system and their distal receptors [20].

1.5.7 Semmes–Weinstein Monofilament Examination (SWME)

Max Von Frey presented variable diameters of monofilament, horse hair mounted inside a tube, to evaluate cutaneous sensation for the first time in 1899 [20]. The monofilament was applied perpendicularly with a known force that caused an obvious bend; at this stage, the patient was asked for verbal feedback to acknowledge that he felt the force applied by the monofilament [20]. The device was refined in 1960 by psychologists Florence Semmes and Sidney Weinstein [20]. After gaining increased recognition through its use in leprosy research, the SWME was approved as the standard assessment tool for patients with peripheral neuropathy [4, 20]. Peripheral neuropathy is the most common cause in the pathway to a diabetic foot ulcer [4]. 10g monofilament, also known as Semmes–Weinstein monofilament, is a non-invasive, simple to use, readily accessible and relatively inexpensive screening instrument [20]. These qualities make it an effective, commonly used and traditional approach to examining peripheral sensory neuropathy.

Research has shown that the inability to detect a 10g force (i.e. 98mN) applied to key weight-bearing points indicates a degree of neuropathy consistent with increased risk of ulceration [21]. The use of 10g monofilament is prevalent across the world and its efficacy in this regard has been confirmed in a number of trials, including the recent Seattle Diabetic Foot Study [4]. Currently, in order to test this, an extruded homopolymer, known as the Semmes–Weinstein monofilament (SWM), is applied to the patient's foot at various pressure points by a trained clinician. Nylon monofilaments are designed to buckle 10mm when a 10g (98mN) force is applied; at this point, the patient is required to acknowledge whether they can or cannot feel the probe on the area in question and the process is repeated for a number of sites on both feet.

The loss of the ability to detect this pressure at one or more anatomic sites on the plantar surface of the foot has been associated with the loss of large-fibre nerve function. It is recommended that

four sites (first, third, and fifth metatarsal heads and the plantar surface of the distal hallux) be tested on each foot [4]. The sensation of pressure using the 10mm buckling 10g monofilament should first be demonstrated to the patient on a proximal site (e.g. the upper arm). The sites of the foot may then be examined by asking the patient to respond "yes" or "no" when asked whether the monofilament is being applied to the plantar surface; the patient should recognise the introduction of pressure as well as identify the correct site. Areas of callus should always be avoided when testing for pressure perception [4]. Many studies have established that loss of pressure sensation using the 10g monofilament is highly predictive of subsequent ulceration [4].

1.6 High-Pressure Areas on Plantar Surface

A statistical study of foot pressure indicates distinguishing trends and was based on new parameters: normalised peak pressure (NPP) and pressure contact ratio (PCR) [22]. According to these methods, the foot is divided into 10 areas, as shown in Figure 5, and the foot pressure is measured using optical pedobarograph.

Figure 5: *Areas of the foot [22]*

Foot pressures *P* have been shown to be affected by the body weight and walking velocity of the subject [22]. One of the new parameters (NPP) is obtained by normalising the pressure *P* with reference to the body weight and walking velocity parameters using the following equation:

$$NPP = \frac{P}{W*V} * 100 \qquad 1.1$$

Where *P* is the peak pressure in the specified area, *W* and *V* are the weight and walking velocity of the subject respectively. The obtained NPP values for each of the 10 areas are shown in Figure 5.

The mean values of the NPP in different foot areas have been obtained. In diabetic sufferers with sensory paralysis, it is found that the foot, once subjected to moderate pressure for a longer duration, is more prone to ulcers than the one subjected to high pressure for a shorter duration [22].

In this context, a newer parameter known as PCR is considered; this new parameter takes into account both the magnitude of pressure and the time for which it acts. It is defined by the following equation:

$$PCR = \frac{t}{T} * \frac{P}{W*V} * 100 \qquad 1.2$$

Where *t* is the time during which pressure ≥50% of the peak pressure acts on the specified area, *T* is the total contact time of the same foot.

Seventy-eight people of different classes, i.e. normal, diabetic, diabetic neuropathic and diabetic neuropathic with ulcers, were studied and the highest pressure areas were found to be the toe, metatarsal and heel areas. The NPP values for diabetic subjects are higher than normal and the highest pressure regions, in descending order, are the big toe, the fifth, second and first metatarsals and the heel. The diabetic neuropathic subject with ulcers also shows higher NPP values than the corresponding normal values, the highest being in the toe, metatarsal and heel regions as shown in Figure 6 and 7.

Another study also investigates the high-pressure region of the plantar surface [23]. The system used in this study was Electronisches Meßsystemzue Erfassung von Druck verteilungen (EMED

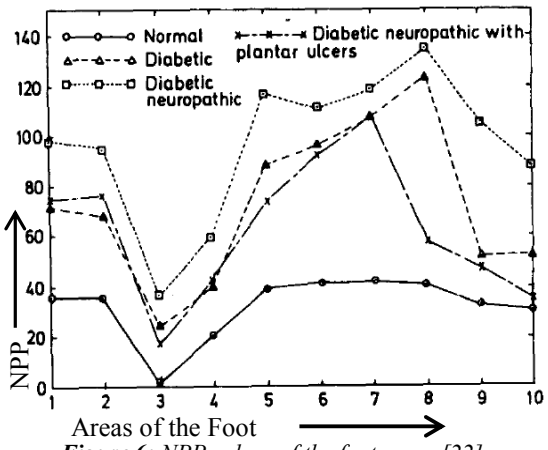

Figure 6: *NPP values of the foot areas [22]*

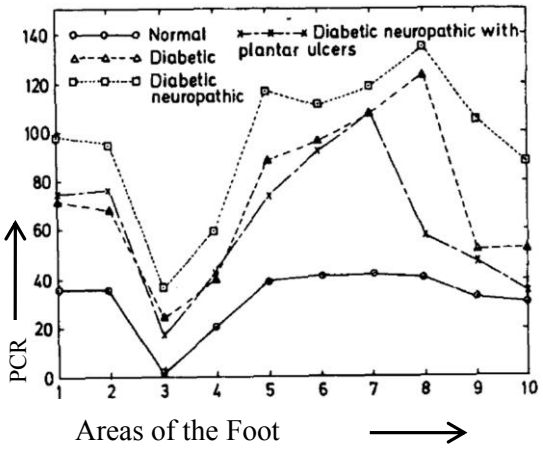

Figure 7: *PCR values of the foot areas [22]*

Novel Inc.). Eight subjects were examined at different clinics and the data was recorded and analysed; it was concluded that the peak pressure areas are the heel, the first, third and fifth metatarsals, and a big toe [23].

J. Jacqueline et al. [24] developed a portable insole plantar pressure acquisition system. To place sensors at a suitable place, higher pressure regions were evaluated using an APEX foot imprinter (APEX, Hackensack, NJ). The subjects had to walk three times on an APEX footprint mat. The highest pressure areas determined were the heel, the first, third and fifth metatarsals, and the great toe.

N. K. Rana [23] investigated this area to develop a dynamic pressure scanner. Prior to the development of the foot pressure scanner system, a study was carried out to determine the highest pressure regions of the plantar surface. A group of healthy people were asked to walk over an EMED foot mat system at different clinics. The finding of the study was that the highest pressure zones of the plantar surface were the heel, the first metatarsal head, the third metatarsal head, the fifth metatarsal head and a big toe.

The same pressure regions, i.e. big toe, first, third and fifth metatarsals, and heel, were selected as high-pressure regions by L. Shu et al. [25] to develop an in-shoe plantar pressure measurement and analysis system based on a textile fabric sensor array.

1.9 Conclusion

Diabetes is a common metabolic disorder and may lead to different complications of which PSN affects the peripheral extremities of the body. PSN leads to diabetic foot ulcer and lack of proper care and management may ends up into amputations. The current direct cost of patient care for those living with diabetes is estimated at £10 billion which is 10% total NHS budget. Regular screening of diabetic patient is required for the assessment of peripheral sensory neuropathy. Neurometry, vibration and SWME are the most practice methods for the assessment of PSN. SWME is the most popular and efficient assessment techniques, high-pressure areas (Toe, metatarsal and heel) are assessed. Further the image processing is discussed in the research perspective.

CHAPTER 2. Literature Review

A large proportion of individuals who live with type2 diabetes suffer from plantar sensory neuropathy (PSN). Regular testing and assessment for the condition is required to avoid ulceration or other damage to patients' feet. Currently most accepted practice known as SWME involves a trained podiatrist testing patients' feet manually with a hand-held nylon monofilament probe.

2.1 Manual and Mechanical SWME

Hitherto the Semmes–Weinstein Monofilament Examination (SWME) is one of the most common methods to test pressure points at specific weight-bearing areas, namely toe (hallux), metatarsal and heel (calcaneum).

The SWME is designed to bend by 10mm when 10g force is applied. Studies have shown that the inability of the patient to feel the pressure of monofilament, when the monofilament bends by 10mm at 10g force, indicates a degree of neuropathy. This technique although most widely used, incurs its own shortcomings. The key downside related to the SWME is the judgment of acceptable force. The precision of the accepted 10g force is based on the practitioner's guess by observing the perceived bend or buckle of the filament i.e. observing the 10 mm bend through the naked eye. There are opportunities to misjudge the bend and consequently misdiagnose the patient. The measurements to meet standard by guessing can become more erroneous, if one takes the fact into consideration that monofilaments age and lose compressible strength due to repeated use [58].

Even though the monofilament size and buckling criteria are well documented, manufacturers often fail to perform accurately within these parameters. K. D. Smith et al. [59] studied the force of 10 unused monofilaments, which were specifically designed to collapse with approximately 10 grams of direct force. The results discovered that the monofilaments buckled on average after only 8.4 grams of force, a 16% discrepancy, during the first application. This outcome was statistically significant as the calibrated 10 grams of buckling force was outside of the designed 5% window of standard deviation; therefore, even calibrated monofilaments may provide inaccurate results [59].

A series of random applications may be needed to minimise any guessing by the patient. This test often requires 10 to 15 minutes to complete, which is often not practical in a busy clinic. Aside from time considerations, the reliability of the monofilament has inherent flaws. This makes interpretation of the testing results questionable and, therefore, limits its clinical application [20].

Another complicating factor inherent in the design of the SWM is mechanical exhaustion incurred after a series of continuous applications. Once the monofilament is subjected to cyclical stress, the reproducibility of the testing device is altered. Several monofilaments have been tested with a fatigue testing device [60]. After 500 consecutive cycles, the results showed there was an average reduction of 1.2 grams (12%) needed to bend the monofilament. Other than obvious manufacturing and/or injury -related defects in the monofilament, there are no guidelines that describe the service life of a standard SWM [60].

Further, currently Podiatrists rely on subjective judgement as to which areas may constitute a high-pressure site, this is frequently based upon bony prominences, deformity or soft tissue indicators. On this basis it is the gold standard that all these identified areas are then tested for peripheral neuropathy (a risk factor for the development of ulceration). However, this process potentially fails to identify all high-pressure sites and also cannot indicate the progression of diabetic foot disease in a measurable manner. Moreover, this test is the first to allow response times to the neuropathy test to be recorded, thus providing the earliest possible indicator of those individuals who may be at risk of ulceration and amputation.

In short the traditional approach is considered cumbersome, labour-intensive, repeatability is difficult to maintain and prone to experimenter bias [16]. Ultimately, those suffering have already reached such numbers as to make a traditional manual PSN test unfeasible.

Furthermore, the resources required simply to test current sufferers outstrips that which is available from National Health providers. Therefore, there is a clear and present need to expedite, simplify and automate the testing procedure that is, autonomous, repeatable, and simplifies the testing procedure. Additionally, a system that provides photographic evidence of patients' feet and their condition over time is also valuable to both medical practitioners and researchers. Automated

techniques such as this would reduce waiting time, increase throughput and have neutral, unbiased selection of test points.

Previous work, was presented by [61] using a robotic monofilament probe to exercise SWM mechanically as shown in Figure 15. But the approach of selection of pressure points of plantar surface is manual i.e. each time the robotic arm is adjusted manually to apply the probe at various pressure points, moreover selected areas were limited to three sites namely toe, first metatarsal and fifth metatarsal. The toe and first metatarsal heads are taken geometrically in the same vertical line, while the first and fifth metatarsals are taken in the same horizontal line as shown in Figure 16.

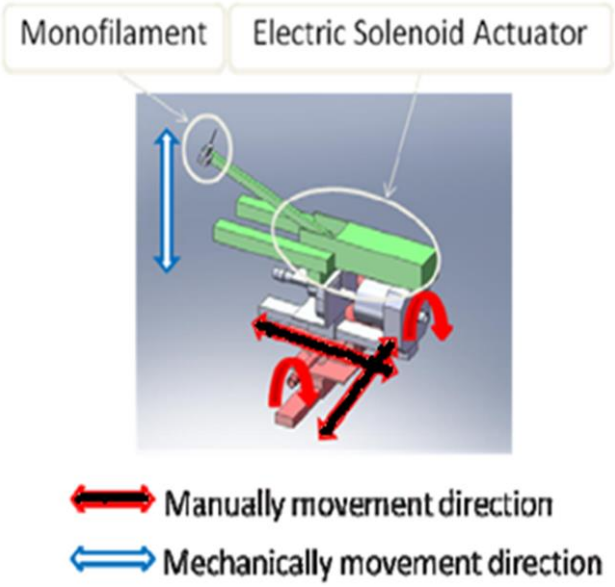

Figure 15: *The model for the plantar aspect of the fifth metatarsal position [61].*

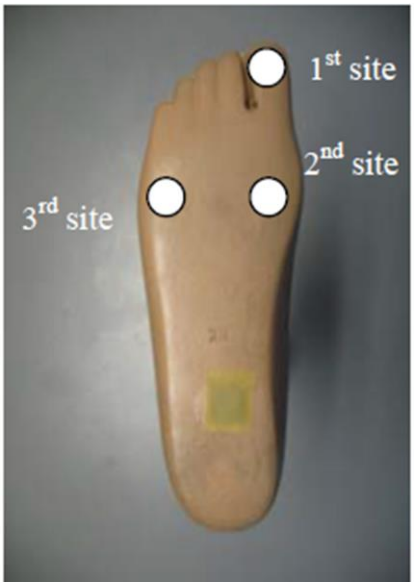

Figure 16: *Monofilament testing sites [61].*

These three points do not cover all the pressure points on plantar surface. Moreover, this might work perfectly for a normal foot anatomy, but a patient with inborn deformities such as flat or high arched foot, clubfoot, and extra digit may alter the pressure bearing points [23].

The research work describes a novel approach to automatically select suitable pressure points, namely toe (Hallux), metatarsal heads and heel (Calcaneum), on a given patient's foot that corresponds to those chosen by a trained podiatrist for sensory neuropathy examination via optical image processing incorporating plantar anthropometry i.e. automating the current manual SWME.

2.2 Plantar pressure distribution Measurement

Human plantar pressure distribution measurement provides key information to be used in medical diagnosis related satisfactory function in the foot [23] and its foot shape as well as shoe making industry. Plantar pressure measurement is an integral part of diabetic analysis [23]. Early identification of individuals at risk of developing ulceration of foot lesion is one of the important means to reduce devastating effects and played an important role in the management of lower limb disorders. Specifically, footwear adjustments and redistributive insoles aimed at unloading areas of high pressure prone to ulceration have been evaluated for efficacy in patients with diabetic peripheral neuropathy. Investigations carried out and established a relationship between ulceration and high-pressure areas at plantar surface [23].

Methods dealing with plantar pressure distribution measurement can be categorises into quantitative and qualitative methods [62]. Qualitative methods are mainly used to measure the shape of the foot rather than the magnitude of load distribution.

Early systems to measure foot pressures utilised ink prints of the subject's foot to show contact distributions [63]. Likewise, pressure sensitive films have been used for direct static pressure measurements [63]. Pedobarograph systems, consisting of a camera positioned below plastic and glass plates, were the first devices used to capture dynamic information [63]. Introduction of array force transducers controlled by multiplexers has led to easy to use systems which can record samples at fast intervals, thus yielding dynamic information. Previous investigators have used these devices to study a variety of diseases, deformities, activities, normal variations and changes, treatment procedures and devices. Plantar pressure measurements have been used to study diabetes club foot, hallux valgus, Marfan's syndrome Charcot-Marie-Tooth neuropathic ulcers Morton's foot and flat foot [29].

A variety of the plantar pressure measuring systems are currently available in the market or research laboratories. These systems based on several types of sensors/ mechanical arrangements e.g. capacitance methods [11, 13, 62], piezoelectric sensors [14, 62], force sensitive resistors [15, 16, 62] and optical techniques [1, 3, 65].

These systems are used for miscellaneous applications e.g. Assessment of foot wear [60], gait and standing posture problems. Some work by R. M. Queen et al., has been carried out to find the difference between gender plantar pressures distributions [66], R. L. William, et. al., have focused on foot ulceration problems due to diabetes [67]. Further research on improvement in balance related to gait and elder people or impaired individuals have been carried out by A. Gioftsidou et. al [68].

The electronic sensors technologies most commonly used in pressure measurement systems are capacitance sensors, resistance sensors, piezoelectric and piezoresistive sensors. All of these are able to provide an electronic signal (voltage, current) that is proportional to the pressure applied on the sensor. The selection of sensors depends on the nature of applications and can be grouped into the following [64]. It has been suggested that sensor sizes should not be greater than 6.4 × 6.2 mm [69]. Sensors always measure the average pressure over the whole sensor surface [67]. For a small anatomic structure, produces a defined peak pressure, the larger sensors and smaller spatial resolution will underestimate the real pressure values due to the lower pressure around the peak [70]. The pressure range should be sufficiently high to accommodate expected pressure and loads [69].

2.2.1 Pressure measuring sensors

Followings are some sensors used in most common pressure measuring systems.

2.2.1.1 Capacitive sensors

Capacitive sensors electronically measure the capacitance between two conductors in a dielectric environment, usually air or a liquid. Once a pressure is applied the dielectric elastic layer bend, which shorten the distance between the two plates resulting in a voltage change proportional to the applied pressure [68, 71]. The schematic diagram is shown in Figure 17.

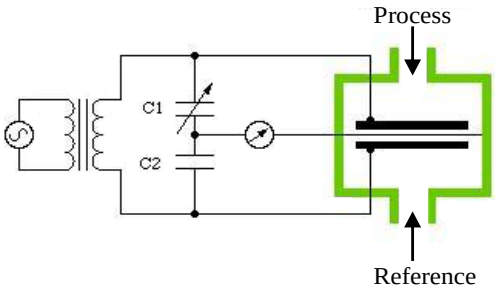

***Figure 17**: Capacitive pressure sensor construction [68]*

2.2.1.2 Resistive sensors

Resistive sensors measure resistance of conductive foam enclosed between two electrodes. The electrical current through the resistance sensor increases as the conductive layer deforms under pressure [68, 71]. FSR is true example of resistive sensors. The schematic diagram is shown in Figure 18.

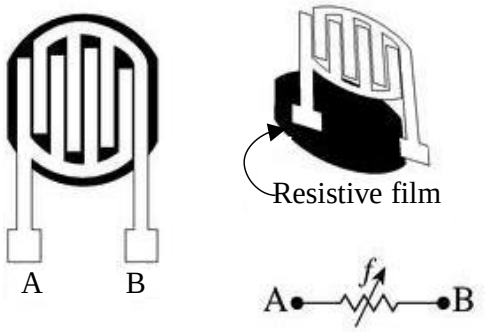

***Figure 18**: Resistive pressure sensor construction [68]*

2.2.1.3 Piezoelectric sensors

Piezoelectric sensors produce an electric field (voltage) in response to pressure [57]. The most suitable materials for clinically-oriented body pressure measurements appear to be polymers, such as polyvinylidene fluoride (PVDF) [71]. The reason behind this is because polymer-based sensors can be made as thin, flexible, and deformable elements (e.g. in-shoe device configurations). A thin layer of metallisation is applied to both sides of the polymeric piezoelectric sheet to collect the electrical charge and permit electrical connections [71]. The schematic diagram of piezoelectric sensors is shown in Figure 19. Piezoelectric pressure sensors measure dynamic pressure. They are typically not suited for static pressure measurements [71].

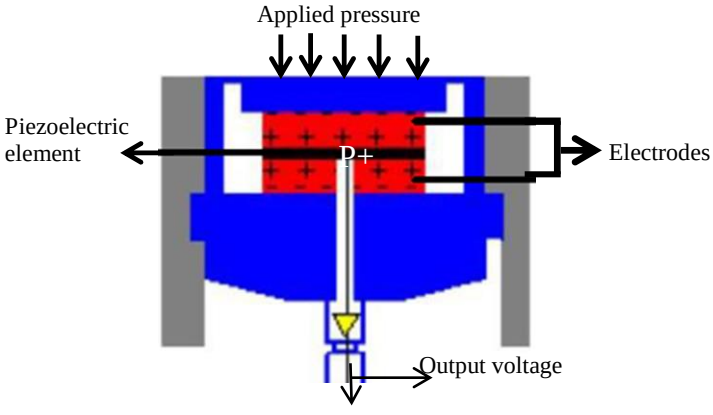

***Figure 19**: Piezoelectric pressure sensor construction* [71]

2.2.1.4 Piezoresistive sensors

Piezoresistive sensors are made of semiconductor materials e.g. polycrystalline that act as force or pressure sensing resistors in an electrical circuit. piezoresistivity is a material property of semiconductors where the bulk resistivity is influenced by forces or pressures applied to the material [71]. Hence, when a piezoresistive sensor is loaded, its resistance reduced and vice versa. The schematic diagram of piezoresistive sensors is shown in Figure 20.

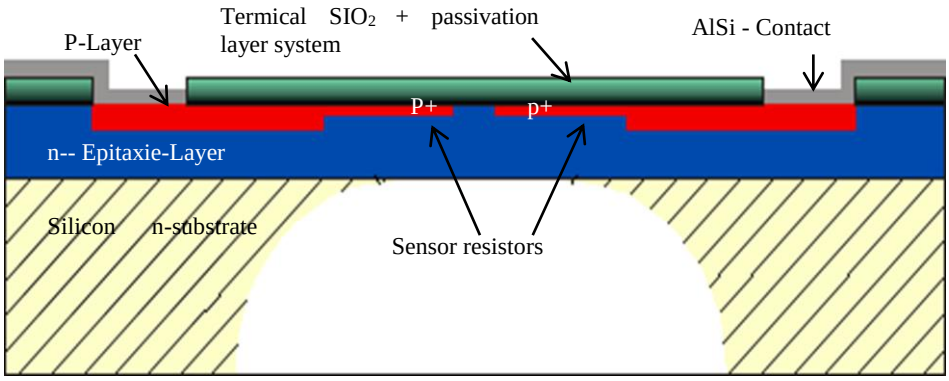

***Figure 20**: Piezoresistive pressure sensor construction [71]*

2.2.2 Strain Gauge Mechanical system

The strain gauge sensors change their resistance when mechanical deformation occurs due to load. The external load changes the conductor length and cross sectional area that are directly related to it resistance. A mechanical assembly of the sensor system developed by [62], consists of a 9×3 matrix of cantilevers. The cantilevers are supported by beams. Studs are welded on the end of

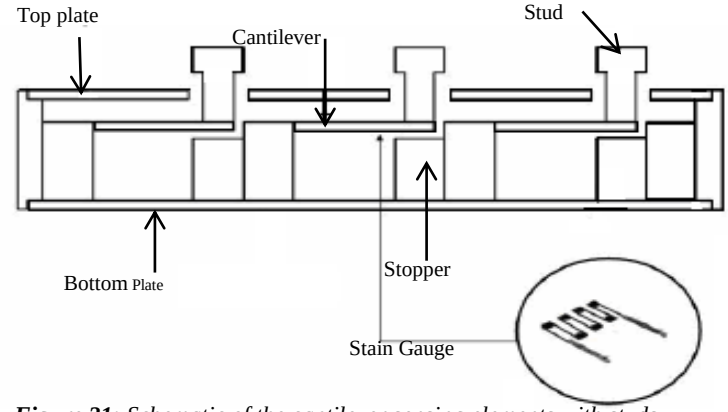

***Figure 21:** Schematic of the cantilever sensing elements with studs*

cantilever to transmit the load. There are holes on top plate through which studs can move freely when force is exerted. A stopper is provided under each cantilever to avoid a permanent deformation due to sudden heavy load. A pair of foil type strain gauge cantilever sensing elements, mounted on either side of cantilever, connected in Wheatstone bridge configurations and shown in Figure 21.

Twenty-seven pairs of wires coming from the Wheatstone bridge network in the sensor array are wired to a 32-1 analogue multiplexer. Any change in selected array element is coordinated with an on-chip ADC using 8-bit microcontroller. The data obtained from the microcontroller is passed on to a PC and displayed in a suitable graphical interface. Each matrix values are observed before and after loading and the variation in the pressure distribution is then plotted.

2.2.3 Pressure measuring system design

Generally, the plantar pressure measurement systems are divided into two classes in terms of design [64].

2.2.3.1 In-shoe system

Force plate studies generally represent barefoot, isolated steps and do not allow the analysis of the ongoing step to step variation in normal walking [72]. Coupling information from both feet during walking is not easily obtained. To analyse plantar pressure during daily life activities, a portable pressure measurement system is needed. The required sensors in insole approach must be small, thin and invariant to permanent deformation when overload for a longer period of time. Placing sensors within an insole provide a method to quantify plantar pressure measurement during daily life activities. Thus the site of the sensors placement is critical. In-shoe sensors are flexible and embedded in the shoe such that measurements reflect the interface between the foot and the shoe. The system is flexible, portable, provides range of studies with different gait, footwear design [64]. Microprocessors embedded into the sole have been used to measure pressure by [24]. The system here had a capability to collect data for up to 2 hours from 14 pressure sensors within the sole. The chosen sensors were inexpensive and 0.25 mm thick. To define the sites of greatest weight-

loading, a subject was required to walk three times on an APEX, foot imprinter, footprint mat that has been evenly inked and covered with paper. The locations of the highest pressure area centres, which appear dark, were averaged.

Subsequently, the APEX paper is then aligned on the insole to lay out the seven sensor locations. Figure 22 shows an instrumented insole with seven sensors and the connecting cable. They aimed to investigate sensate and insensate plantar pressure, shuffling gait versus normal walking. The data acquisition unit is 20 x 18 x 7 cm in size and weighs 0.8 kg. Subjects carry it in a backpack during ambulation. The test data are downloaded to the IBM PC, translates the voltages into pressures by looking up pre stored calibration tables. The system has the ability to run for 8 hours without a battery change and can be conveniently reprogrammed.

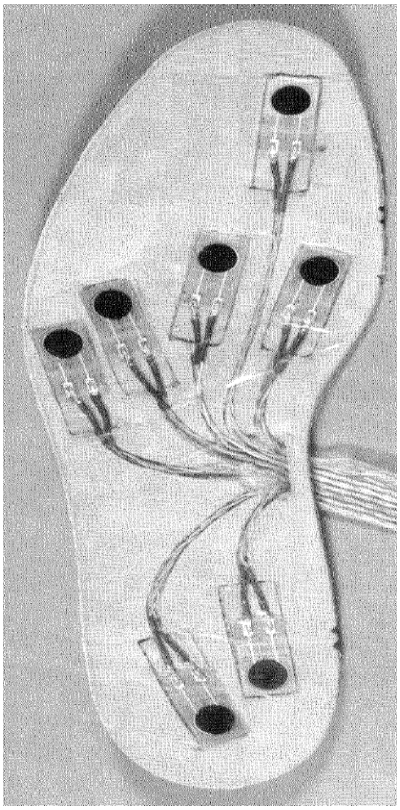

***Figure 22**: Seven pressure sensors placed under plantar pressure areas*

Figure 23: The placement of sensors and the developed foot sole.

A low cost dynamic foot pressure scanner is developed [23]. Peak pressure points on plantar surface are determined by placing 8 subjects on EMED (from Novel Inc.) foot mat system [23]. The analysis of recorded data indicated the peak pressure areas are heel, 1st, 3rd, 5th metatarsal head and toe. Force sensing resistors FSR are embedded into shoe sole of different size at peak pressure areas to measure peak pressure during walking condition [23]. These sensors are connected to data acquisition system by multi-channel Biopac MP100 as shown in Figure 23. Once data is collected, it can be sent to the computer system for analysis using USB interface.

2.2.3.2 Platform system

During walking or standing, the human foot exerts force upon the ground or underlying surface, an equal magnitude of force but in opposite direction is exerted in response. This force is termed ground reaction force [24]. Elevated plantar pressures have been widely recognised as a contributory factor in the development of several pedal pathologies, including the development of stress fractures, plantar calluses, neuropathic ulceration, forefoot deformity, increased heel pad

***Figure 24**: Capacitive pressure distribution platform*

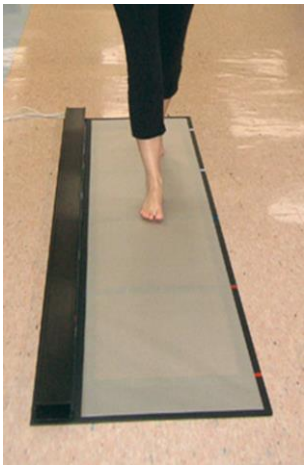

***Figure 25**: CTekscan platform pressure distribution system*

stiffness and lesser toe deformity [24]. Elevated plantar pressures have been widely recognised as a contributory factor in the development of several pedal pathologies, including the development of stress fractures, plantar calluses, neuropathic ulceration, forefoot deformity, increased heel pad stiffness and lesser toe deformity [24]. Pressure sensing elements are arranged in a matrix configuration and embedded in the floor and can be used for both static and dynamic pressure measurement. Its usage is easy because it is fixed and flat. The disadvantage here is that the participant is required to ensure they have a natural gait. It is restricted to use in a laboratory environment. Furthermore, for an accurate reading the foot must be placed centre of the sensing area [64].

Platform pressure measurement system has been used by researchers from various discipline. Used capacitive pressure distribution platform (EMED AT, Novel GmbH, Munich, Germany) was designed shown as in Figure 24 by [73], to investigate the reliability of repeated plantar pressure

distribution measurements during normal gait. Four parameters were investigated: peak pressure, maximum force, impulse, and contact time, and these were investigated in 10 areas of the foot after using the PRC mask method of subdividing the foot into ten anatomical areas of interest. A comparison of plantar pressure distribution of hemiparetic patients with a control group was performed using capacitive pressure distribution platform (EMED-F01 system, Novel GmbH) to determine quantitative, objective and reproducible criteria for better assessment of hemiparetic gait [74].

Reliability of assessing plantar pressure variables in a group of typically developing children, during barefoot level walking has been investigated using Tekscan system. Tekscan is one of the popular platform pressure measurement system [75]. It consists of 5 mm floor mat composed of 2,288 resistive sensors.

2.2.3.3 Optical System (Pedobarograph)

An optical technique is used to measure pressure distribution across the plantar surface [65]. A simplified diagram is shown in the Figure 26. A glass plate illuminated at the edge of the plate by strip of lights is used. An opaque plastic mat is laid over the glass on which the subject stands. The area of the foot in greater contact due to high load or pressure can be viewed from below with greater intensity of light.

The phenomena emerged because of the difference in the refractive indices of i.e. glass, plastic mat and air. Commercially available systems currently employed by clinicians and researchers to assess dynamic plantar pressures include in-shoe measurement systems (Novel Pedar®, TekScan F-Scan®, RS-Scan Insole® and IVB Biofoot ®) and platform systems (Novel Emed®and the RSScanFootscan®) [24]. The validity of these measurement systems has been documented throughout the literature, suggesting they are able to

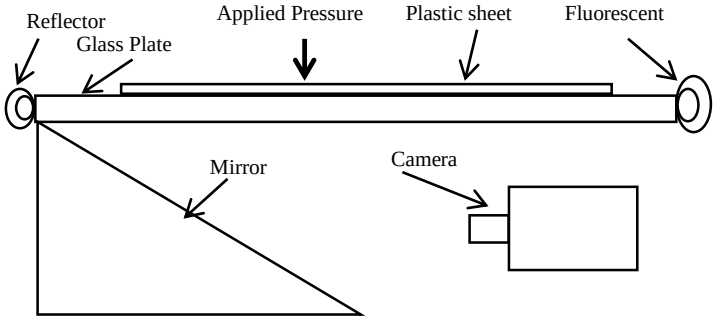

Figure 26: *Schematic of pedobarograph*

accurately quantify dynamic plantar loading patterns of the foot [58].

The key difference and advantage of the system developed and presented in this report is that it can be used to not only identify the pressure areas but also apply a mechanical probe as well i.e. a complete and automated replication of SWME. The probe driven mechanical system is impossible to fit into the above mentioned plantar pressure area measurement systems and these systems only carry out one characterisation, the pressure points. With the system presented here, pressure points are detected followed by a mechanical probe that tests for PSN. Clinicians and patients are provided with an image of their foot surface with resulting data that can be stored and viewed over time, providing them with photographic evidence of the health of their feet, empowering them to take action on and developing a mature healthy behaviour.

The human foot is a complex structure, playing an important role in the locomotion processes of the lower extremity [77]. People vary in foot shape; gender, age, race, and even lifestyle habits play an important role in shaping the foot [78].

Foot anthropometry is the measurement of the size and proportion of different parameters of the foot and is accepted in studies related to ergonomics, forensics science and anthropology. Parameters often measured include foot length and foot breadth [79]. The most common foot parameters used for foot anthropometry are foot length, ball length, ball width, girth, heel width, instep height, instep width and toe height [79, 80, 81, 82, and 83].

Previous anthropometric studies of foot shape have used different protocols and measurement devices. Most anthropometric approaches directly measure the foot dimensions using a Vernier calliper or cloth tape flat ruler, whilst others have used foot prints. Additional studies have devised physical foot measurement platforms [81]. There are also methods devised to quantify foot posture or mobility from digital images; these methods have a commonality in that they involve capturing a digital image of the foot. However, the post-processing procedures differentiate amongst them [84, 85, 29, and 86].

Though their research objectives are diverse, the methods followed by those referenced involved manual intervention like marking “bony” land marks [85], painting the plantar surface with ‘‘face

and body'' paint and attached retro reflective targets [30], making the procedures cumbersome and difficult to repeat.

An automated selection of pressure points of plantar surface lies on plantar contact area using optical imaging is proposed and discussed in chapter 4 [87]. An optical scanner was used to obtain the human plantar surface with specific skin colour tone detection. In Chapter 5 a superior method is proposed using the same system architecture as described in [87] but an improved algorithm is presented that extracts a plantar surface pressure point using a combined optical image processing and plantar anthropometry approach independently of subject ethnicity. Chapter 6 presents a further algorithm that improves the method used in chapter 5 to make the algorithm independent of optical point of reference i.e. an integrated foot stopper.

2.3 Image Processing

It is necessary to understand the importance of different colour spaces in this presented research perspective. A digital image is a numeric representation of two-dimensional data representing spatial and intensity or colour information as shown in Figure 8.

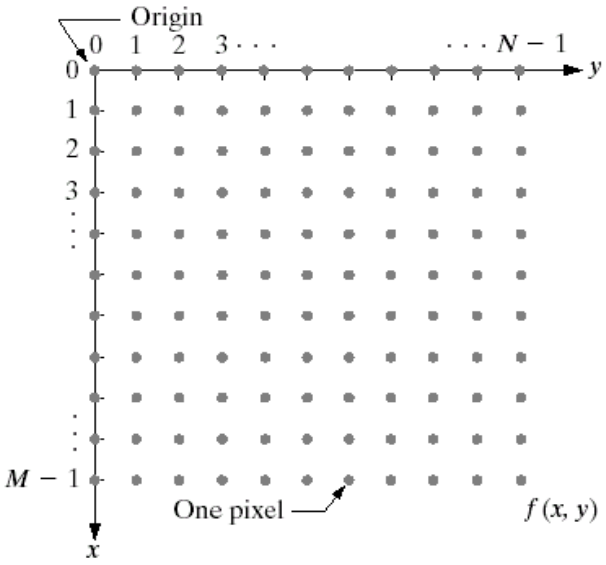

Figure 8: *Digital image layout*

The two-dimensional (2D) digital image $I(m,n)$ represents the 2D continuous spatial signal $I(x, y)$ through a sampling process [26]. The indices m and n designate rows and columns of the image, respectively. Digital images are composed of individual pixels, formed by the words "picture" and "element", to which discrete brightness or colour values are assigned [27]. The image pixel located at the intersection of the m^{th} row and n^{th} column is denoted by $I(m, n)$.

2.3.1 Colour Representation

The colours are actually electromagnetic waves described by their wavelength. The visible spectrum, i.e. the portion of the electromagnetic spectrum that can be detected by the human eye, ranges from 390nm (violet) to 750nm (red) [28].

The following attributes characterise the light.

a) Intensity
b) Radiance
c) Luminance
d) Brightness

Intensity is the only attribute involved in the case of achromatic light. On the other hand, in the case of chromatic light, the other three attributes are used to measure the quality of the light source [28]. Radiance refers to the amount of energy emitted by the light source. The luminance measures the amount of radiation perceived by an observer. The brightness is associated with the light intensity [28].

The colour depth measures the amount of colour information available to display each pixel of a digital image. A binary image has a depth of one bit. A pixel with a depth of eight bits has 256 possible values, and so on [28].

Colour spaces indicates the colour coordinate system in which the image values of a colour image are represented [29]. The colour models are used to specify colours as points in a coordinate system, creating a specific standard. In the following section, the most common colour spaces are briefly presented.

2.3.1.1 RGB Colour Model

One of the most frequently used colour spaces, especially for eight-bit digital images, is known as RGB (red, green, and blue) colour space. RGB colour space is generally used for the representation, transmission and storage of colour images on analogue devices, such as television sets, as well as digital devices, such as computers, digital cameras and scanners [30]. The scanned

foot is initially obtained in RGB colour space. RGB is an additive model where the red, green and blue colours are combined in different quantities to reproduce other colours. The pixels of an image represented in the RGB model usually have eight-bit depth, resulting in 256 possible intensities, i.e. the range of [0, 255] for each colour [28].

A colour, *C*, in the RGB model can be described to indicate the amount of red, green, and blue. Each colour can vary between the minimum value (totally dark) and the maximum value (totally intense).

$$C = rR + gG + bB \qquad 1.3$$

Where *C* is a colour in RGB, and *r*, *g* and *b* indicate the relative amounts of red, green, and blue respectively.

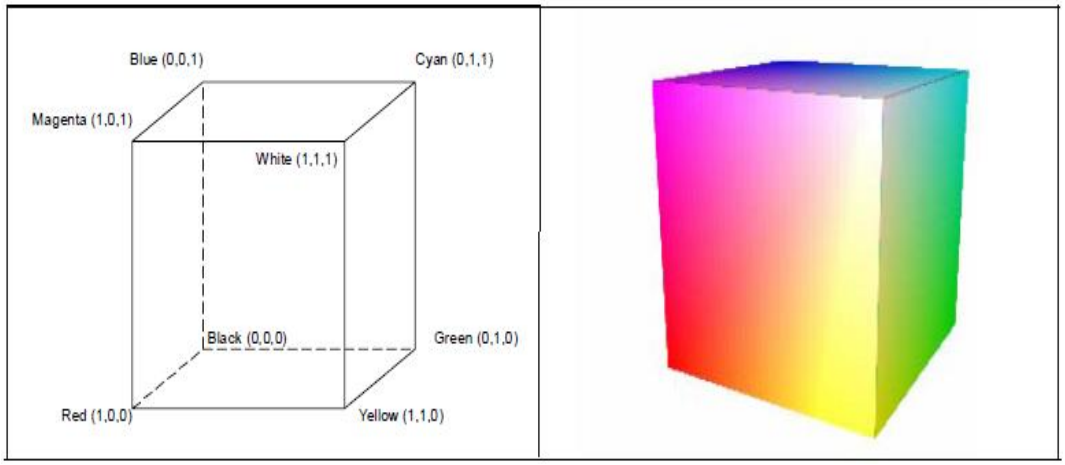

Figure 9: *RGB colour model*

When all the colours have the minimum value, the resulting colour is black. On the contrary, when all the colours have the maximum value, the resulting colour is white [28]. The RGB colour model is easy to depict graphically as a cube on the Cartesian coordinate system as shown in Figure 9. The primary and secondary colours are at the corners of the cube. The black colour is at the origin and the white colour is at its opposite corner. The diagonal between the black and the white colours is the greyscale [28]. The primary colour components are highly correlated and it is therefore difficult to execute some image processing techniques that only operate on the intensity component

of an image [31]. In RGB colour space, the luminance information is embedded into each band in the visible light spectrum of the image. Varying levels of brightness in an image cause RGB values to shift.

2.3.1.2 CMY(K) Colour Model

Like the RGB colour model, the CMY(K) colour model divides a colour into three primaries, using a subtractive rather than an additive colour creation process. The CMY(K) model is composed of the cyan, magenta, yellow and black colours [29]. This space is usually used by printers and photocopiers to reproduce the majority of the colours in the visible spectrum. The system is the subtractive colour system, in opposition to the additive system RGB. Cyan is the opposite colour of red, i.e. it acts as a filter that absorbs the red colour. The same occurs with magenta and green, and with yellow and blue [29].

It generally happens that some visible colours on the screen of a computer monitor are not printed properly on paper. This occurs because the CMY(K) used in the printers is based on a mixture of inks on the paper, and the CMY(K) used in computer monitors is a variation of the RGB space [29]. Consequently, the CMY(K) colour spectrum happens to be smaller than the RGB colour spectrum.

Since cyan, magenta, and yellow are the complementary colours to red, green and blue, the *RGB* colour space and the *CMY* colour space can be transferred through

$$\begin{pmatrix} R \\ G \\ B \end{pmatrix} = \begin{pmatrix} G_{\max} \\ G_{\max} \\ G_{\max} \end{pmatrix} - \begin{pmatrix} C \\ M \\ Y \end{pmatrix} \text{ and } \begin{pmatrix} C \\ M \\ Y \end{pmatrix} = \begin{pmatrix} G_{\max} \\ G_{\max} \\ G_{\max} \end{pmatrix} - \begin{pmatrix} R \\ G \\ B \end{pmatrix} \quad 1.4$$

2.3.1.3 Perceptual Colour Space

Perceptual colour space is another way of representing true colour images in a manner that is more natural to human perception and understanding of colour than the RGB representation. Colour spaces that are based intuitively on human colour perception are of interest to the fields of computer vision and computer graphics. Many alternative colour representations exist, but here

we concentrate on the hue, saturation and value/voluminous (HSV) colour, which is also called hue, saturation, brightness (HSB), a space popular in image analysis applications [29]. The HSV colour system, created by Alvy Ray Smith, is composed of three components: hue, saturation, and value. This model is also known as HSB [28].

By projecting the RGB unit cube along the diagonals of white to black, a hexacone results that forms the topside of the HSV pyramid shown in Figure 10 [29]. As shown, the hue *H* is indicated as an angle around the vertical axle that can be read in degrees from 0 to 360. Red is determined with $H = 0°$; as the *H* values increase, it moves counter clockwise through yellow, green, cyan, etc. and back to red at 360°. The hue attribute contains the information concerning the main wavelength in the colour, i.e. it is responsible for verifying the colour in the complete spectrum, from red to violet and magenta.

Saturation is a function of the colour's distance from the central axis (i.e. the value axis). The saturation describes the level of mixture between the hue and the white light; a fully saturated colour does not contain white light [28]. The further a colour is from this axis, the more saturated the colour in considered. The value/voluminous axis lies from the black point of the hexacone through to the centre of the circle, with values ranging from 0 for black to 1 for white, where 0 is at the tip and 1 is on the surface of the hexacone as shown in Figure 10.

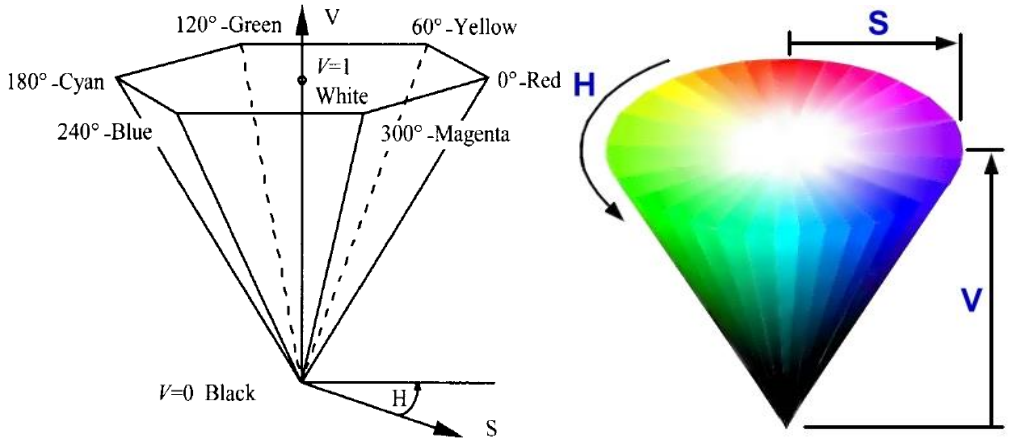

Figure 10: *Hexacone and cylindrical representation of HSV colour model*

Changes within this colour space follow a perceptually acceptable colour gradient. From an image

analysis perspective, it allows the separation of colour from lighting to a greater degree [29]. The HSV model is based on cylindrical coordinates and a nonlinear transformation of the RGB system. Hence, it is possible to directly transform a colour from the HSV system to the RGB system, and vice versa [29]. HSV space decouples the brightness information from the colour information. Thus, HSV has one layer for brightness information, i.e. V, and two layers for colour information, i.e. H and S. It is widely used in artificial vision systems, as it is a powerful tool for the development of a digital image processing algorithm based on the human colour perception model. The HSV model is perfectly suited to portraying colours in practical terms for human understanding and is, therefore, ideal for medical application where the human eye is the ultimate diagnostic tool. It is widely used in artificial vision systems, as it is a powerful tool for the development of digital image processing algorithms based on the human colour perception model. Indeed, the HSV model is well suited to characterising colours in practical terms for human interpretation, differently from the RGB and CMYK models [29].

2.3.2 Mathematical Morphology in Image Processing

The image obtained by **Per**ipheral **Sen**sory **N**europathy **T**est (PerSeNT) is processed and converted into binary image. Further the morphological operation known as ‘closing’, is used to connect objects in a binary image that are close to each other, or to fill the gaps in the object by using a structural element.

Mathematical morphology is one of the most dynamic areas in image processing; it deals with the study of shapes, using mathematical theory to define shapes using sets. Mathematical morphology is a tool used for extracting image components, useful for representation and description. It is used to investigate the interaction between an image and a certain chosen structuring element. The techniques were originally presented by Matheron and Serra at the Ecole des Mines in Paris [32].

The impetus comes from the collection of structural information about the image domain. Mathematical morphology contents are entirely based on set theory. Based on set operations and logical operators, many useful operators are defined in mathematical morphology [32]. It is a collection of nonlinear processes that can be applied to an image to remove details smaller than a

certain reference shape, i.e. structural elements (*SE*).

Mathematical morphology stands quite apart from traditional linear image processing, since the basic operations of morphology are nonlinear in nature, and thus make use of a totally different type of algebra to linear algebra [33].

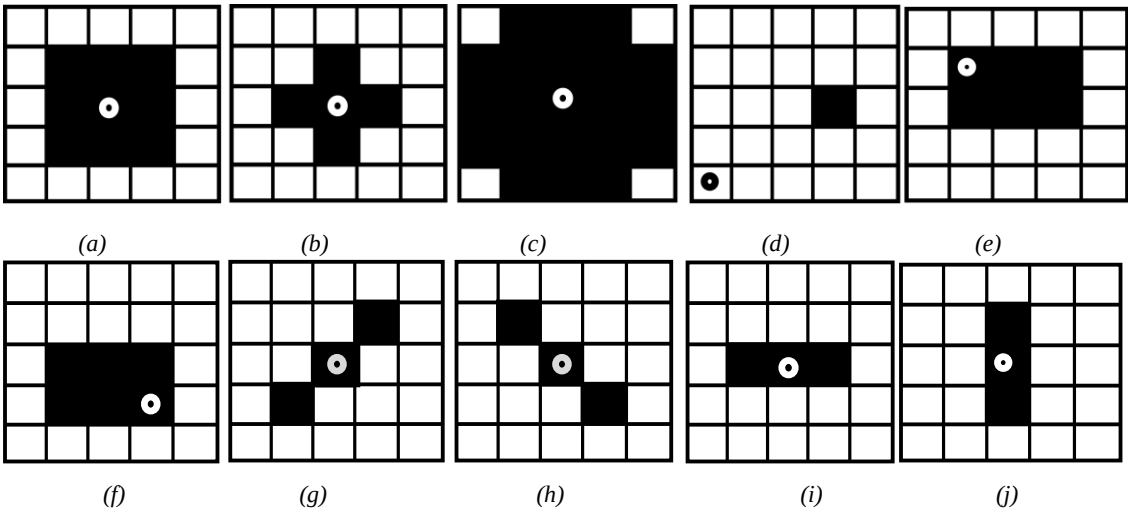

***Figure 11**: Some possibilities of 5 × 5 square structuring elements are shown. They are named as: (a) N8 (8-neighbour-hood centred); (b) N4 (4-neighbourhood centred); (c)Flat plus; (d) Shifted version; (e) 2 × 3 sized rectangular; (f) Reflected structuring element of Fig. (e); (g) Line-structuring element of 45°; (h) Line-structuring element of 135°;(i) Horizontal structuring element with size 1 × 3; (j) Vertical structuring element with size 3 × 1 [32]*

The structuring element in a morphological operation plays a central role in determining its shape and size. Shape and size are defined by the numbers of 0s and 1s in the structuring elements [32]. The resultant value is applied on the circle shown in Figure 11 and called the centre pixel. This circle can be anywhere in the structuring element according to the user's perception, generally occupying the centre of the structuring element.

Morphological operation works as follows.

A mask representing a structuring element is slid over the binary image to be modified in such a way that it is centred over every pixel at some point. When the mask is centred over a region of the image, a logical operation is carried out on the pixels covered by the structuring element, yielding a binary output. Morphological image processing is like a convolution process, as shown in Figure 12.

Like the convolution kernel, the structuring element can be of any size, and it contains a complement of 1s and 0s. At each pixel position a specified logical operation is performed between the structuring element and the underlying binary image. The binary image result of that logical operation is stored in the output image at that pixel position [32]. In its approach, pattern recognition by mathematical morphology consists of analysing the relationships between an object, a subset of R, and its environment using structuring elements, i.e. predefined geometrical sets [34].

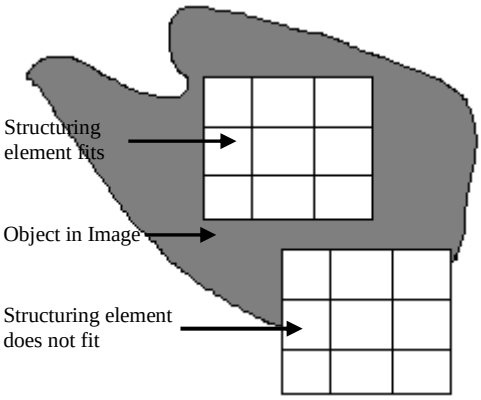

***Figure 12**: Morphological image processing [32]*

From a geometric perspective, the most morphological idea is to examine an image with a structural element and mark the locations at which the structuring element fits within the image, deriving from this structural information concerning the image. This information depends on both the size and shape of the structuring element, and, as emphasised by Matheron, the nature of that information is therefore dependent on the choice of the structuring element [33]. Nonlinear image processing is two-fold in nature; it is fundamentally both geometric and logical in character [33].

Numerous sophisticated and efficient morphological architectures, algorithms, and applications have been developed by researchers. One may be interested in morphological techniques such as filtering, thinning, and pruning for image pre-and post-processing [35]. Mathematical morphology can also be used as the basis for developing image segmentation procedures with a wide range of applications, and it also plays a major role in procedures for image description [32].

Morphological operations can simplify image data while preserving their necessary shape characteristics and eliminating irrelevancies; additionally, they can extract shape features such as edges, fillets, holes, corners, wedges, and cracks using structuring elements of varied sizes and shapes [35].

Mathematical morphology is also known as the study of shape. In image processing, mathematical

morphology is used to study the interaction between an image and structural elements using the basic operations of erosion and dilation. Unlike traditional linear image processing, the basic operations of morphology are nonlinear in nature, thus implementing different types of algebra to linear algebra [36]. Morphological operators aim to extract the relevant structures of the image by probing the image with another set of given shapes, i.e. structural elements.

Dilation and erosion are the two elementary morphological operators, and all other operators are based on the combination of these two [37].

In dilation, the 'rich get richer' and in erosion the 'poor get poorer'. In dilation, the centre or active pixel is set to the maximum of its neighbours and in erosion it is set to the minimum of its neighbours, i.e. dilation tends to expand edges, borders, or regions while erosion tends to decrease or even eliminate small regions [34]. Since both operations are nonlinear, they are not invertible i.e. one followed by the other will not generally result in the original image.

The bases for the above two basic operations are Minkowski basic operations. For any given two sets, *A* and *B*, the Minkowski addition and subtraction are given below [36].

Minkowski addition - $$A \oplus B = \bigcup_{\beta \in B} (A + \beta) \quad 1.5$$

Minkowski subtraction - $$A \ominus B = \bigcap_{\beta \in B} (A + \beta) \quad 1.6$$

where β is the element(s) that comprises set *B*.

Dilation is an operation that grows or thickens objects in a binary image. The specific manner and extent of this thickening are controlled by structural elements.

On the other hand, the key process in the dilation operation is the local comparison of a shape, called a structural element, with the object to be transformed. When the structural element is placed at a given point and it touches the object, then this point will appear in the result of the transformation, otherwise it will not.

Dilation – $$D(A,B) = A \oplus B = \bigcup_{\beta \in B} (A + \beta) \quad 1.7$$

Or can be expressed with *A* and *B* as sets in *Z* (means binary image)

$$A \oplus B = \{z \mid (\tilde{B})_z \cap A \neq \Phi\} \quad 1.8$$

Where $\tilde{B} = \{-\beta \mid \beta \epsilon B\}$ and Φ is the empty set and B is the structural element. The equation 1.8 shows that dilation of A by B is a set of all displacements z such that $\tilde{B}$ and *A* overlap by at least one element [38].

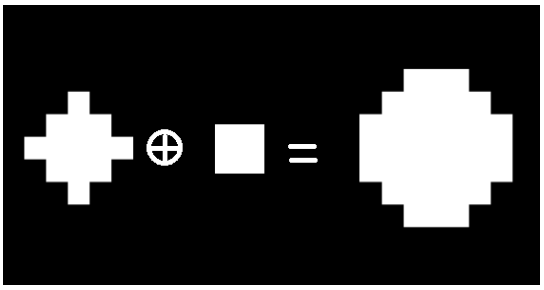

Figure 13: *Dilation operation with a square SE*

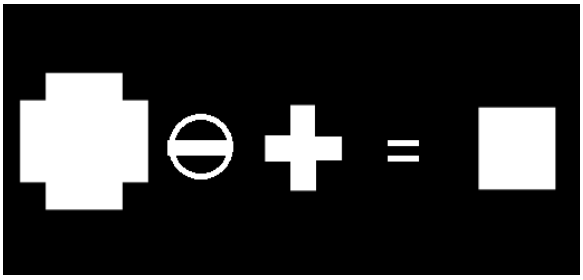

Figure 14: *Erosion with a cross-shaped SE*

For example, Figure 13 shows an original object and the result of its dilation by a 3×3 square structural element. In other words, the dilation of *A* by *B* is the set consisting of all the structural element origin locations where the reflected and translated *B* overlaps with at least some portion of *A*.

Unlike dilation, erosion shrinks or thins the object in an image. The shrinkage of the object is controlled by structural elements.

Erosion – $$E(A,B) = A \ominus \tilde{B} = \bigcap_{\beta \in B} (A - \beta) \quad 1.9$$

Or can be written as

$$A \ominus B = \{z \mid (B)_z \subseteq A\} \quad 1.10$$

Erosion of *A* by *B* is the set of all points z such that, shifted by *z* is contained in *A* [38]. The key mechanism under the erosion operator is the local comparison of a shape, called the structural element, with the object that will be transformed. If, when positioned at a given point, the structural element is included in the object then this point will appear in the result of the transformation

(otherwise it will not). Figure14 shows an object and the result of its erosion by a 3×3 cross.

The above basic morphology operations are used to facilitate noise removal from images, as edge detectors, to carry out image compression and conduct feature extraction [36].

Erosion and dilation are the building blocks of an important operation of morphology called opening and closing. Both of these operations have been used in the image processing program in the developed algorithm to remove noise; combined, the plantar surface patches appeared in the foot binary image because of the poor light [37].

If erosion is followed by dilation, the operation is termed **opening**; if the image is binary, this combined operation will tend to remove small objects without changing the shape and size of larger objects. If the order is reversed and dilation is performed first followed by erosion, the combined operation is called **closing**. Closing connects objects that are close to each other, tends to fill up small holes and smoothes an object's outline by filling small gaps [80]. A mathematical representation of opening and closing for image A and structural element B is given in equation s (1.11) and (1.12) [37]:

$$O(A, B) = A \circ B = D(E(A.B),B) \qquad 1.11$$

$$C(A, B) = A \bullet B = E(D(A,\tilde{B}),\tilde{B}) \qquad 1.12$$

where O, *C*, *D* and E are opening, closing, dilation and erosion, respectively.

2.3.3 Digital Image Processing in Medical Applications

Image processing gained popularity in different areas of research. In the past, it was limited to satellite imagery [29]. The influence and impact of digital images on modern society has been incredible, and image processing is now a significant component of science and technology. The most speedy progress in reconstruction of computerised medical image, associated developments in analysis methods and computer-aided diagnosis, has made medical imaging one of the most important sub-fields in scientific imaging [39]. In the past few years, the influence of digital image processing has been felt in the medical and healthcare domain. A multitude of diagnostic medical imaging systems are used to examine the human body. They comprise both microscopic (viz.

cellular level) and macroscopic (viz. organ and systems level) modalities. Interpretation of the resulting images requires sophisticated image processing methods that enhance visual interpretation and image analysis methods and consequently provide automated or semi-automated tissue detection, measurement, and characterisation [39].

These images contain a lot of information and can be exploited for better understanding. Extracting information from images and analysing them requires special techniques. Image processing is a technique that involves image interpretation, image enhancement and segmentation of the area of interest [40].

In many medical applications, X-rays, which traditionally exist as greyscale images, are used to diagnose. The visualisation of nuance areas is improved by transferring the grey image into pseudo colours [27]. The interior portion of the body can be seen using imaging technology in medicine, and consequently the diagnostic process is improved. It also helped surgeons to reach interior parts of the body without invasive procedures [29].

Since the discovery of X-ray by Roentgen in 1895, imaging techniques have evolved into magnetic resonance imaging (MRI) and computed tomography (CT). Imaging technology has progressed greatly, the focus having now shifted from the mere generation and acquisition of images to post-processing and the management of image data [40].

Some research studies carried out skin tumour classification based on colour image processing. An accurate evaluation of a pigment sample and a hue typical of a melanocyte are necessary for classification. In [41], the automatic classification of skin tumours based on feature extraction using several neural networks is discussed without practical realisation.

Diabetes-related eye diseases are the most common causes of blindness in the world. Early detection is the prime key to effective treatment. H. Wang et al. [42] employed image processing techniques to automatically detect the presence of abnormalities in the retinal images. The approach combines brightness adjustment procedures with statistical classification methods and a local window-based verification strategy.

A productive way to effectively (with accuracy of 96.25%) segment malignant melanoma in colour dermoscopy images is presented by [43]. A combination of methods, including smoothing filters, PSNR, spline, edge detection, morphological operations and segmentation, is used to discriminate malignant melanoma boundaries [43]. This process employs the spline function, followed by noise removal, to improve edge detection, while morphological operations are used to segment the lesion from the image.

An automated gastroscopic image lesion detection method has been designed by [44]. Two multi-scale textual features, contourlet transform with grey level co-occurrence matrix (GLCM) and local binary pattern (LBP) respectively, are employed and compared respectively.

2.4 Lesion Detection

Automatic lesion detection also is a challenging issue because of the presence of inconsistencies in lesion appearance. Wounds have great variation in shape, low contrast between lesion and the surrounding skin, irregular or fuzzy boundaries, variegated colouring inside the lesion, and artefacts such as skin lines, hairs, black frames and blood vessels [45, 46]. Further complexity is created by slough and coagulated blood in and around the lesion, which can, due to the influence of some dressing materials, cause the wound colour to alter [46].

Imaging is already used to diagnose abnormalities within the body, e.g. X-Ray, dermoscopy, magnetic resonance imaging (MRI), thermal imaging, Nevoscope, gastroscopy, fundus camera, CCD colour camera. An expert is needed to read images produced by the above mentioned devices. Skin lesions are detected and classified based on different features, and are characteristically evaluated by dermatologists using the "ABCD" rule, an easy guide to analysing the asymmetry, border irregularity, colour variation and diameter of a lesion. Practically, rules A, B, and C analyse texture information, and this confirms the importance of texture [51].

In the domain of automatic lesion detection using image processing techniques, much research has been carried out, ranging from simple edge-based detection and greyscale segmentation to sophisticated statistical analysis of colour and patterns using different image capturing devices and techniques including dermoscopy, MRI, thermal imaging, Nevoscope, gastroscopy, fundus

camera, and CCD colour camera. Neither of the algorithmic approaches using current imaging techniques developed so far could produce a robust solution [47].

A. Chodorowski et al. evaluated a semi-automatic real time segmentation method called livewire to find the boundaries of oral lesions [48]. The live wire technique is considered a member of the active contour model, which is also known as the snakes model.

Another piece of research was carried out to effectively detect malignant melanoma in the colour images produced by dermoscopy [49]. The techniques used consisted of a combination of methods, including average, median, bilateral Gaussian filters and PSNR spline, to reduce the noise and smoothing of the image; additionally, canny and zero crossing edge detection were used to detect the edge around the skin and segment the lesion by morphological operations. The research was specific to malignant melanoma and showed 96.26% accuracy. It cannot be used as a generic approach to detect all sorts of lesions. Moreover, the filters used in the research are unable to preserve the details used to detect early stage lesions related to the plantar surface.

Automated analysis of retinal lesions using image processing is conducted by many researchers. A particular effective method used Lab view. A novel technique is presented to diagnose the lesion through fluoresce in angiographic images using virtual instrumentation [50]. Clinical photographers usually capture colour images of the retinas of the patients suffering from retinal diseases. A fluoresce in dye is injected into a vein in the subject's arm. Several pictures are taken, by a colour fundus camera, as the dye propagates through retinal blood vessels. Once vessel extraction is carried out from the two fluoresce in images, these two images are then aligned and fused to identify the region of abnormality and lesion growth. The colour image is converted into a greyscale *I* mage and binary images are created using iterative thresholding. In iterative thresholding, the image is segmented into background and foreground sections with the threshold *T*. The averages (*T1* and *T2*) of the two sets are calculated and a new threshold *T* is calculated by taking the average of *T1* and *T2*, i.e.

$$T = \frac{T1+T2}{2}. \qquad 1.13$$

The process is repeated until the new threshold matches the previous threshold. Morphological operation is used to remove small objects from the image obtained from iterative thresholding. Fusion of the two images is used to isolate invariant geometric features. The most common invariant features observed in this specific kind of retinal image are the optic disc, optic vessel image edges and Y-features [50]. The images, taken during fusion with the same alignment and containing Y-features, are compared in terms of pattern matching. Any discrepancy in the propagation is indicated as a dark or bright spot because of the leakage of flow.

Sophisticated research is undertaken by [51] to automatically detect tumours related to breast cancer, i.e. computer-aided tumour detection. Breast cancer has emerged as one of the prime mortality causes among females in Europe and North America. The chance of survival is directly proportional to the stage at which the cancer is detected. To assess a high number of mammograms, a computer-aided diagnosis is proposed. The proposed system potentially eases the radiologist's workload by filtering out truly negative cases, so only suspected positive cases will be referred to experts. To achieve the overall goal, the research has several main phases:

Phase 1: Suspected locations are to be found.

Phase 2: Foreground 'lesion' to be extracted from background 'skin'.

Phase 3: The shape of the foreground is to be characterised.

In phase 1 a dual binarisation with combination of Bezier-smoothed histogram is used. Since there is no global threshold to apply in all situations to extract a required object in an image, an adaptive approach is used. Morphological operation is used to reduce the noise in the binary image. As tumours generally have a specific shape, a shape description method is used to decide whether the object in question is tumour or not suing textural analysis by histogram. Two methods were used in this regards moment-based method and principal component analysis (PCA) on the binarised images is applied. The proposed method was trialled on 71 images and the detection rate was 93%.

Support vector machine (SVM) is a pattern recognition technique which learns to assign labels to objects through training. It has been used for oral lesion classification by C. Artur et al. [52]. Only

two lesion types related to oral were considered namely oral leukoplakia (a pre-cancerous lesion) and oral lichenoid. A digitised colour image of human oral cavity is obtained and an assumption is made that size, orientation and position of the lesion have no impact on the decision [52]. The features used for SVM were based largely on shape and colour namely solidity, eccentricity, form factor, roundness, area factor, difference in intensity, hue, saturation, transition area, hue and saturation within the lesion area, intensities differences, hue and saturation between adjacent area and the lesion area, normalised Fourier descriptors and colour histogram. They found 89% success rate in a two class problem i.e. pre-cancerous and non-pre-cancerous and 78% into four classes i.e. leukoplakia, lichenoid, normal area and transition area [52].

The adopted approach is specific to two types of oral lesions and the assumption doesn't fit for large domain of lesions. The required approach for automated peripheral sensory neuropathy assessment using optical imaging system needs a generic approach.

X. Yuan et al. worked on early skin cancer detection decision support system based on analysis of the pigmentation characteristics of a skin lesion, detected using cross polarisation imaging, and the increased vasculature associated with malignant lesions [53]. The researchers focussed here on texture information to classify the benign and malignancy of the skin lesion. Firstly, pre-processing step is carried out where noise (hair etc.) in the image is removed and conversion of RGB colour space to intensity grey image [52]. The grey image is fed into the input layer where feature extraction is carried out and feature vector space is generated. In the second layer the input spatial imaging space is transformed into nonlinear space [54]. The output layer applies a hyper plane classifier to classify the skin lesions (benign and malignant).

B. A. Abdullah et al. proposed a technique for automated segmentation of multiple sclerosis (MS) lesion. MS affects nerves in the brain and spinal cord, and manifests itself via a range of symptoms including problems with muscle movement, balance and vision [55]. The techniques based on position and neighbourhood of brain textural features. SVM is trained and used to binary classify MS lesions region and non-MS lesions region. Fluid attenuation inversion recovery (FLAIR) images of brain are taken due to a better quality and its high accuracy. The FLAIR images are then pre-processed for intensity correction and noise reduction. The next step involves building the

feature vector space, consisting of textural features like histogram, gradient features, grey level non uniformity and co-occurrence matrix based features [55]. An SVM is trained for the above mentioned feature and use it as a classifier. Post-processing is carries out in the last step to address the false positive and false negative issues.

N. Abdullah et al. used SVM techniques in their research to classify brain MRI image into normal and abnormal brain (brain tumour). The pattern classification based on the fact that there is symmetry in the brain image which manifests in the axial and coronal images [56]. Like any SVM algorithm, the process consists of the training phase and the testing phase. The Flair MRI images of 10 normal and 22 abnormal are taken. Subjects with abnormal images were at the very first stage of brain tumour.

L. Wang et al. research targets the automation of foot ulcer detection, the wound image is captured by an Android smart phone using an image capture box [57]. Foot boundary is determined based on skin colour and the wound extraction is performed by accelerated mean shift algorithm and simple connected region detection method. A quantitative analysis of healing status is carried out by trend analysis for time records for a given patient. The research based on three assumptions; firstly, prior to capturing the image from smart phone, it must be ensured the visibility of wound is high and clear. Secondly, the healthy skin of the plantar surface is nearly uniform and thirdly, the wound is not located at the edge of the foot boundary [57]. The algorithm was efficiently used on wound images collected from a health care wound clinic. Different methods work well on different types of lesions, but no attempt has been made towards a generic approach.

A generic approach has been attempted in this thesis and yet further research is underway to ensure the probe isn't applied to a lesion, if a suspected lesion and the chosen pressure point overlap.

2.5 Conclusion

The SWME incurs its own downsides. The key disadvantage is the potential misjudgement acceptable force. The precision of the accepted 10g force is based on the practitioner's guess by observing the perceived bend or buckle of the filament i.e. observing the 10 mm bend through the naked eye. Therefore, there is a clear need to further, simplify and automate the testing procedure

that is, autonomous, repeatable, and simplifies the testing procedure with the storage capacity of photographic evidence of patients' feet and their condition over time. Previous work based on semi mechanical selection of three test points is compared. Selection of pressure points from pressure region is vital and provides key information to be used in medical diagnosis associated with satisfactory function in the foot. Plantar pressure measurements systems ranges from simple system to more complex system. These systems come into two design platform and in-show. Further these can be classified into qualitative and quantitative measurements. Though their research objectives are diverse, the methods followed by those referenced involved manual intervention. Image processing gained popularity in medical applications. Most common colour spaces used in image processing are RGB and HSV. Dilation, erosion, opening and closing are the building blocks of basic mathematical morphology operations in image processing. Many algorithms have been developed and under further research to detect specific lesions.

CHAPTER 3. Automated SWME System Design

This chapter discusses the physical design and attributes of the Periphery Sensor Neuropathy Test (PerSeNT) system. It was essential to make a system that copied the SWME method closely by scanning the foot and finding the pressure points. Subsequently enabling a probe to be applied to those pressure points detecting (or not) PSN. Importantly the system should be automated, have a unique scanning and probe all-in-one capability, portable, provide repeatable testing and provide photographic evidence of test, again a unique feature. This charter describes the overall system architecture. A physical description of the system is presented which aims to assist the readers understanding of the design and the subsequent embedded system development.

3.1 PerSeNT System architecture

In order to provide an automated SWME experience the system must be able to replicate a health practitioner carrying out a typical SWM examination. That is to scan a user's foot, find the pressure points, apply a 98mN probe and for the user to declare a yes or no to the probe application. The system presented contains a scanning (image capturing) section, subtended by a perforated sheet that would (a) enable the foot placement and scan, and (b) permit the subsequent probe application. The probe mechanism was fabricated in-house using precision components and a commercial amplifier. This assembly is driven by stepper motor controlled rails in both the X and Y-axes. A further Z-axis stepper motor is then used to drive the probe onto the plantar surface to apply exactly 98mN. If the patient feels the probe, they record their response by pressing a handheld button which is wired into the microcontroller. The original algorithms related image capturing and test points extraction will be explained later in the thesis. An overall schematic and photo of the individual physical parts of the PerSeNT system are shown in Figures 27 and 28 respectively. Each of the essential components will be subsequently explained.

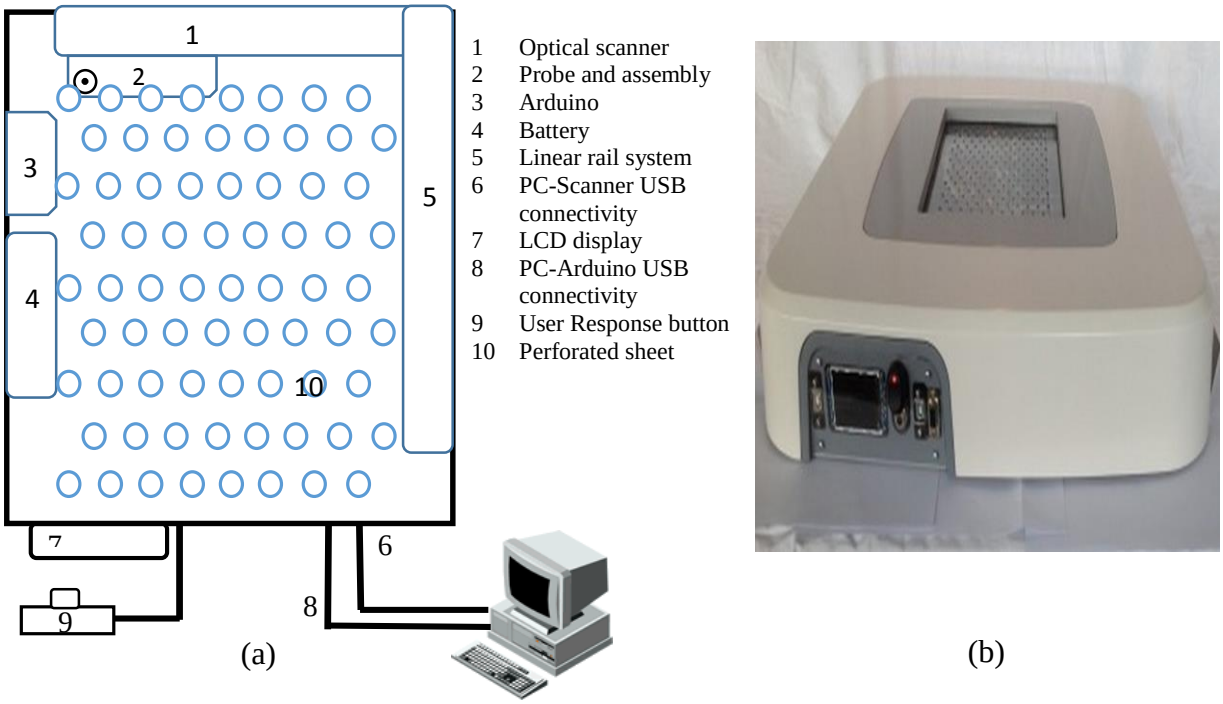

1 Optical scanner
2 Probe and assembly
3 Arduino
4 Battery
5 Linear rail system
6 PC-Scanner USB connectivity
7 LCD display
8 PC-Arduino USB connectivity
9 User Response button
10 Perforated sheet

Figure 27: *(a) PerSeNT schematic diagram, (b) Actual (PerSeNT) device*

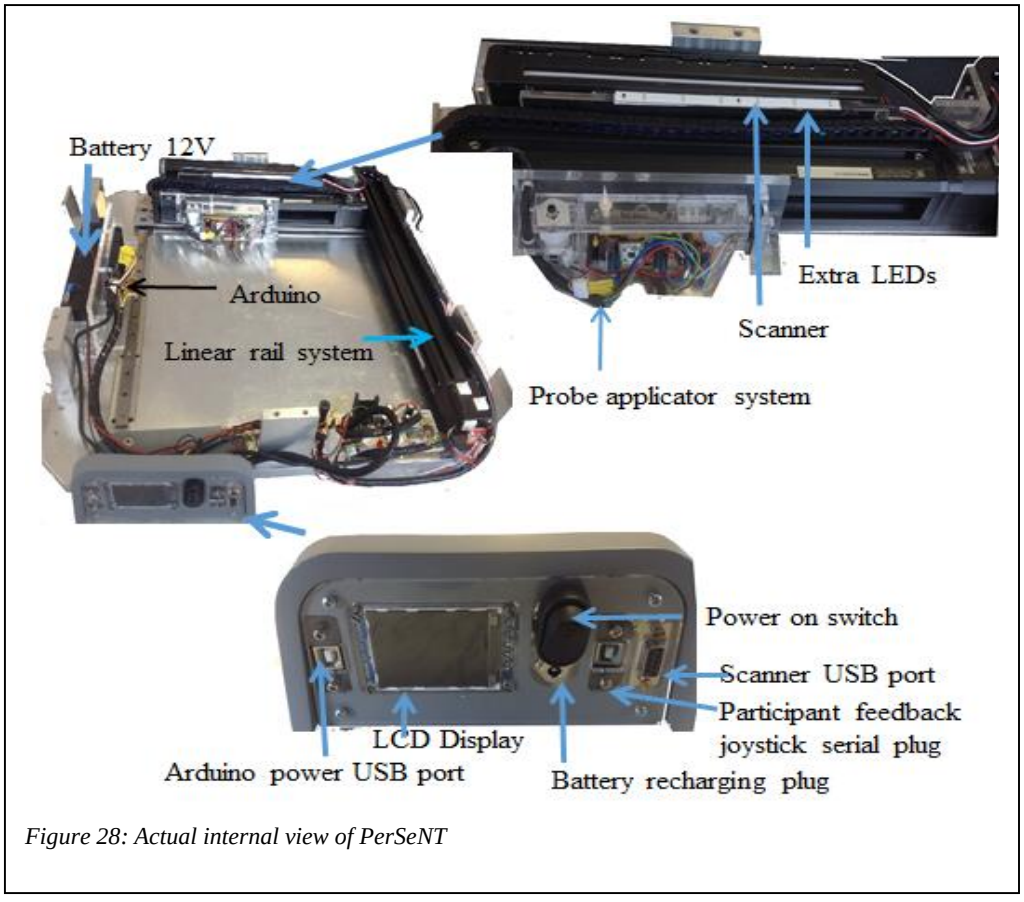

Figure 28: Actual internal view of PerSeNT

Details of major parts of the system are explained:

3.1.1. Raspberry Pi (RPi)

RPi is a microprocessor based single-board computer (SBC). It has a BCM2835 system-on-chip (SoC module) provides general purpose processing, graphics rendering and input/output capabilities [88]. Stacked on top of the chip there is a RAM. It has 8 I/O interfaces. Above and below the chip, there are two video outputs. The silver colour is an HDMI socket for modern TV or monitor and the above (in yellow) is for the older TVs. For audio streaming there is a separate 3.5 mm audio jack just right of the composite video socket. General purpose input-output (GPIO) pins are mounted on the top left corner of the Pi. It is used to connect Pi with other hardware. Generally, it is used to connect an add-on board. Below the GPIO port is the display serial interface (DSI) port for digital flat display systems. On the right of the HDMI port, a camera serial interface (CSI) is mounted to connect camera to RPi. Power socket (micro USB socket) to power the RPi is stacked at very bottom left on the board. Underside of the RPi on the left hand side there is a secure digital (SD) memory card slot. SD card provides storage for the operating system, programs, data etc.

Figure 29: *Raspberry Pi*

There are different connectors on the right edge of the RPi depending on the model of RPi. The RPi comes as two model basis Model A, and Model B. Model A comes with single USB port and limited 256 MB Read Access memory (RAM), moreover it doesn't have Ethernet port, while the model B has two USB ports and an Ethernet port. The RPi has low power consumption, the model B draws at most 3.5 W only [88].

3.1.2 Perforated Sheet

This sheet is where the subject places their feet for the test and shown in Figure 30. It consists of a polycarbonate glass sheet that is 30cm long, 21cm wide and 1 cm height perforated in 18 rows. Each row has 11 holes with diameter 4mm equally 1 cm spaced i.e. total perforations are 198. The equidistance holes on the perforated sheet permit the mechanical probe (discussed later) to pass through for required force application.

Figure 30: *Perforated sheet*

3.1.3 Optical Scanner Mechanism

Copy Cat is a handheld, portable scanner used to capture books, papers, photos and other documents. It is a light weight high resolution, up to 600 DPI resolution capabilities, scanning device [89] as in shown in Figure 31. It stores images in a micro SD card. It can be connected to the RPi as a USB drive using USB type B cable. It works as USB memory card when plugged into a computer.

Figure 31: *Portable scanner*

It inherits a limitation in terms of scanner mode and memory mode. It serves as a scanner when disconnected with RPi and serves as a USB drive when connected to RPi. An in-house created circuitry and code was developed to toggle between scanner mode and USB memory mode.

3.1.4 Arduino Mega/UNO

Arduino is an open source physical computing platform, shown in Figure 32, based on a simple microcontroller board and a development environment for writing software for the board.

On the left edge, there is a Universal serial bus (USB) that connects the board to computer for power supply, uploading the sketches (computer program for Arduino) and for serial communication. Below the USB connector there is another alternate poser connector. At lower middle of the board is the processor "Atmega328P-PU". Two small sockets in a row are mounted just below the microprocessor. The one set on left is for power and the other set contains sockets (A0 to A5) for analog data. Along the top of the board is another row of sockets numbered 0 to 13 (digital I/O).

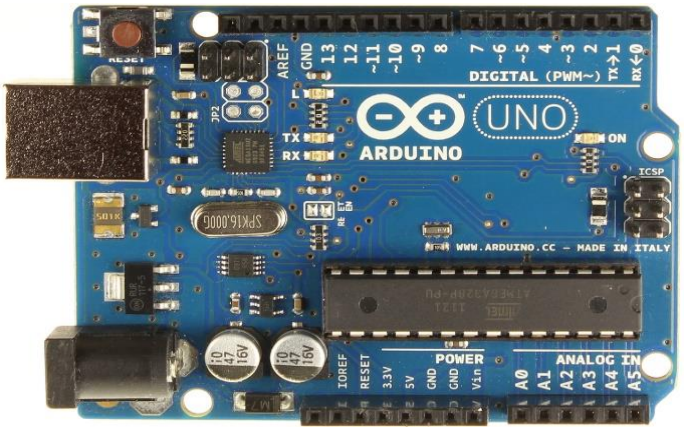

Figure 32: *Arduino UNO*

In the system, Arduino UNO controls the scanner modes toggling, controls the mechanical probe movement in x and y direction, and controlling the force sensor to make sure 10g force is applied on the plantar surface through mechanical probe.

3.2 Automated Peripheral Sensor Neuropathy (PSN) Algorithm Design and Test

A unique approach to automate the Semmes–Weinstein Monofilament Examination (SWME) is proposed in this thesis by exploiting optical detection and binary image processing. Although the SWME method is one of the most common tests used to identify PSN and increased risk of ulceration, through the examination of five pressure points at specific weight-bearing areas, namely the toe (hallux), metatarsal, and heel (Calcaneum).

An extruded homopolymer monofilament (SWM) probe is applied by a trained clinician. The SWM is designed to bend by 10mm (gauged commonly by sight) when 10 g (98 mN) force is applied. Studies have shown that the inability to detect the SWM, when it bends by 10 mm at 10 g force, indicates a degree of neuropathy. The rationale for this is based upon World Health Organization (WHO) and National Institute for Health and Care Excellence (NICE) guidelines, which indicate that reduced sensation to a high-pressure site is an accepted risk factor for the

development of ulceration [90]. Currently, professionals rely on subjective judgment as to which areas may constitute a high-pressure site; this is frequently based upon bony prominences, deformity, or soft tissue indicators. On this basis, it is the gold standard that all these identified areas are then tested for PSN (a risk factor for the development of ulceration). The SWME, although the most widely used, is considered cumbersome and labor intensive. Repeatability is difficult to maintain and testing can be prone to experimenter bias. Moreover, this issue may be amplified when a patient is seen by a different practitioner on each visit [91]. Further the number of sufferers reached to such a huge number that made it unfeasible for the podiatrist or health expert to attend each patient individually. Thus an automated system that replicates the traditional manual SWMME is the need of the time. This test replicates the same protocol as the WHO and NICE standard test for this risk factor.

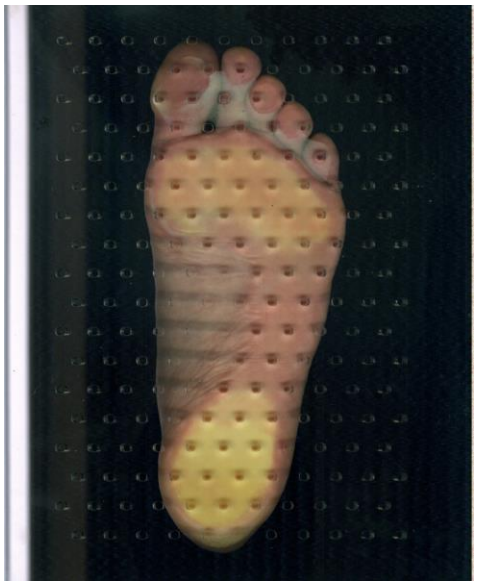

***Figure 33**: Image taken of foot resting on perforated sheet*

Overall the system schematic and actual design is shown in Figures 27 and 28 respectively. Here the fibre glass perforated sheet rests on a scanner structure with built in mechanically driven probe element. The optical scanner section is used to obtain the image of the plantar surface of the patient. The built in perforated fibreglass sheet that has two purposes

(a) To enable a clear optical image of the plantar surface.

(b) Holes within the sheet permit probe to pass through so that the accepted bend by 10mm when 10g (98mN) of force can be applied.

To reduce overall system software and hardware complexity holes on the sheet are equidistant in both the horizontal (x) and vertical (y) domains as shown in Figure 33.

The image has a resolution of 300 dpi to aid the visualisation of the patients' pressure points. The orientation of these pressure points was evaluated in x, y domains by an image processing application developed as part of the research. The localisation information is then sent to a micro controller (robotic-arm with monofilament probe) controlled serially by a computer. The

microcontroller drives two stepper motors, to give x and y directional control. The movement of the monofilament probe in x, y direction is dictated by the results (pressure points stream) of the image processing found from Figure 33 and will be discussed subsequently. To aid the movement of the robotic arm a reference point is used along z-axis and directs the probe to move vertically up & downward accordingly to specific degree so that the probe reaches the specific pressure points of plantar surface required number of times (possibly three times) and force (10g (98mN)). The image processing development from the initial foot image algorithm development consists of a number of discrete repeated steps

1. Obtain an image in RGB
2. Convert the image into HSV (grey colour) colour space
3. Turn all the pixels' colour white that come in specific range (human plantar colour range)
4. Dilate, Erode and Smooth the image to remove noise
5. Draw counters of resulting binary image
6. Calculate the central point of specific contours (polygon) in terms of coordinates
7. Send these points to micro controller
8. Execution of micro controller.

The image shown in Figure33 is taken as the obvious starting point. The software for image processing was developed in C/C++ using OpenCV library. The image in Figure 33 is converted into a black and white, binary (threshold) image as shown in Figure 34(a).

Using existing OpenCV library functions (cvInrange() and cvInranges()) the image can be specified into explicit colour ranges. These two functions can be used to clarify if the pixels in an image fall within a particular specified range. In the case of cvInRange(), each pixel of source image (such as that shown in Figure 33) is compared with that particular specified range. If the pixel's value in source image is outside of the specified range, here the specified range is the colour space of pressed plantar areas with the said contact surface, then the corresponding value in destination will be set to 0 (Black); otherwise, the value in destination image will be set to 1 (white).

Further analysis on generic colour space is ongoing to account for different patient ethnicities. The function cvInRangeS() works exactly the same way except that the source image is compared to the constant (CvScalar) values in lower and upper [92]. Once an image in binary form is obtained, edge detection becomes less complex. From here the foot boundary is obtained and subsequently the pressure point coordinates are calculated. Library functions cvFindContours() detect edges and computes the contours, while approxPolyDP() function draws a polygon of these contours [92]. Two dimensional dynamic array (vector) of type Points are used to store these contours. The boundingRec() function bound each contour in a rectangle by calculating the extreme contour points.

3.2.1 Finding the Pressure Points of a Plantar Surface

When a foot is pressed against a surface in the normal manner some parts of plantar surface are in greater contact with the said surface and experience more pressure than other parts of the foot [64]. The area of interest for this research is the plantar surface that are in greater contact with the surface as the pressure points lie in those areas, as can be seen from the scan of a foot in Figure 33. Figure 34(b) shows the resulting contours bounded by rectangles and can be identified by their sizes. Toe contour (hallux), Contour (metatarsal head), Heel contour (Condyle). The pressure points are now easily recognizable. From here a decision is made where to apply the probe. The central point o f a polygon is obtained by the equation given below [93].

$$T_x = \frac{1}{6A_T}\sum_{i=0}^{N-1}(X_i + X_{i+1})(X_iY_{i+1} - X_{i+1}Y_i) \qquad (3.1)$$

$$T_y = \frac{1}{6A_T}\sum_{i=0}^{N-1}(Y_i + Y_{i+1})(X_iY_{i+1} - X_{i+1}Y_i) \qquad (3.2)$$

Where A_T the area of the polygon and T is the central point with coordinate (T_x, T_y). The pixels in an image are arranged so that the top left pixel has coordinates (0, 0) and bottom right pixels has maximum width and height values as coordinates as shown in Figure 35.

The centre of toe polygon (contours) can be calculated using above polygon centroid equations (3.1) and (3.2). For clarity the central point of these polygons are taken as the centre of circles of

equal radius. Specific points must now be chosen at different locations on these polygons to represent the probe contact pressure points. For the metatarsal head areas, three areas are chosen based on the pressure images provided by health experts as shown in the Figure 34(b). Three circles are chosen but this number can be increased or decreased depending on requirements. The above formulae provide the centre of the polygon that will give one circle in the middle. To create the circles at right and left edges, lowest and highest x-coordinates are obtained in the contour respectively.

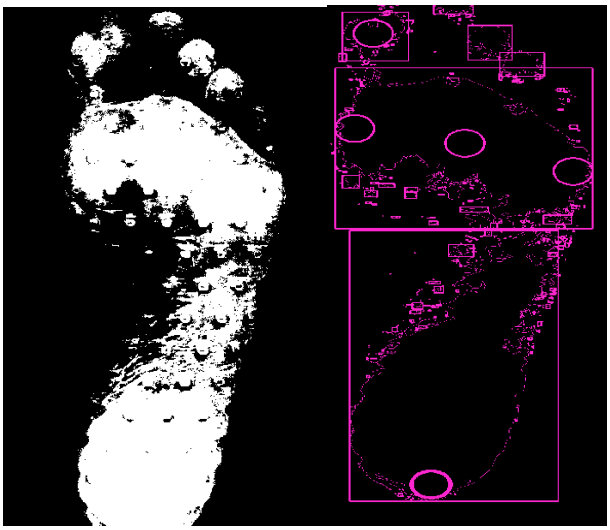

(a) *(b)*

Figure 34: *(a) Binary image from Figure 33; (b) Contours polygon/circle*

For the right most circle on metatarsal pressure point area, largest x coordinate (to get the right most point of the contour) of the contour is taken providing an arc on the right most part of the metatarsal pressure point area.

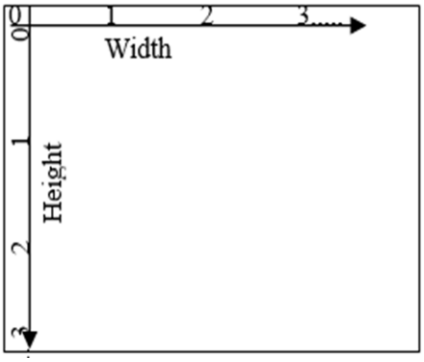

Figure 35*: Pixel image dimensions*

Figure 36*: Edge of heel*

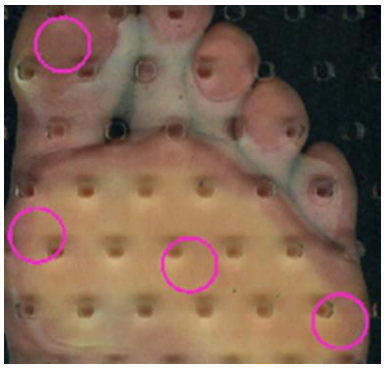

Figure 37*: Mismatching of circle's centre and holes of holey sheet*

The heel polygon (contours) requires a circle positioned at the edge of the heel colour contrast shown in the Figure 36.

As contours are stored in two dimensional vectors points, the above location can be identified by finding the largest height (y- coordinate) values in these contours. The largest height value of

contours should logically always be located at the edge of the heel. This of course will be tested further for reliability. Once the circles are determined, it must be ensured that they align fully with an entire hole on the perforated sheet to enable appropriate pressure application and to avoid probe damage. Although the probe pressure points have been determined, it does not mean a probe point will align appropriately with the centre of these circles as shown in Figure 37.

In order to ensure that a probe point is found accurately within the pressure circle, the following method is applied.

a) The first top left hole on the perforated sheet is taken the reference point as shown in the Figure 38. This will remain as the reference coordinates for all further processing and images are aligned to match this reference point. The top left hole from a fixed image is now known as "ref coordinates" and has fixed coordinates (156,107). Furthermore, the pressure point is taken as the center of the circle with coordinates (X_c, Y_c). Since all the holes are equidistant (row-wise 88 pixels) and columns (column-wise176 pixels), (excluding at the moment bowing from heavy feet (currently being analysed). This then helps to identify the position of all holes.

b) Identify the closest hole on perforated sheet to the centre of the pressure point circle *C*

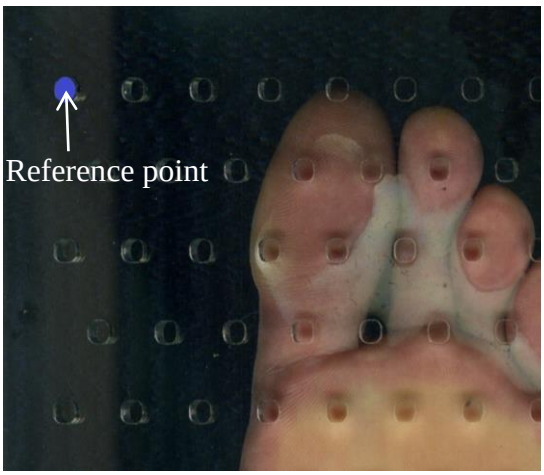

***Figure 38**: Reference point marked blue on perforated sheet*

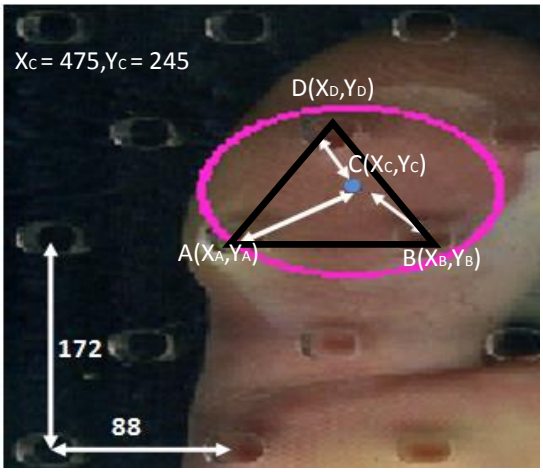

***Figure 39**: Hole coordinates calculation*

The process of selecting appropriate holes on the perforated sheet to apply the probe is same for

all circles. Consider the selection of the closest hole to the extracted test point at toe. The pixel coordinates of the extracted test point "C" at toe is determined i.e. X_c=464, Y_c=245. As shown in Figure 39. Three holes can be seen around the centre of the circle. Euclidian distance formula is applied to obtain the closest hole to the point $C(X_C, Y_C)$. For the distance formula to be applied, coordinates of the three holes around the extracted pressure point must be evaluated.

To obtain the first left hole coordinates (X_A, Y_A) to (X_C, Y_C) where X_C, Y_C are centre of circles coordinates and X_A, Y_A are the coordinate of left hole to the circle's centre.

$X_A = 156 + \{ (X_c/88 \text{ (quotient))} - 2 \text{ if} < 77 \text{ or } -1 \text{ if} >=77\} * 88$

$X_c/88=464/88$ will give 5 as quotient and 35 as remainder so subtracting 2 from quotient will give 3

$X_A = 156 +3 * 88 = 420$

$Y_A =107 +(Y_c/176$(quotient) $)* 176.$

y_c/176= 245/178 will give quotient 1 so

$Y_A = 107 + (1) *176 =107$

Once the coordinates of left hole (*A*) to the centre of the circle are obtained, the other two holes (*B* and *D*) can easily be identified in terms of their coordinates as holes are equidistant as shown in the Figure 39.

For example, adding 88 to left hole x coordinate will give x coordinate of next hole and similarly adding 176 to the y coordinate of hole will give y coordinate of next hole in downward.

Applying Euclidian line distance formula

$$d = \sqrt{(x2 - x1)^2 + (y2 - y1)^2} \qquad (3.3)$$

on *AC, AB, AD,* one can identify the nearest hole that will be entirely within the circle. Hence get the required output as shown in Figure 40.

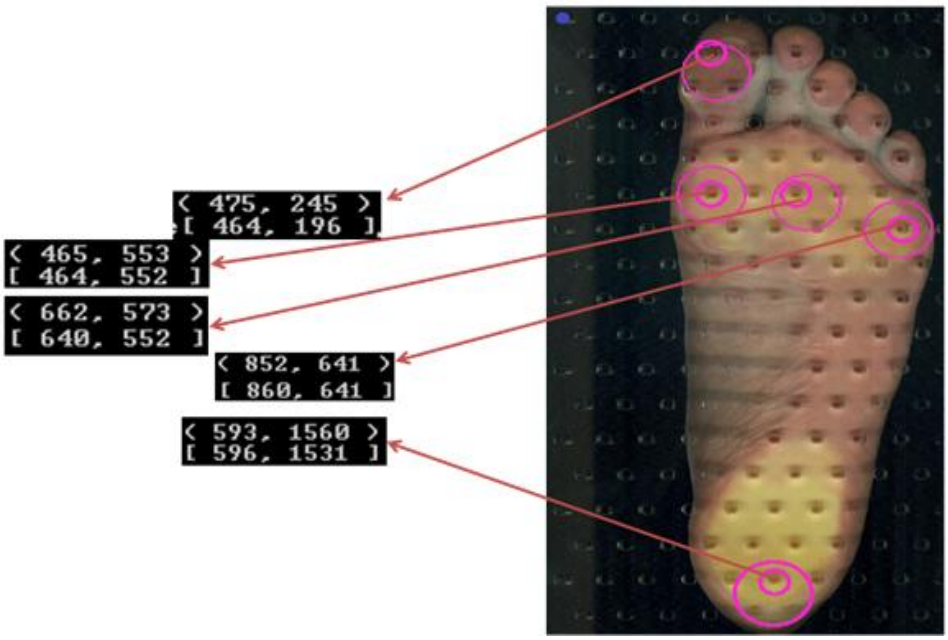

Figure 40: *Selecting the next best closest hole of a perforated sheet to the pressure point*

3.3 Conclusion

The key constituent components of the PerSeNT machine includes a Raspberry pi, Arduino Uno, portable scanner, perforated sheet and stepper motor to control x, y and z directional motion. A novel approach towards automation of plantar surface sensory neuropathy is proposed. In this approach a scanner is used to obtain the patients plantar surface image in RGB colour space. Then via developed image processing using a specific colour space and three largest size of contours, the orientations of pressure points are identified. This information is then sent to a robotic arm holding a monofilament probe. The robotic arm will be used to conduct the SWME procedure as it is conducted in hospital or health care centre manually. The patient's feedback will be recorded to identify the insensate area of plantar surface.

CHAPTER 4. PSN Algorithm Improvements

The previously and initially developed algorithm was specific and used to detect the plantar contact area of one ethnic group (Caucasian) and did not include flat feet probabilities in subjects. In this chapter an improved method is introduced to make the automated pressure area selection on plantar surface independent of ethnicities and to account for non-standard foot pressures. In order to reflect the accepted SWME method, the foot rest again is a perforated sheet enabling a mechanically driven 10g probe to be admitted to the patient's foot through the perforations once the pressure points have been correctly identified via the optical imaging method described. To assist the supervisory development of the programme, a fixed small and soft stud is introduced to the underside of the perforated sheet as shown in Figure 41(a).

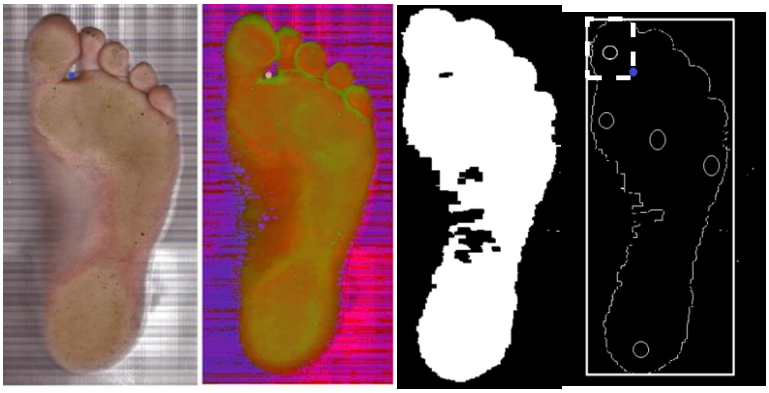

(a) (b) (c) (d)

Figure 41*: From left to right: (a) Plantar image in RGB colour space; (b) Plantar image in HSV space; (c) Binary image; (d) Foot anthropometric reference point and bounded rectangle*

The stud is known as a foot stopper (FS) and has two existence reasons:

1) It helps the patient position their foot on the perforated sheet.

2) It acts as a reference point for the algorithms used to perform the foot anthropometry calculations.

The specific colour of the FS helps in its identification during the image processing of the plantar surface in terms of spatial coordinates. The foot is scanned and then obtained foot image in RGB colour space as shown in Figure 41(a). RGB colour space is generally used for representation, transmission and storage of colour images on analogue devices such as television sets as well as digital devices such as computers, digital cameras, and scanners [94]. RGB is an additive colour

system, where primary colours are combined in different quantities to form other colours. In this space (RGB) a colour is described by indicating the amount of red, green, and blue colour. When all colours have the maximum value, the resulting colour is white and black when vice versa [95]. The primary colours components are highly correlated and therefore difficult to execute some image processing techniques that operate on the intensity component of an image only [31].

An alternative is a perceptual colour space like HSV that is more close to the human perception and understanding of colour [31]. HSV model is based on cylindrical coordinates and it is actually a nonlinear transformation of the RGB system. The importance of HSV space in terms of image processing is the ability of separation of the three components of a specific colour (hue, saturation, and voluminous). It is widely used in artificial vision systems, as it is a powerful tool for the development of digital image processing algorithm based on human colour perception model. HSV model is well suited to portray colours in practical terms for human understanding [96]. Therefore, the scanned foot image is converted into HSV (hue, saturation, value) colour space, Figure 41(b), and then a skin classifier is used as a threshold against the image in HSV space. Let *A* be the HSV image with dimension $M \times N$ and H be the set of human plantar skin colour HSV space.

$$A = \begin{pmatrix} a_{11} & a_{12} & a_{13} & \dots & a_{1N} \\ a_{21} & a_{22} & a_{23} & \dots & a_{2N} \\ & & & \vdots & \\ a_{(M-1)1} & a_{(M-1)2} & a_{(M-1)3} & \dots & a_{(M-1)N} \\ a_{M1} & a_{M2} & a_{M3} & \dots & a_{MN} \end{pmatrix}_{M \times N}$$

$$H = \{x \mid \forall\, x \in \text{human colour skin tone}, x \in \mathbb{Z}\} \qquad (4.1)$$

Using the selected threshold, an object (foot) image is extracted from the background image and yields a binary image, where the white area shows the entire foot and black is the foreground as shown in Figure 41(c).

If $f(x)$ is a function given as

$$f(x) = \begin{cases} 1 & Hmin \leq x \leq Hmax \\ 0 & otherwise \end{cases} \quad (4.2)$$

Where H_{min} and H_{max} is the minimum and maximum values of H respectively and serves as a lower and upper threshold bounds. Any pixel of HSV image A, shown as a matrix A, that lies within the human skin colour space H is considered the object (foot) pixels. Otherwise, the pixels belong to the background and set to black in colour.

The HSV image A under $f(x)$ is a binary image and can be represented in a matrix B with dimension $M \times N$ as given below,

$$B = \begin{pmatrix} b_{11} & b_{12} & b_{13} & \dots & b_{1N} \\ b_{21} & b_{22} & b_{23} & \ddots & b_{2N} \\ b_{(M-1)1} & b_{(M-1)2} & b_{(M-1)3} & \dots & b_{(M-1)N} \\ b_{M1} & b_{M2} & b_{M3} & \dots & b_{MN} \end{pmatrix}_{M \times N}$$

Each $\boldsymbol{b_{i,j}}$ has value either 0 or 1where i=0,1,2,...,M and j=0,1,2,...,N. The element of B with value 1 is the part of the plantar surface.

Let F is the set that contains all points belonging to plantar surface or foreground or more precisely F contains all white colour pixels.

$$F = \{ p(x, y) \mid \forall_{f(p)} = 1 \Lambda\, p(x,y) \in B \} \quad (4.3)$$

S is the set that contains foot stopper colour values in HSV space.

$$S = \{ x \mid \forall\ x \in \text{foot stopper colour}, x \in \mathbb{Z} \} \quad (4.4)$$

$$g(x) = \begin{cases} 1, & x \in S \\ 0, & otherwise \end{cases} \quad (4.5)$$

The HSV image A under $g(x)$ gives the exact foot stopper reference point FS(x',y').

In further stages, a contour is drawn around the plantar surface and is then bounded by a rectangle called the foot rectangle. The bounded rectangle encloses the entire foot, representing the foot dimension in terms of width and length as shown in Figure 41(d). The total foot length including toe can be identified by the total length of the rectangle bounding the entire foot. Before explaining the pressure points extraction, it is important to show the Cartesian plane used in the image processing. The origin of Cartesian plane in the image processing lies at top left corner of the image. Therefore, the x-axis increases from left to right as usual, while the y-axis grows from the top of the foot to bottom as indicated in Figure 42. Subsequently, the extreme points along the x-axis of the contours define the width of the rectangle.

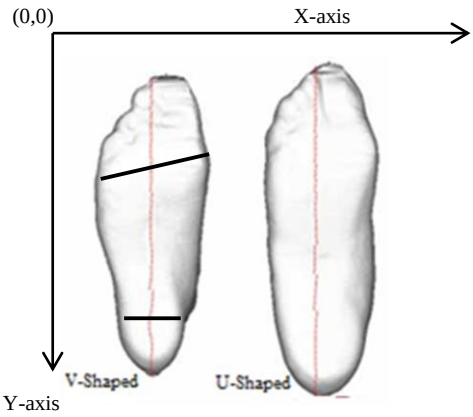

***Figure 42**: V- and U-shaped feet [77]*

The region of interest (ROI) for the toe pressure area is bounded by a sub-rectangle, shown by dashed line in Figure 41(d), created mathematically using FS point and top left corner point of the original foot rectangle area. The subsequent algorithm then considers only those contours' points at toe that lies within this sub-rectangle and is explained in the algorithm section.

A set T represents all the points in Toe pressure region

$$T = \{\, p(x,y) \mid \forall y \leq y' \wedge f(p) = 1 \,\} \qquad (4.6)$$

The work [87], is used to obtain the central point of the toe polygon of set T as follows

$$T_x = \frac{1}{6A_T} \sum_{i=0}^{N-1} (X_i + X_{i+1})(X_i Y_{i+1} - X_{i+1} Y_i) \qquad (4.7)$$

$$T_y = \frac{1}{6A_T} \sum_{i=0}^{N-1} (Y_i + Y_{i+1})(X_i Y_{i+1} - X_{i+1} Y_i) \qquad (4.8)$$

Where A_T is the area of the polygon comprises with the points of *T*. *N* is the cardinality of the set *T* or more specifically *N* is the number of vertices in the polygon. Subsequently the pressure point

of toe region is given as

$$T' (T_x , T_y) \qquad (4.9)$$

Following this the metatarsal area should be discovered in order to place pressure points correctly for this region. Pressure points at edges of the metatarsal area normally lie on the first and fifth metatarsophalngeal joint. Generally, the metatarsal area is the widest area of the plantar surface but this is not the case for all feet. There are currently two shapes of foot considered V and U and are classified [81].

The ratio of ball width (distance from first metatarsophalngeal joint to fifth metatarsal joint) and heel width, see Figure 42, changes from person to person. A large value of the ratio indicates a V-shape foot, while a small value indicates a U-shape foot [81]. The only difference between U and V shape foot is that the widest part of the foot, in a V-shaped foot, always lies in the metatarsal region. Subsequently in V-shape foot the extreme edges along x-axis are the metatarsophalngeal joint, first metatarsal joint at one side and fifth metatarsal joint on the other.

In the case of a U-shaped foot, the metatarsal area is first defined as the widest part of the plantar surface may not be the actual metatarsal region. To address these possible errors with such feet, the metatarsal pressure points are ascertained by using the process of foot anthropometry and the contour's extreme points along the x-axis and the FS. To aid algorithm speed, the same process takes place for both V and U shaped feet.

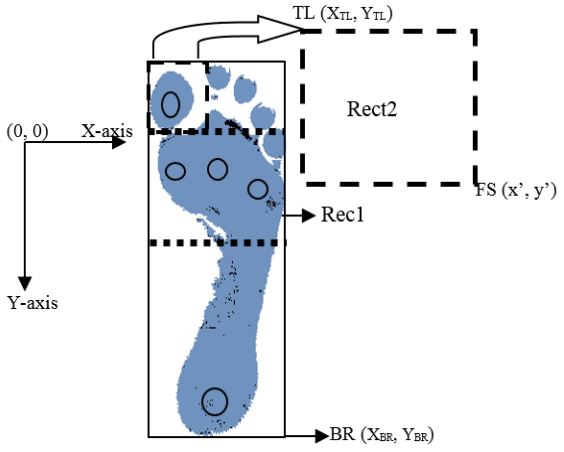

Figure 43: *Pressure points extracted by anthropometry of plantar surface*

As the metatarsal area lies in the forefoot area minus the toe, any extreme x-axis points lying above and below the forefoot area are excluded for metatarsal pressure point search. The metatarsal ROI algorithm produces an area bound by two dotted lines, as shown in Figure 43.

The lower boundary is the line dividing the entire plantar surface foot rectangle in two,

perpendicular to the y-axis, while the upper boundary is the line that the FS takes again perpendicular to that point on the y-axis across the plantar surface. The area extracted between the bounded lines is qualified for the metatarsal pressure points search.

For pressure points at metatarsal area a subset M of F is considered i.e. $M \subset F$

$$M = \{ p(x,y) \mid \forall y \geq y' \wedge y \leq \frac{max\ p(y)+min\ p(y)}{2} \wedge p(x,y) \in F\} \quad (4.10)$$

Where, max p(y) is the highest position in vertical direction (y-axis) in F. Similarly, the min p(y) is the lowest position vertically (y-axis) in the set F.

Once the metatarsal area is defined, the extreme points of contours are found by running the algorithm on the selected metatarsal area. The extreme points along the x-axis represent the first and fifth metatarsal pressure points that are associated with the metatarsal pressure points region.

The required pressure points at metatarsal are given as

$$M_1(M_{x1},M_{y1}) \mid M_{x1}=min\ (x) \wedge M1 \in M \quad (4.11)$$

$$M_2(M_{x2},M_{y2}) \mid M_{x2}= max\ (x) \wedge M2 \in M \quad (4.12)$$

$$M_3(M_{x3},M_{y3}) \mid \frac{M1(Mx1,My1) + M2(Mx2,My2)}{2} \wedge M_3 \in M \quad (4.13)$$

where M1, M2 and M3 are left, right, and middle metatarsal pressure points.

The pressure point at heel is a point in Set F with largest y coordinate

$$H(x,y) \mid y=max\ H(y) \in F \quad (4.14)$$

Hence 4.9, 4.10, 4.11, 4.12, 4.13 and 4.14 are the extracted pressure points i.e.

$$T'(T_x , T_y),\ M_1(M_{x1},M_{y1}) ,\ M_2(M_{x2},M_{y2}) ,\ M_3(M_{x3},M_{y3}),\ H(H_x, H_y)$$

The algorithm output depends on the following pre-process conditions given below:

1. The foot must be placed straight on the scanner using the FS.
2. No other part of the skin, except the plantar surface should be exposed to the scanner.

3. Though the background noise in the image is filtered, controlling the background noise will minimize the possibility of failure, as will be shown.

The following algorithm shows the step-by-step procedure to find the required pressure points from the ROI's previously described. Those specific regions namely toe (Hallux), metatarsal heads and heel (Calcaneum).

1. Obtain the dimension of foot in length and width using the bounded rectangle Rec1.
2. Obtain the Region Of Interest (ROI) for the toe by drawing a rectangle Rec2 mathematically using $FS(x', y')$ and the rectangle top left point $TL(X_{TL}, Y_{TL})$ as shown in Figure 43.
3. Draw the polygon from the toe contour points bounded by Rec2.
4. Obtain the central point of the toe contour using a trapezoidal centroid.
5. The metatarsal region is ascertained using the foot anthropometry. Once the ROI for the metatarsal is framed, a leftmost point along the x-axis is obtained as a left metatarsal point. Similarly, the right most point at metatarsal region is assured by discovering the point with the largest x-coordinate of the contour.
6. Heel pressure point can be identified by finding the point with the largest y-coordinate in contours.

4.1 Further Progress: Toe Groove

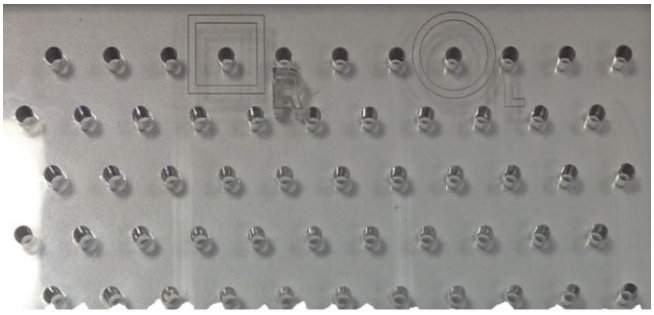

Figure 44: *Top and left toe grooves on perforated sheet*

Although the method previously described is very useful, however the use of a foot stopper (FS) could be problematic for patients with severe foot problems. In this chapter a foot groove on the perforated sheet is considered in order to alleviate these issues. A patient's foot is scanned optically and the subsequent image processing and the use of fixed foot groove reference reliably identify the plantar surface sensory neuropathy pressure points on a given patient's foot.

Subsequently, these coordinates are relayed to an automated mechanical probe driven by a microcontroller where it randomly applies the accepted 98mN (10g) of force to those pressure points.

Toe groove, left and right feet, are introduced on the perforated sheet, as shown in Figure 44, to guide foot placement. Both grooves contain a hole in the centre, it guides the patient to place their toe right over the groove. As both holes have fixed position on perforated sheet, these holes serve as a reference point for anthropometric calculation similar to the Foot stopper in previous algorithm.

Once the foot is bounded by a rectangle Rec1, another rectangle Rec2 is drawn with the help of two points $TL(X_{TL}, Y_{TL})$ an $G'(X'_G, Y'_G)$ as shown in Figure 45 in dotted line.

Here $TL(X_{TL}, Y_{TL})$ is the top left point of Rec1 and $G'(X'_G, Y'_G)$ is the bottom right point of Rec2.

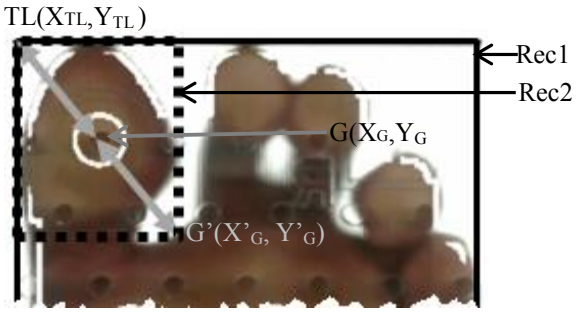

Figure 45: *Test pressure point extraction under toe*

$$X'_G = 2 * (X_G - X_{TL})$$

$$Y'_G = 2 * (Y_G - Y_{TL})$$

where $G(X_G, Y_G)$ are the coordinates of the hole inside the groove.

In the next phase metatarsal area is outlined by the boundary lines, as shown in Figure 43. The lower boundary is the line dividing the entire plantar surface foot rectangle in two, perpendicular to the y-axis, while the upper boundary is the line that passes through the point $G'(X'_G, Y'_G)$ and perpendicular to that point on the y-axis across the plantar surface. The area extracted between the bounded lines is qualified for the metatarsal pressure points search.

The heel areas are approximated and in the last phase by considering the lowest y-coordinate of the contour. The approximated areas are processed to localise the pressure point inside the specific pressure regions. Paddings are added to avoid selection of pressure point at edge of the plantar surface in a specific pressure region.

The plantar surface bounded rectangle is internally divided vertically by 6 columns as shown in Figure 46(a). Each vertically segmented space is correlated with the width of the foot. The first

and last vertical spaces acts as paddings. The extreme pressure points at both ends of metatarsal must be selected in between these pads.

The plantar surface bounded rectangle is internally divided horizontally by 25 segments and shown in Figure 46(b). Each segment space is correlated with the length of the foot. The heel pressure point must be above the last two segment space so that it lies well inside the heel.

(a) *(b)*

Figure 46: *(a)Vertical segmented into six columns; (b) Internal division into 25 columns*

To test the systems accuracy, a qualified podiatrist with over 15 years' experience collaborated to compare the automated and manual SWM pressure detection methods. Foot images from all 70 subjects were provided and the podiatrist independently marked what she identified as the five pressure points on each foot. She then drew a "circle of acceptance" with a diameter of 1 cm bounding those points and each image was stored separately from the automated findings. A success was considered when the output of the machine identified the same area (anywhere inside the podiatrists drawn circle), a failure if not.

Age Group	Quantity
20-25	5
25-30	11
30-35	16
35-40	25
40-45	8
50-70	5

Table 1: Database age group

Ethnicity	Quantity
Western European	15
Eastern European	11
African	15
Asian	20
Chinese	9
Total	70

Table 2: Database ethnicities

The time efficiency of the system against the manual method was also evaluated. This evaluation included testing, manual reporting and result storage. The proposed automated system takes 47

seconds to a single foot test. It includes handshaking of personal computer (PC) with scanner (4 sec), picturise the foot (36 sec), extract 5 test points displaying the test results visually (5 sec) and sending them to health care provider via internet i.e. email. (2 sec). The manual SWME process takes in total 180 second per foot between viewing a foot, making a pressure-point decision, final data handling and storage. This does not include SWM application in either case. This clearly shows the time and information advantages of such an automated approach.

A group of healthy subjects (44 male and 26 female participants with a mean age of 32.85 (±7.4) years) were selected. The database consists of 70 images of different ethnicities, age groups, and gender, as given in Table I and II. In the first phase, the algorithm initially showed 96% agreement with the pressure points chosen by the podiatrist. Issues causing the4% failure rates were identified and are presented. In the first phase, the algorithm initially showed 96% agreement with the pressure points chosen by the podiatrist. Issues causing the 4% failure rates were identified and are presented. The primary failure occurs when the image processing algorithm mistakenly detects a portion of background as a part of the object (foot), e.g. if a skin tone exists in the background, as shown in the Figure 47(a).

(a) (b) (c)

Figure 47*: Spots in the background similar to skin tone: (a): Input image; (b) Contours of detected plantar surface and false positive detected object in the background; (c) Superimposed of image (a) and image (b).*

The actual image and the detected edges are superimposed to help the reader visualize the unwanted background as part of the foreground (foot) as shown in Figure 47(c).

A controlled background mitigates such false positive detection.

This controlled background was achieved by the use of a short range optical flat-bed scanner and reduced external lighting conditions. Failure may also occur if skin, other than foot plantar surface, is exposed to the scanner, as shown in Figure 48.

(a) (b) (c)

Figure 48: *Unwanted skin detection proximal to the plantar surface: (a) Input image; (b) Binary image of detected plantar and skin other than plantar surface; (c) Incorrectly detected pressure points*

The algorithm extenuates minor patches in the background similar to plantar skin colour by Gaussian blur filtering and only considers the single large patch of plantar skin in the image. This constraint is avoided by ensuring foot placement is performed in a straight and upright manner. This is now ensured by a voice activated system explaining to the user how to place their foot correctly on the scanner and a 5 second sub-scan test performed.

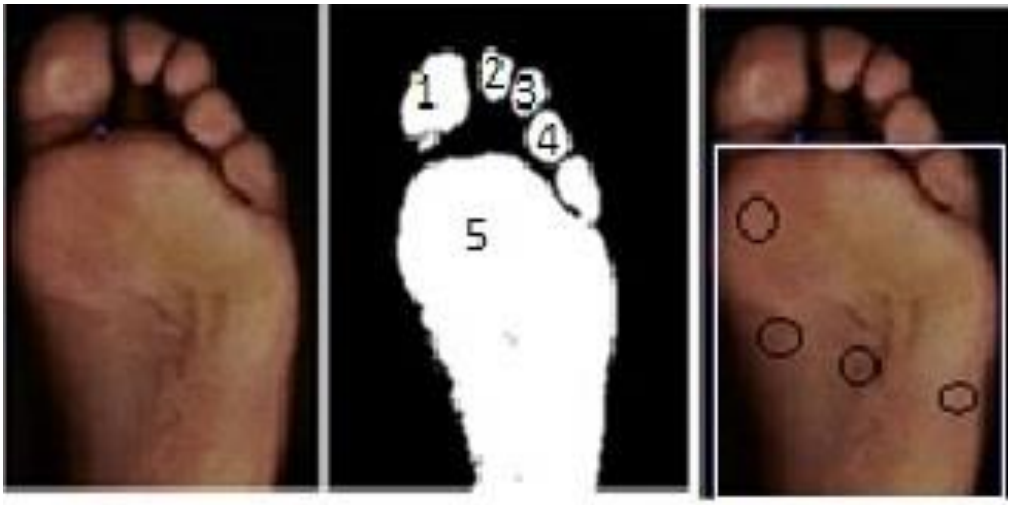

Figure 49*: Object's (foot) patches are numbered in binary image*

A final cause of failure is the object, the foot in this case, appearing as separated patches in the binary image, rooted from poor light. Consider Figure 49, where the toe and other foot digits, numbered by 1, 2, 3 and 4, appear separated from the rest of the foot image i.e. patch 5. The 5th patch is the largest patch and comprises a major portion of the foot, while the rest of the patches are the separated foot digits. The rectangle only bounds the largest patch that represents the foot.

The combination of a dilation followed by erosion morphological operations in image processing, known as 'closing', can be used to connect objects in a binary image that are close to each other, or to fill the gaps in the object by using a structural element [96]. The operation is controlled by a structural element which is used to "smooth" the regional boundaries without significant or obvious changes to the area [99]. If '*I*' is a binary image and *E* is a structural element, then

$$I \bullet E = (I \oplus E) \ominus E \qquad (4.15)$$

Where $\oplus$ and $\ominus$ denote dilation and erosion respectively. Post-closing operation reduced the number of patches without deteriorating the actual size of the foot as shown in Figure 50.

Figure 50: *After dilation with visible contour boundary*

The proposed solutions above were implemented in a second test phase with the same participants and procedures as before and a 100% success rate was achieved.

Manual and automated testing time comparisons were also evaluated. This evaluation included

pressure point detection, manual reporting (original SWME) and result storage. The automated system proposed takes a total 47s per foot including data storage and email transmission.

The manual SWME process takes in total 180s per foot between viewing a foot, making a pressure point decision, final data handling and storage. This does not include SWM application in either case. This clearly shows the time and information advantages of such an automated approach.

Future research will focus on (a) adding the developed algorithm directly to the physical system architecture and (b) more complex image processing mechanisms to substitute the foot stopper with an embedded left and right large toe groove in the perforated sheet. In parallel with the above, lesion recognition on the plantar surface will be performed to avoid subsequent probe application on pressure points where they may overlap a lesion. The authors will consider 3G system options to account for broadband and wireless fidelity (Wi-Fi) restrictions in developing countries, making use of mobile phone and tablet systems at practitioner sites.

4.1.2 Foot Sectorisation

The introduction of foot grove method in perforated sheet mitigate the issues related to foot stopper (FS) but at the same time foot placement is dependent on the toe groove. It is sometimes difficult to locate the toe groove easily. Another robust change in algorithm has been recommended, the foot sectorisation. The proposed algorithm is required on place the foot anywhere on the perforated sheet but in a straight and upright manner. A patient's foot is scanned optically and the subsequent image processing and grid information algorithms presented reliably identify the plantar surface sensory neuropathy pressure points on a given patient's foot. Subsequently, these coordinates are relayed to an automated mechanical probe driven by a microcontroller where it randomly applies the accepted 98mN (10g) of force to those pressure points. The current approach is more generic and can accommodate flat and non-flat feet as well as different ethnicities. Grid sectorisation enables faster pressure point recognition.

4.1.2.1 Methodology

As before the foot image is scanned using a flatbed scanning technique and the obtained image is

shown in Figure 51(a). The in-house designed image processing code extracts the object (foot) from the background (image) and draws a border around the detected foot as shown in Figure 51(b). The obtained foot image (object) is then sub-divided into a fixed dimensions of grid as shown in Figure 51(c). The space, cell size of the grid, amongst grid rows and columns is correlated to the size of the foot being scanned. Following the grid incorporation, two computational phases are then performed.

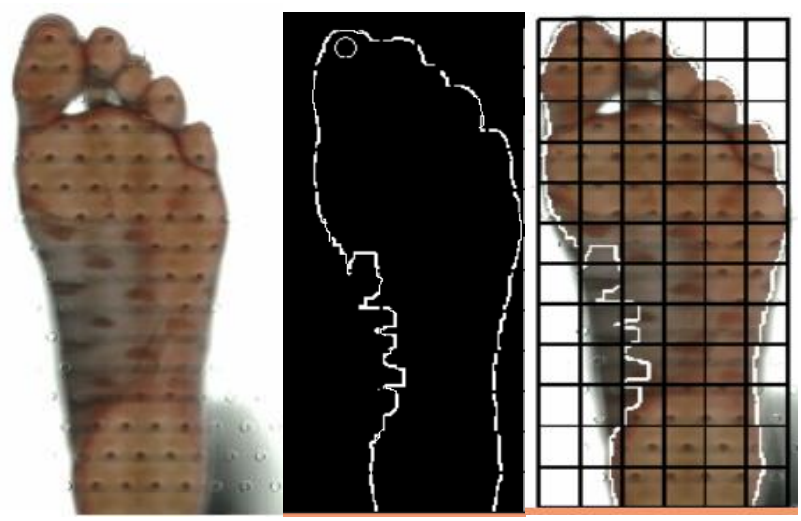

(a) (b) (c)

Figure 51: *Processing the input image: (a) Input image; (b) External boundary; (c) Foot in grid.*

In phase 1, the foot image is sub-sectioned into approximated pressure regions of interest using the grid information. The sub-sectioned regions are namely the toe, metatarsal, and heel regions.

For a better understanding, an analogy of matrix element position and grid cell position is made, hence the entire grid is represented by a matrix '*G*' as given below.

$$G = [g_{i,j}]_{M \times N} \qquad (4.16)$$

here, 'g' represents the sub-element, (grid cell) within the grid *G*, *i* and *j* are cell position within the rows M and columns N respectively, where $1 \leq i \leq M$ and $1 \leq j \leq N$ and M=12 and N=6. For example, the first top left cell in the grid is represented by $g_{1,1}$ and the 2nd cell in first row is represented by $g_{1,2}$ and so on.

The region of interest (ROI) for the toe pressure area always lies in a sub-rectangle or sub-matrix '*T*' i.e. $T \subseteq G$;

$$T = [t_{i,j}]_{2 \times 2} \qquad (4.17)$$

where $1 \leq i \leq 2$ and $1 \leq j \leq 2$, where '*t*' represents one cell inside the *T*, subset of *G*, as shown in Figure 52. The element of matrix, grid, *T* are $(t_{1,1}, t_{1,2}, t_{2,1}, t_{2,2})$.

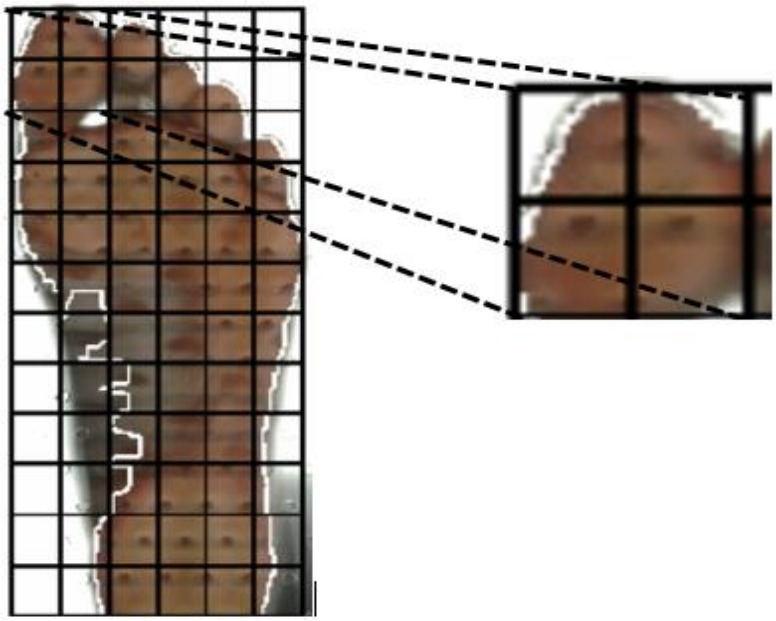

***Figure 52**: Extraction of toe area using grid*

The metatarsal area is then computed so as to correctly identify the pressure points for this region. Using the same matrices analogy, the metatarsal area lies at fore foot minus toe and it always resides in grid area, represented by a matrix 'M_e' as follows:

$$M_e = [m_{i,j}]_{4\times 6} \qquad (4.18)$$

where $3 \leq i \leq 6$ and $1 \leq j \leq 6$ and $Me \subseteq G$ and 'm' represent one cell inside the subset 'M_e' with relative position of i_{th} row and j_{th} column in G as shown in Figure 53(a).

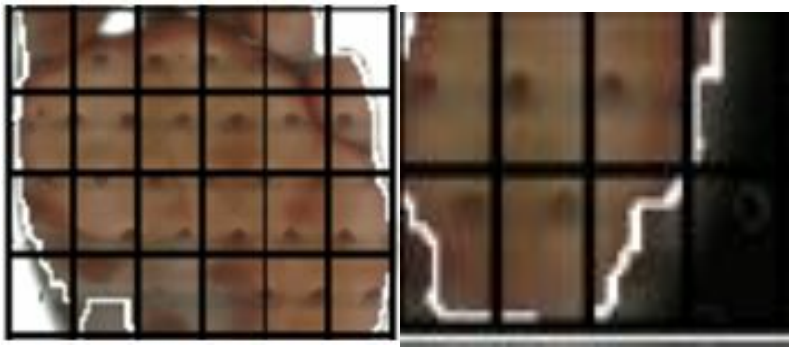

(a) *(b)*

***Figure 53:** (a) Sectorisation of metatarsal area and (b) heel area by dissecting grid*

To avoid the mechanical probe hitting the outer edge of a patient's foot, the heel area pressure point is defined by subtracting one grid row from the max y-coordinate of the external boundary contour. The heel area always lies in the grid area, represented by a matrix, grid '*H*' as follows:

$$H = [h_{i,j}]_{2\times 4} \qquad (4.19)$$

where $11 \leq i \leq 12$ and $2 \leq j \leq 5$ and $H \subseteq G$ and '*h*' represent one cell inside the subset *H* with relative position of i_{th} row and j_{th} column in *G* as shown in Figure 53(b).

The grid formation is used in phase 1 to dissect the foot image further and to produce areas that represent the plantar surface pressure points in the regions found above. Using the grid in this phase enables a faster processing time as it promotes a more accurate sub-detection of the pressure region via the grid and excludes regions outside the area of interest.

The subsequent algorithm then considers only those contour points of the toe that lie within this sub-rectangle *T*. A central point of the toe polygon is obtained by applying trapezoidal centroid.

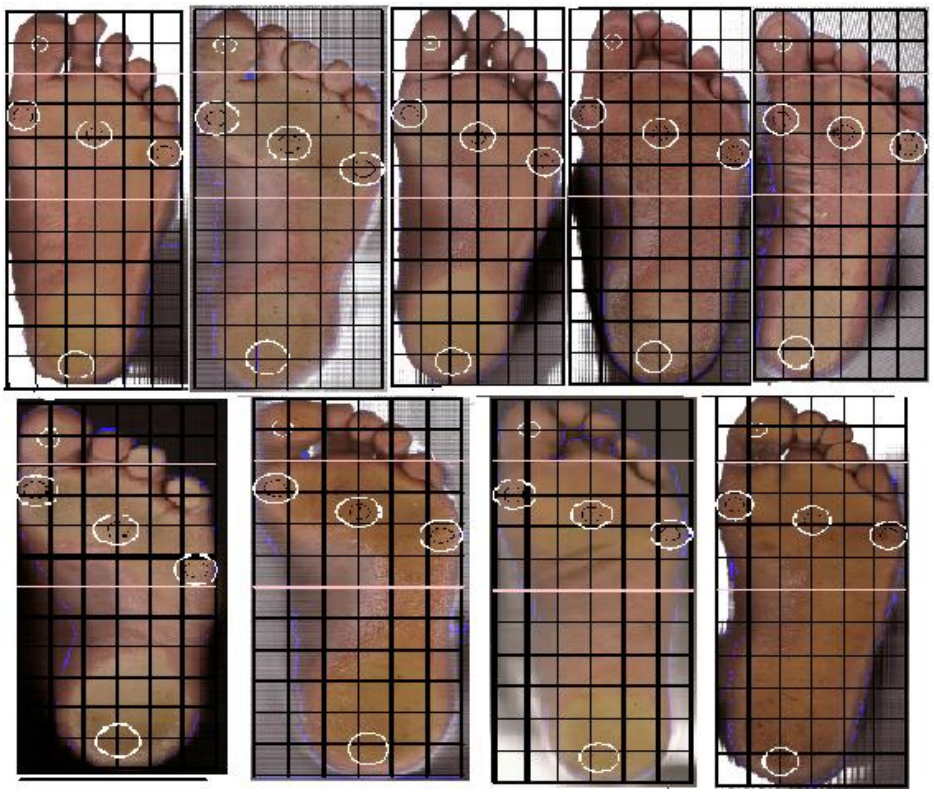

Figure 54: *Foot images with a grid of 12 rows and six columns and extracted pressure points*

The algorithm is then applied on the sub rectangle *M* and three pressure points, the first metatarsophalangeal joint and a central point between these two points are found, using the extreme contour points on the x-axis.

The pressure point at the heel is extracted by subtracting one grid step from the y-coordinate of the contour's point that has the largest y-coordinates. Results for 9 participants are shown in Figure 54. Participant details are presented in Table's 1 and 2.

Investigations to optimise the grid size were performed and it was established that that the performance of the grid increased and peaked when it had dimensions of 12 rows and 6 columns, with further division of the grid deteriorating the performance. This is to say that the grid is optimized as above, but the cell size of the grid varies with foot size. The grid information successfully classifies the pressure regions i.e. the accepted toe, metatarsal and heel areas.

Subsequently, the mechanical phase takes place. The locations of the extracted pressure points are then translated in terms of rows and columns position which are then aligned to a hole in the perforated sheet closest to the chosen pressure point. This information is then relayed to an off the shelf microcontroller board via serial communication.

A probe assembly was fabricated in-house using precision components and a commercial amplifier and calibrated to apply exactly 98mN ±1%. This assembly is driven by stepper motor controlled rails in both the X and Y-axes. Once the microcontroller has received the correct coordinates from the algorithms as described it directs the probe assembly accordingly, a further Z-axis stepper motor is then used to drive the probe onto the plantar surface to apply exactly 98mN to each site in turn. If the patient feels the probe, they record their response by pressing a handheld button which is wired into the microcontroller. The response latency is recorded by the microcontroller and a two second window is permitted for a positive response to be recorded. Furthermore, a random delay is introduced before the probe is activated to mitigate false positives or "guessing" by the patient. Once all five test sites have been examined the microcontroller returns the probe to its home location and transfers the results of the tests to the host PC.

4.1.2.2 System Flow Chart

The overall sequence of the system test execution is shown in Figure 55. Here PC stands for host Computer and MC stands for microcontroller.

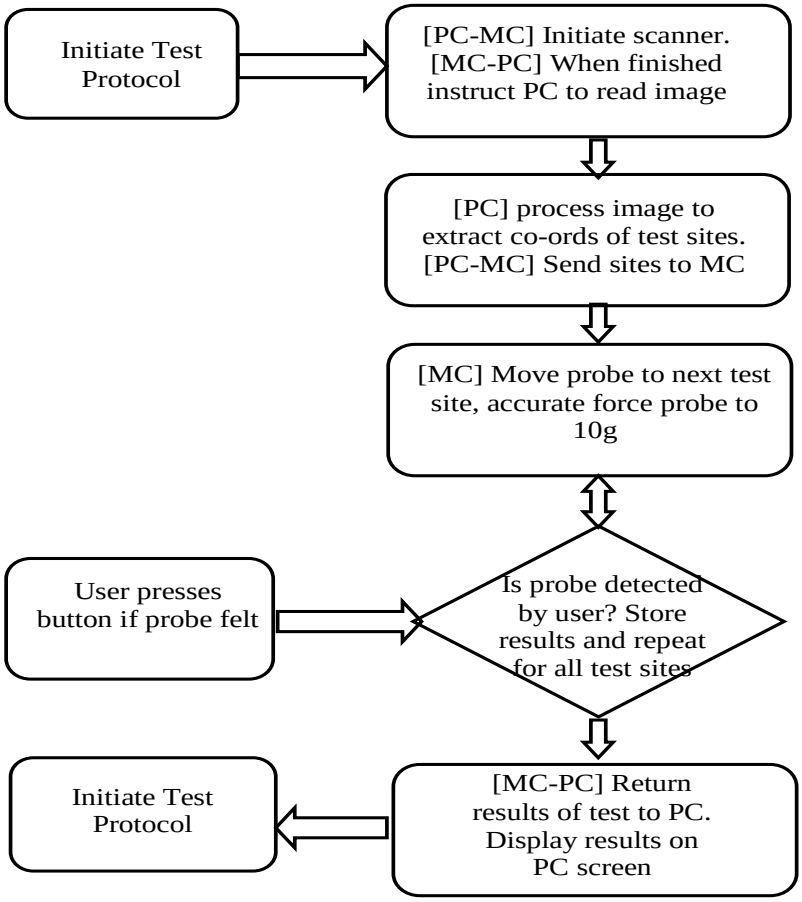

Figure 55: *System flow chart*

4.2 CONCLUSION

An improved method is introduced to make the automated pressure area selection on plantar surface independent of ethnicities and to account for non-standard foot pressures. A fixed small and soft stud is used to assist the supervisory development of the programme, introduced to the underside of the perforated sheet. The foot stopper, stud, improved the algorithm but at the same time the use of a (FS) could be problematic for patients with severe foot problems. Another improvement made by introducing toe groove on the perforated sheet in Lieu of FS in order to alleviate issues associated with FS. The proposed method performs a thresholding process and bounds the foot image in a rectangle followed by contours. Plantar pressure points are then obtained using a combined approach of optical imaging over the HSV three-dimensional colour space and plantar anthropometry. The algorithm was successfully applied on 70 participants with a 100% success result, regardless of the patient's race, age or gender. The introduction of foot grove method in perforated sheet mitigate the issues related to foot stopper (FS) but at the same time foot placement is dependent on the toe groove. It is sometimes difficult to locate the toe groove easily. Another robust change in algorithm has been recommended, the foot sectorisation. The proposed algorithm is required on place the foot anywhere on the perforated sheet but in a straight and upright manner. A patient's foot is scanned optically and the subsequent image processing and grid information algorithms presented reliably identify the plantar surface sensory neuropathy pressure points on a given patient's foot. The current approach is more generic and can accommodate flat and non-flat feet as well as different ethnicities. Further research focuses on lesion recognition on the plantar surface to avoid the probe application on pressure points where they overlap a lesion.

CHAPTER 5. Plantar Surface Lesion Detection Using Layered Approach of LBP and SVM

When a photographic image of the plantar surface is obtained, the PerSeNT image processing program extracts five pressure points to be tested by a mechanically driven probe. These five pressure points match those chosen by the SWME method. There may be some areas where probe shouldn't be applied e.g. cuts or bruises, thus the algorithm must be smart enough to discriminate normal and abnormal skin or lesions and avoid the probe application on pressure points that are overlapped with lesions.

A breach in the skin is known as lesion and the trained podiatrist obviously through appearance and sight avoid applying the probe to it. The PerSeNT should comply with the same rule, but in an automated manner. If test points on the plantar surface and lesion overlap the area must be avoided and an adjacent non-overlapped suitable pressure test point needs to be selected.

Given such a system obvious care must be taken to recognise areas where the probe must not be applied such as on lesions, blisters and open wounds. Research hitherto focused on lesion detection on the plantar surface to avoid the probe application on pressure points where they overlap the lesion. Automatic lesion detection is a challenging issue because the presence of inconsistencies in lesion appearance. Wounds have great variation in shape, low contrast between lesion and the surrounding skin, irregular or fuzzy boundaries, variegated colouring inside the lesion, and artefacts such as skin line, hairs, black frames and blood vessels [45, 46]. Further complexities include slough and coagulated blood in and around the lesion while due to the influence of some dressing materials, the wound colour as a whole may be shifted [46]. Several algorithms have been developed and deployed to deal with the challenge but these algorithms are lesion specific oriented. These are generally classified as a thresholding, edge based detection or region based methods [92]. Thresholding performance is high when there is a good contrast between skin and lesion but degrades if the two are overlap [45, 101]. Edge based detection performs poorly if boundaries are not well defined and region based detection has difficulties when the lesion or skin region are textured or have different colours present which leads to over segmentation [46].

Texture information is a key and proficient tool to estimate the structure, orientation, roughness, smoothness, or regularity of various regions in a set of images to distinguish between discriminate objects [102]. Yet texture analysis is considered as one of the most challenges in computer vision and image analysis. Generally, Image texture is defined as a certain pattern repeated in a local area of an image [102].

Texture analysis is usually performed in two steps

(i) Texture feature extraction

(ii) Texture identification and classification.

Commonly used texture extraction methods include statistical, model-based, and filtering-based methods, while classification and identification methods for texture include neural networks, decision trees, and support vector machines [102].

Some of the algorithms based on colour space segmentation and histogram equalisation use special equipment, Nevoscope, and specific lesion (melanoma) [103]. Some have used edge-based segmentation [104], again here detection is confined to a specific lesion, malignant melanoma, of dermoscopy images. Regional-based wound detection based on the colour and texture or combination of both was remained the subject of many algorithms, including Local Binary Pattern (LBP), Gray Level Co-Occurrence Matrix (GLCM) [105, 106]. There are few robust algorithms in the machine learning domain for classifications e.g. neural network, support vector machine [107, 108].

Different statistical and mathematical tools are available in image processing to obtain textural information of a specific object in an image e.g. histogram, Scale-Invariant Feature Transform (SIFT), Speeded Up Robust Features (SURF), Colour intensity distribution of an object within an image using different colour space can also facilitate the recognition of a particular object. Combining machine learning and textural recognition algorithms can be used to efficiently discriminate normal and abnormal skin based on the appearance using image processing –A non-invasive and non-aversive approach.

The scenario presented in this thesis is different from others in that, the intended algorithm should be smart enough to detect all types of lesions related to the plantar surface. The main objective is to discriminate the location of plantar surface whether it is normal or abnormal skin. Two approaches, LBP and SVM are used in a layered fashion to detect lesions on the plantar surface. LBP detects the lesion on plantar surface, once it is trained. The detected area by LBP is then passed through SVM that has seven dimensions or features space built by the statistical data of colour intensities of constituent channels of BGR and HSV colour space and histogram of the lesion image. The area is qualified as a lesion area if SVM identifies it as a lesion based on its training.

5.1 Local Binary Pattern (LBP)

LBP is one of the most popular discriminating tools based on the texture. LBP is computationally extremely simple and invariant to monotonic greyscale changes [102]. The basic idea behind LBP is the extraction of the pattern by thresholding the neighbouring pixels of 3 * 3 block by its central pixel and then obtaining an LBP code for the central pixel [108]. A histogram is drawn using LBP code to show the distribution of the pattern and used in pattern comparison as shown in Figure 56 and 57.

The original LBP was invariant to image rotation, and many extensions have been made to make it scale and rotation invariant. To make the LBP discriminate for different texture sizes, the block is considered as a circle where neighbouring pixels are evenly spaced on a circle. The notation used for such kind of LBP is given as (P, R) and the LBP code is given by the expression below [109].

$$LBP_{(P,R)} = \sum_{p=0}^{p-1} s(g_p - g_c)\, 2^p \qquad (5.1)$$

Here P is the total number of neighbours of the central pixel of the circle, R is the radius of the circle, g_c and g_p are the grey values of the central pixel, and particular neighbour pixels respectively.

$$S(x) = \begin{cases} 1, & x \geq 0 \\ 0, & x \leq 0 \end{cases} \qquad (5.2)$$

Where *S(x)* is the thresholding function. Based on *P* and *R*, different size of LBP can be used to achieve scale invariant LBP texture descriptor as shown in Figure 58.

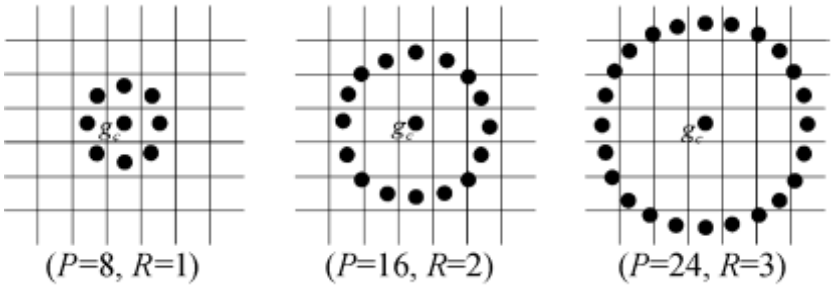

Figure 58: *Differently sized LBP descriptors based on P and R values*

For rotation invariant LBP the original approach is used where LBP bit code is circularly rotating to its minimum LBP code value. For example, if the LBP code extracted as

10000111= 143, 11000011= 195, 11100001= 225, 11110000=240, 01111000=120, 00111100=60, 00011110=30, 00001111=15

In the above example the minimum value is 15 so the LBP code 00001111 will be used as a LBP descriptor for that particular central pixels.

5.2 Support Vector Machine (SVM)

Support Vector Machine (SVM) is one of the widely used supervised learning algorithm. It has a main method used for prediction based on a set of training data. SVM is trained under supervised learning to discriminate each extracted test point's surrounding area as absent and present of lesion. Currently the SVM is trained with 11 different lesions, further investigation is underway.

Let *vectors x1,x2,….,xn* Є Rn are patterns to be classified and scalar *y1, y2, …, yn* Є{-1, +1} are labels. Then the pair {(*xi, yi*) | i=1, 2, … , n} is the set of n training examples, where each training pattern is paired with one of y value. A hyperplane is required to divide same set of pattern or examples on one side and other are on other side. SVM finds a decision boundary that has maximum margin between two classes using linear function [110, 111, and 112] as shown in Figure 59(a)

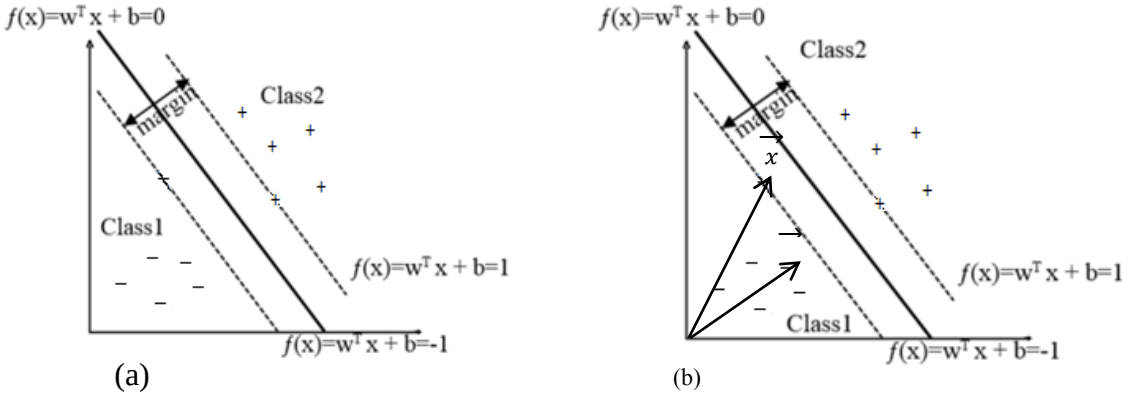

Figure 59: *(a) Hyperplane separating two classes with maximum margin using the SVM; (b) Vector w normal to central line and vector x points to sample x.*

Let is a vector and perpendicular to the central line and there are some unknown '*x*', pointed by a vector as shown in Figure 59 (b). To find whether *x* is on positive side or negative side. The projection of *X* on *W* will determine its class i.e.

$\bar{w} . \bar{x} \geq c$

where c is some constant. Let $c=-b$

$\bar{w} . \bar{x} + b \geq 0$ *(5.3)*

If (5.3) is true then it is a positive sample, this is called "Decision Rule". Let

Let $\bar{w} . \bar{x}_+ + b \geq +1$ likewise $\bar{w} . \bar{x}_- + b \leq -1$

For a mathematical convenient a single equation is substituted keeping the above unaffected.

Take y_i such that y_i = +1 for positive samples and y_i= -1 for negative samples,

Where $i=1, 2, \ldots, n$

Now the above equation can be written as

$y_i(\bar{w} . \bar{x} + b) - 1 \geq 0$ for all $i=1, 2 \ldots, n$ *(5.4)*

For a maximum margin or wider space between the two classes $M=2 / \|\bar{w}\|$ must be maximum.

The only factor that contributes in M to maximize it, is $\|\bar{w}\|$. For mathematical convenient $2 / \|\bar{w}$

|| is replaced by $\|\bar{w}\|^2/2$.

Thus for maximum *M*, $\|\bar{w}\|^2/2$ is needed to be minimum subject to (4).

Now the decision rule

$f : \bar{x} - y$ is then $f(x) = \text{sgn}(\sum_{i=1}^{n} y_i \bar{w} . \bar{x} + b)$ (5.5)

To find the extremum of a function under the given constraint, Lagrange's multiplier was used.

$L=\frac{1}{2}\|\bar{w}\|^2 - \sum_{i=1}^{n} \alpha_i[y_i(\bar{w} . \bar{x} + b) - 1]$

By taking partial derivative with respect to "w" and b

$\bar{w} = \sum_{i=1}^{n} \alpha_i y_i . \bar{x}_i$

$\sum_{i=1}^{n} \alpha_i y_i = 0.$

Replacing them back into L following is obtained

$L = \sum_{i=1}^{n} \alpha_i - \frac{1}{2}\sum_{i,j=1}^{n} \alpha_i\alpha_j y_i y_j(\bar{x}_i . \bar{x}_j)$ (5.6)

Subject to $\sum_{i=1}^{n} \alpha_i y_i = 0$, $0 \leq \alpha_i \leq \frac{c}{n}$, for i = 1,2, …, n. The decision rule, then becomes

$f(x) = \text{sgn}(\sum_{i=1}^{n} y_i \alpha_i \bar{x}_i . \bar{x} + b)$

Practically, data input space becomes nonlinear and difficult to make it linearly separable. SVM needs a kernel function to transform an input data set into higher dimensions and the Lagrange's multipliers associated with minimum $\|\bar{w}\|^2/2$takes the following form.

$L = \sum_{i=1}^{n} \alpha_i - \frac{1}{2}\sum_{i,j=1}^{n} \alpha_i\alpha_j y_i y_j(\Phi(\bar{x}_i) . \Phi(\bar{x}_j))$ (5.7)

Subject to $\sum_{i=1}^{n} \alpha_i y_i = 0$, $0 \leq \alpha_i \leq \frac{c}{n}$, for i = 1,2, …, n.

The decision rule is

$f(x) = \text{sgn}(\sum_{i=1}^{n} y_i \alpha_i \Phi(\bar{x}_i). \Phi(\bar{x}_j) + b)$

Mercer's theorem indicates that there exists a mapping Φ such that

$K(\bar{x}_i, \bar{x}_j) = \Phi(\bar{x}_i).\ \Phi(\bar{x}_j)$, the decision function then becomes

$$f(x) = \mathrm{sgn}\left(\sum_{i=1}^{n} y_i \alpha_i K(\bar{x}_i, \bar{x}_j) + b\right) \quad (5.8)$$

In the case presented here in this thesis, the radial basis function (RBF) kernel is selected to be the kernel of the SVM.

5.3 Methodology

Firstly, obtained the statistical data (mean ± SD) of constituent colors (channels) intensities of the stored lesion images and plantar pressure regions from a different ethnic groups in two most commonly used color spaces in image processing BGR and HSV and obtained their hue histogram H_h, the hue distribution.

If f(x, y) is the lesion image then features set F is obtained as

$$F = [B_{avg,} G_{avg}, R_{avg}, H_{avg}, S_{avg}, V_{avg}, H_h]$$

All the sample images are then labelled either +1 or -1 to discriminate normal and abnormal plantar surface skin. The SVM is trained by the stored sample lesion and non-lesion images, based on the above mentioned features space *F*. Once the SVM has learned or been trained with above features or parameters, the SVM is applied on input image that classifies it into lesion and non-lesion areas based on the training.

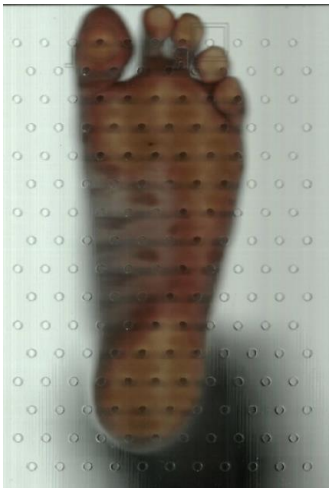

***Figure 60**: Scanned input image with perforated sheet*

The surrounding area of the extracted test point is examined by the lesion detection code in the manner presented below. The input image as show in Figure 60 is divided into equal sized patches such that each patch contains a hole roughly at its centre. The holes on the perforated sheet are laid out in 11 columns and 16 rows i.e. total number of holes is 176. Consequently, the input image is divided into 176 patches

The patches can have any one of the following patterns as shown in the Figure 61.

i. Blank Patch

The patch of the input image residing outside the plantar surface, as shown in Figure 61(a).

ii. Foot Edge Patch

The patch that lies at the edge of the plantar surface in the image as shown in Figure 60(b).

iii. Foot Pressure Area Patch

The patch of the input image that lies inside the pressure area of the plantar surface and shown in Figure 61(c).

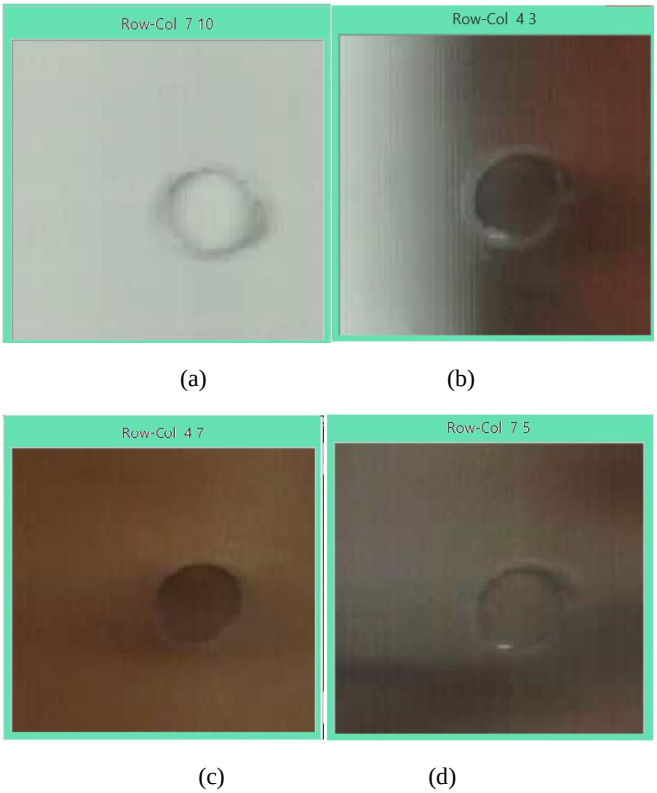

***Figure 61**: Perforated sheet's patch patterns: (a) Blank hole; (b) Edge; (c) Plantar pressure area; (d) Plantar non-pressure area*

iv. Foot Non-Pressure Area Patch

It is the patch that lies in the plantar surface non pressure area e.g. middle arch and shown in the Figure 61(d).

The local binary pattern is trained with these patches from a wide range plantar surface using different ethnicities; the local binary pattern information is transformed into LBP histogram and stored for future use.

When the algorithm extracts the pressure points, the corresponding patch is sent to LBP section to compute the LBP pattern, an example is shown in Figure 62(b). In the LBP section, LBP code histogram for the patch is obtained as shown in Figure 62(c). In the next step the LBP histogram of input image patch is compared with the stored LBP histogram. The Bhatta Charia histogram comparison is used to discriminate normal and abnormal patch. The Bhatta Charia histogram comparison gives comparison results via value in the range from 0 to 1.

For identical patterns the Bhatta Charia histogram comparison results in 0 and 1 for opposite. In this research, the Bhatta Charia histogram comparison value that falls in the range of 0 to 0.05 is considered identical normal plantar pressure area pattern and outside the above mentioned range is considered as an abnormal skin patch.

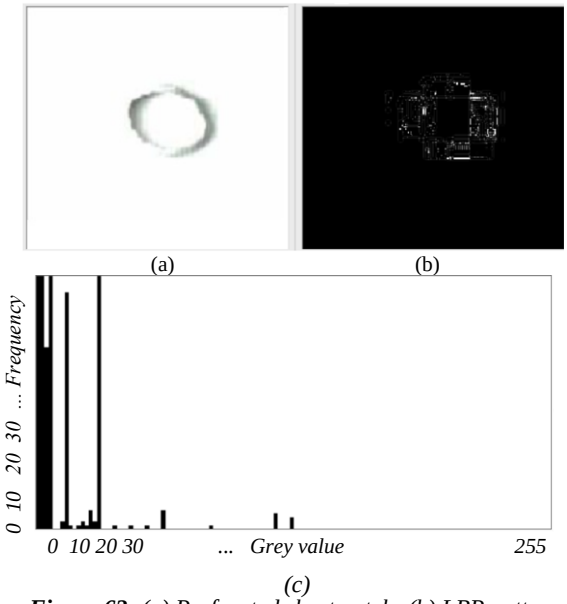

***Figure 62**: (a) Perforated sheet patch; (b) LBP pattern of the patch Figure 57(a); (c) LBP code histogram*

The range 0 to 0.05 is taken to accommodate any minor changes in normal plantar pressure area patterns. If the pattern matches the stored patches, it is classified as a normal patch. In the case of an abnormal patch, the patch is sent to SVM for further examination, where it is classified as a lesion or non-lesion patch. In the SVM layer, the patch is further divided into segments or windows. If the patch is found as a non-lesion or in other words 'normal skin', by the SVM layer, the extracted pressure points are added to the pressure point stream to be sent to microcontroller for the subsequent probe application. If the SVM results in a lesion patch, the corresponding hole is encircled in red as shown in Figure 63 and the next best hole is selected. This process is repeated until a healthy pressure skin area is found in the respective pressure region.

For example, using the extracted test point $P(x, y)$ shown as a white dot in Figure 63. The surrounding best and closest holes to the extracted pressure point are determined as shown in Figure 8 with white circles. If the "best" hole overlaps a lesion, encircled with red colour, the next closest "best" hole is chosen and the process is repeated to find out whether it overlaps the lesion or not. The 2-dimensional location of the corresponding "best" hole is stored in the stream of points subsequently sent to microcontroller in the case of "best" non-lesion hole shown as a circle with black colour in Figure 63.

The lesion detection process is divided into three main steps

- Step 1 is known as pre-processing; the patch is examined by scale and rotation invariant LBP to detect suspected lesion regions, using two different scales of LBP (8, 1) and (16, 2) respectively and compared with the stored LBP code histogram of normal pressure areas. If it doesn't match, step 2 is performed.
- In step 2, the patch of the plantar surface of the input image, suspected as a lesion in step 1, is further examined under SVM. The patch image serves as an input image and the SVM identifies whether the area lies on positive side, one side of the hyperplane, or on negative side, the other side of the hyperplane.
- In step 3, if SVM classifies the area enclosed in the patch as a lesion, the corresponding hole in the input image is encircled in red and the next "best" patch closest to the extracted pressure point patch is examined. The process is repeated until a normal pressure area patch is found.

All the lesions used in the study were taken from internet and a podiatrists files and superimposed (via Photoshop) on healthy feet used in the project work described in this Thesis. The algorithm was then executed for validation. The following images show the initial results. The result shows a fraction of false positive and false negative phenomena but this due to the lack of training. If the algorithm is trained with more lesion the detection rate will increase. This is proven in the result section.

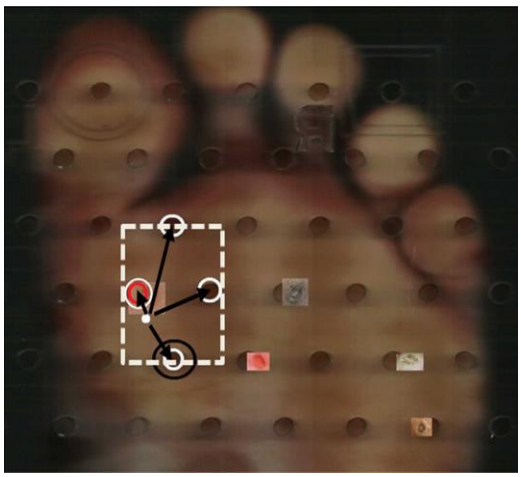

Figure 63: *Best perforated sheet hole selec-*

5.4 Probe Application over Non Lesion Area Algorithm Flow Chart

A probe assembly module was designed, I am not responsible for its design but the code that managed it, in-house using precision components and a commercial amplifier and calibrated to apply exactly 98mN ±1%. The module is driven by stepper motor controlled rails in both the X and Y-axes as it receives coordinates from the algorithms, a further Z-axis stepper motor is then used to drive the probe onto the plantar surface to apply exactly 98mN to each site in turn. The

overall flow diagram of the system is given in Figure 64.

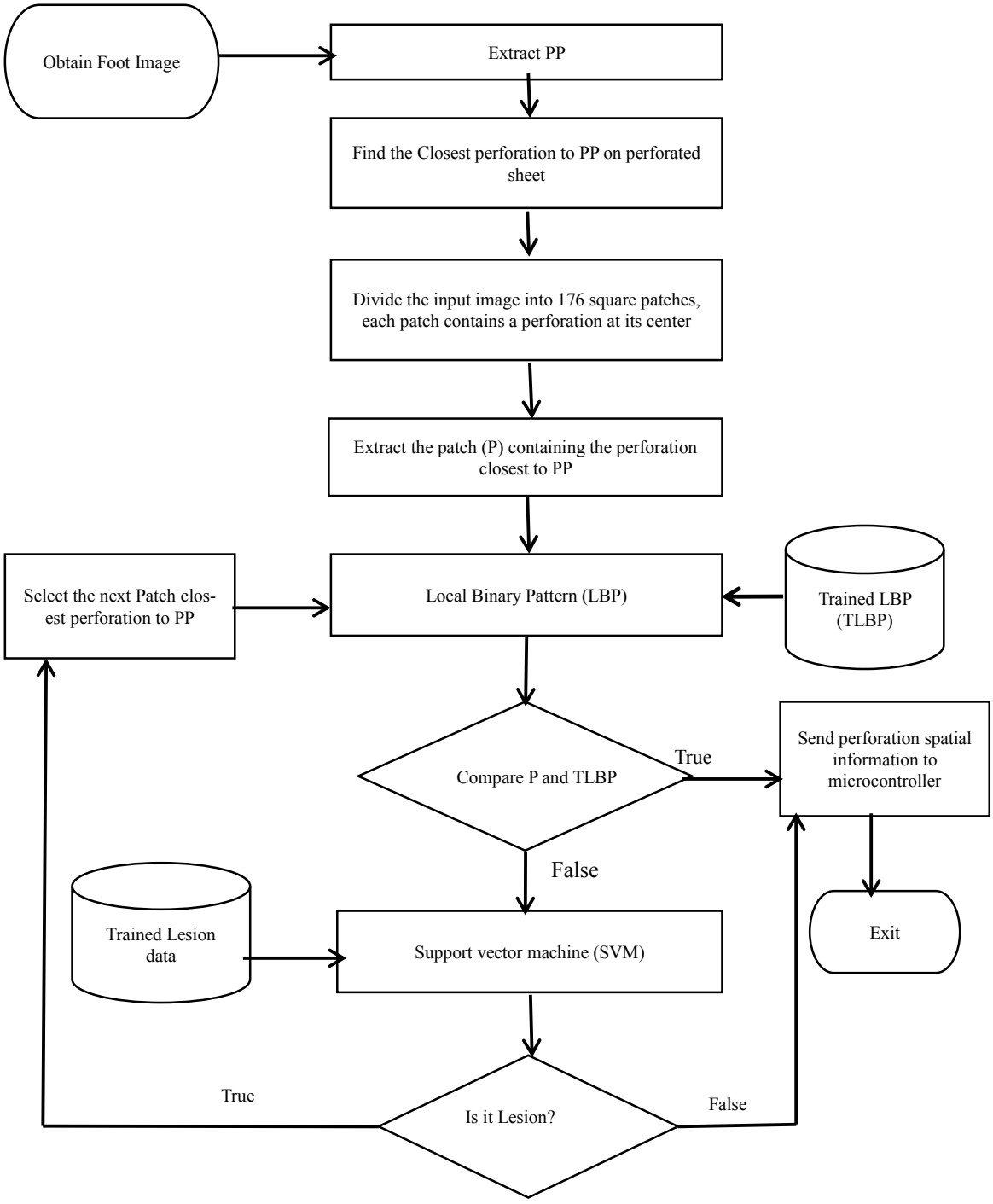

Figure 64: *Flow chart of PerSeNT lesion avoidance technique*

5.5 Result and Discussion

As previously discussed, LBP is trained with the patches shown in Figure 61 using different ethnic groups; Caucasian, Chinese, Asian and African. SVM is trained with lesions and patterns of normal pressure areas. All the lesions used were taken from internet and a trained podiatrist and superimposed on images of healthy feet. Figure 65 shows an image example superimposed with lesions at the pressure regions. The algorithm successfully detects these lesions and the adjacent hole lying on same pressure region normal plantar surface is selected.

In the current research scenario, the performance of the SVM is reciprocal with the window size. Keeping the SVM parameters the same, the larger the window size provides faster run times, but results in poor performance. A smaller size window has shown better performance of detecting patches that contain lesions but takes longer to process. Through repeated experimentation a window size 8 × 8 was found to be optimum. This window size was then used subsequently.

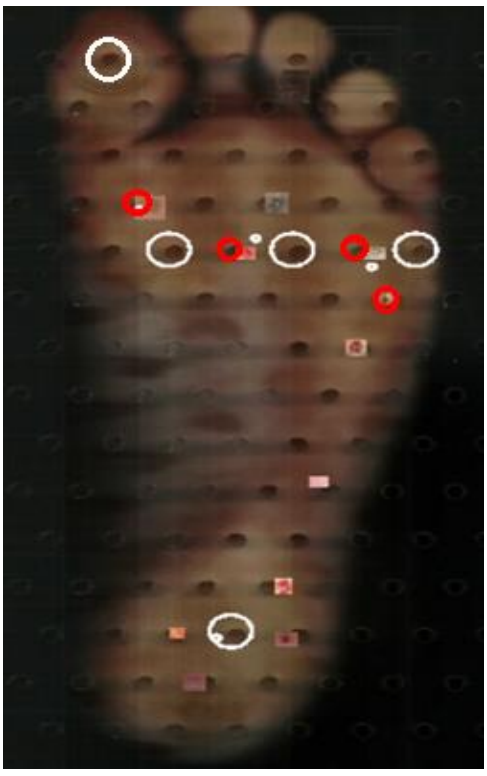

Figure 65: Next best hole selection

5.6 Conclusion

As presented, obvious care must be taken to recognise area where the probe must not be applied such as on lesions. A layered approach of LBP and SVM has been used in previously developed automated peripheral sensory neuropathy assessment using optical imaging to avoid probe application on lesion on plantar surface. Several different types of lesion are taken from internet and superimposed on plantar surface image. The proposed approach successfully detects all of the lesions available in database.

CHAPTER 6. Result and Analysis

In this chapter the PerSeNT system efficiency in terms of latency, accuracy and reliability are assessed. In detail, a comparison will be made between the time it takes to manually screen a person's foot for pressure points by a practitioner and the time the automated approach instantiated of PerSeNT takes. The accuracy of the automated approach refers to the correctness in the selection of the standard test five accepted pressure points under foot. In test 1, the PerSeNT accuracy is compared against the gold standard, this being the selection of the pressure points by a trained podiatrist. Moreover, in a second test the PerSeNT accuracy is compared to a commercially available pressure plate to test for pressure area detection accuracy. In the last test, user's signal detection and the reliability of PerSeNT is measured via the test-retest Pearson correlation coefficient.

The study was approved by the university ethics committee. Informed consent was obtained from each participant and the form is provided in Appendix 8.6.

In all experiments, the PerSeNT apparatus was set so that the machine was placed on the floor in front of a chair. All participants were given a prior demonstration about the posture required and experience of the magnitude of the force exerted by the probe. Subjects were then asked to place one barefoot on the perforated sheet, the foot image was scanned and pressure test points were extracted from the pressure regions. The same procedure was performed for the other foot.

6.1 Efficiency: Processing Latency Analysis

The overall efficiency of the PerSeNT system is tested against the manual SWME (Semmes Weinstein Monofilament Examination) method in terms of the time taken to screen a person's foot for pressure points. This evaluation included preparation time for the test, manual/automated reporting and manual/automated result storage. Timings for the PerSeNT system is shown in table 3. The PerSeNT activity flow can be seen in section *4.1.2.2.*

In the case of manual SWME process, it is difficult to accurately time each of the above

components, so the overall time was considered. A typical test on a participant was performed by a trained podiatrist and it was observed that the manual approach took on average 180 seconds per foot per trial between viewing the foot, making a pressure-point decision, final data handling and storage. On the other hand, PerSeNT took 47 second per foot per trial. For both the practitioner and the PerSeNT machine the SWM (Semmes Weinstein Monofilament) application was excluded. From the table below, where the data from this measurement exercise are reported, it appears that the automated approach is more than 2 minutes shorter than the manual one per foot.

Handshaking (PC and scanner) in the automated method is considered equivalent to the scene in the manual case of a patient sitting and preparing for the manual test, scanning the foot and pressure point extraction is equivalent to manual viewing of pressure points and preparing SWM, and the results' dissemination is equivalent to the practitioner writing the results of patient's test. This of course does not include any patient/practitioner interaction.

PerSeNT Activity	**Time (second)**	**Manual Activity**	**Time (second)**
Hand shaking (PC-Optical scanner)	4	Patient preparation for test	
Scanning foot	36	Viewing PP and prepar-ing SWM	
Pressure point extraction and result display	5		
Transmitting result over the internet	2	Writing test result	
Total time	47	Total average time	180

Table 3: *PerSeNT latency analysis*

6.2 Accuracy

6.2.1 Test No 1: Test Point Selection (Podiatrist VS PerSeNT)

To test the system's accuracy in the extraction of the test points under the foot (where to apply pressure), a qualified podiatrist with over 15 years' experience collaborated to compare the

automated and manual SWM pressure detection methods. Foot images from seventy multi-ethnic volunteers were provided and the podiatrist independently marked (with a blue dot) where she identified the five pressure points on each foot that would be used in the manual SWME and this is shown in the Figure 66. The podiatrist added a "circle of acceptance", also shown in black colour in the Figure 66, with a diameter of 1 cm bounding those points. Each of these images was stored separately from the automated findings. Every time the machine identified a pressure test point (white dot shown in Figure 66), the same area (anywhere inside the podiatrists drawn circle) a success was marked while a failure was assumed if the dot was not identified within the circle. The test showed a 100% success rate.

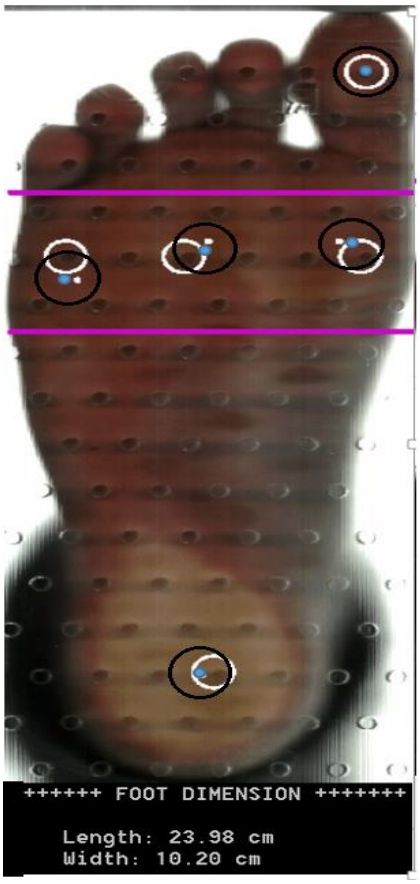

Figure 66: *Test points marked by PerSeNT and trained podiatrist.*

6.2.2 Test No 2: Test Point Selection from Pressure Region Test (PerSeNT Vs Pressure Plate)

To further validate the selection accuracy of the chosen pressure areas, a comparison of the

PerSeNT system and a commercially available pressure plate, which displays pressure region on the plantar surface when pressure is applied to the plate, known as footscan®PLTES (manufactured by RSscan) [113] was performed. The comparison was enacted to ensure that the PerSeNT innovative and unique embedded signal processing system extracted test points which lie inside actual pressure regions. The commercial system operates with a sampling rate of 125Hz and can record data up to 500 frames per second.

The embedded sensors resolution of 5mm × 7mm permit an accurate analysis of pressure deviations under all regions of the foot. Such commercial systems are considered for use in PSN detection methods but there are two major disadvantages: (A) The commercial system requires the participant to apply a large amount of force on the pressure mat to discover the pressure areas; This is not a problem for healthy participants here but would be problematic for diabetes sufferers with existing foot problem, display the added advantage of PerSeNT. (B) An automated follow-up of the mechanical probe cannot be performed meaning that a system with this approach could not be an all in one design. This is where the PerSeNT machine far exceeds anything currently in existence.

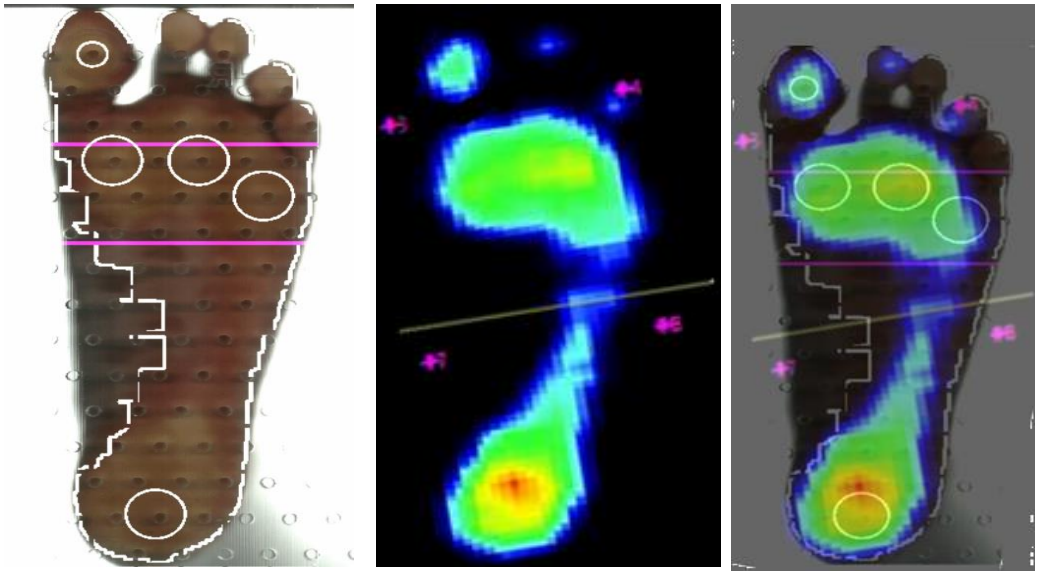

Figure 67: *(a) PerSeNT's detected pressure points (b) Pressure region detected by pressure plate (c) Superimposed image of (a) and (b)*

Nine healthy volunteers were selected from the original 70 and their foot images obtained using

the two approaches (automated and pressure plate) systems. The obtained images were then superimposed and qualitatively examined. It is found that almost 98% of the chosen points by the proposed system were selected from plantar pressure regions as shown in the Figure 67.

The test result analysis is summarised in the table 4. Thus the sensitivity of the PerSeNT vs pressure plate test is 97.7%

Total extracted Test point	45
Total extracted points by PerSeNT lying inside the pressure areas defined by the commercial plate	44
Average extraction of test points from the pressure region sensitivity/ true positive	97.7%
Incorrectly identified pressure test point or False positive	1
Average of false positive rate	2.2%

Table 4: *Pressure point selection from the pressu0re region detected by pressure plate.*

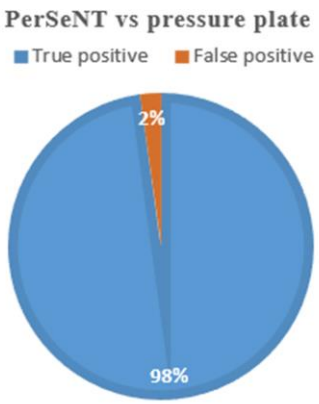

Figure 68: *True and False positive*

A failure occurred when/if the PerSeNT extracted test point did not fully match one of the pressure regions defined by pressure plate. The problem lay here with the pressure plate, where a slight tilt in the foot posture may shift the detected pressure regions. The (2%) failure consists of those points that were inside the accepted region according to podiatrist but were not inside the region detected by the pressure plate as a pressure region as shown in the Figure 69, where pressure plate image and PerSeNT image are superimposed. This issue was verified by the podiatrist. An example is shown in Figure 69 were the accepted extracted test

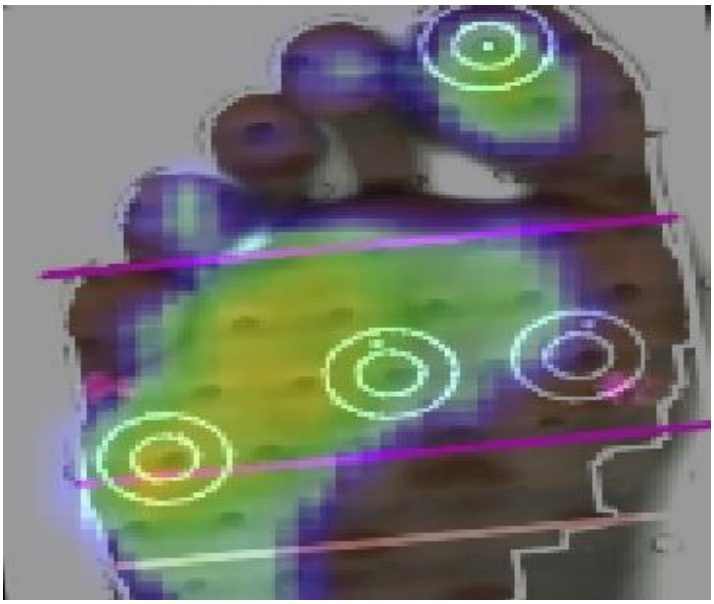

Figure 69: *First metatarsophalangeal PP extracted by PerSeNT lying outside the pressure region (highlighted by yellowish) extracted using the pressure plate.*

point by PerSeNT at first metatarsal is an acceptable location (podiatrist) but doesn't lie on the region detected as a pressure region by the pressure plate foot leaning and hence a change in pressure perceived by the commercial plate by the participant is obvious in the Figure 69.

6.3 Validity: Test No. 3

6.3.1 Signal Detection Theory and Test-retest Pearson Coefficient Reliability

Signal detection theory provides a general framework to analyse the accuracy of targets' detection occurring in uncertain or ambiguous situations. In the current test, the detection of a signal means the acknowledgement (pressing a push button) of the 98mN force applied by the probe on the plantar surface at the critical 5 pressure points. The 98mN is considered the correct and accepted force used by podiatrists using the accepted SWME method, thus the system was designed to apply the same pressure. If in future this is considered too low or too high then the PerSeNT system can simply be adjusted to new levels, this is much more difficult and costly for podiatrist in the field considering training and information costs as well as new instrumentation needs.

To ensure that the systems chosen probe method was appropriate and that the ability to detect a signal was appropriate for patients (10g of force through a hole of the perforated sheet) the following study was performed. Twenty-eight healthy subjects were tested in five sessions. Each session consisted of two consecutive subsessions; subjects undertook 2 trials in each subsession: one trial where the protruding probe touched the plantar face of the foot in five pressure regions and in another type of trial where the probe protruded but did not touch the foot (sham trial). A trial refers to a one complete test in which the foot was scanned and five extracted pressure points were detected and examined by the PerSeNT.

Hence it was possible to assess the proportion of HIT and FALSE Alarms in each session, thus obtaining a measure of accuracy of participants' ability to detect the actual probe pressing the foot. The procedure was repeated in five sessions, each 10 minutes apart. Within each session there were two sub-sessions in sequence. Each subsession comprised a random sequence of 2 trials with respect to both the location of the plantar surface pressure area being touched and the trial being either real or sham.

Furthermore, and importantly, in order not to bias the measurement outcome, the delivery of each sequence occurred in a double-blind format (i.e. neither the experimenter nor the participants were aware of the type of stimulation delivered during any single trial, i.e. either real or sham).

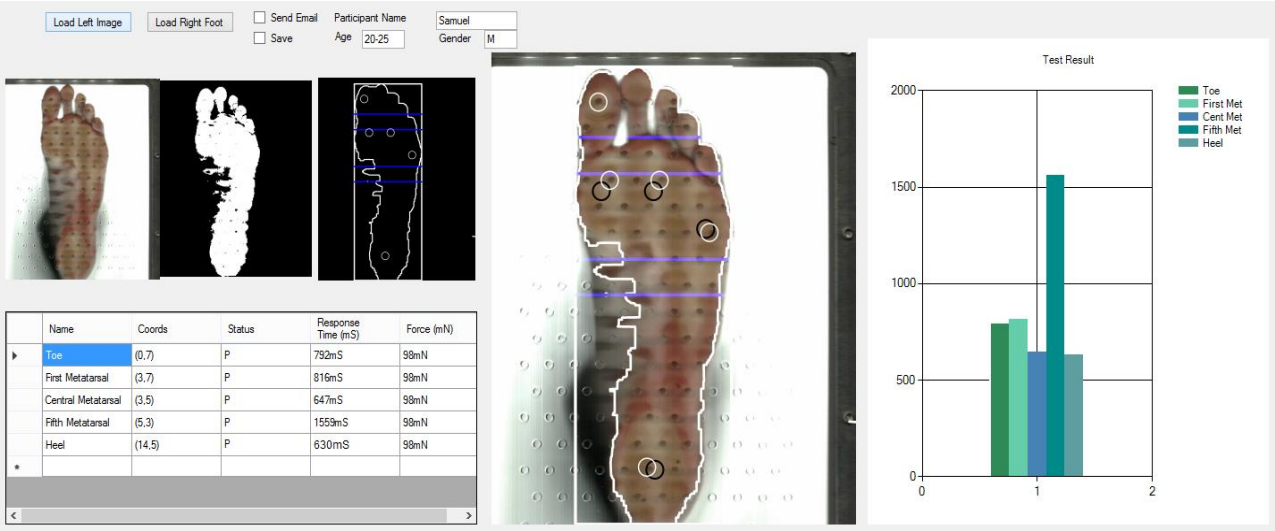

Figure 70: *Real test with PerSeNT*

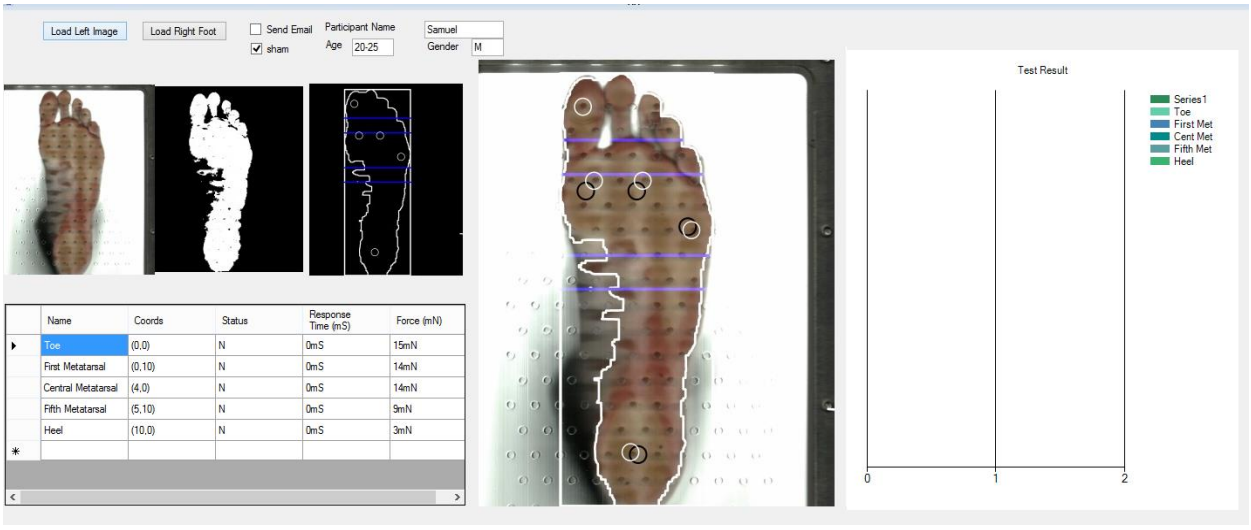

Figure 71: *Sham test with PerSeNT*

Overall, this procedure allowed the assessment of the extent to which participants' responses correlated across sessions, i.e. high test-retest correlations support reliable measurements.

6.3.1.1 Signal Detection Test Results: Sensitivity & Specificity (Validity)

Initially the accuracy of a total number of subjects 28 tested in all five sessions of
10 real and 10 sham trials was measured.
Total number of participant was 28, a computer code was developed for PerSeNT machine to conduct the real and sham trials. Overall, the number of times the probe was applied in the real test was 1400: Total number of trials (Real/Sham) × total number of subjects × total number of test points in a subject = 10 × 28 × 5.
The number of trials where the probe was detected (Hit event) was 1265, and those where the probe was not detected (Miss event) was 135.

In the case of the 1400 sham trials, no False Alarms occurred, therefore "Correct" rejections numbered 1400. Table 5 below summarises the data.

Thus the Sensitivity of the test (true positive correctly identified as such – i.e. Hit/ (Hit + Miss) = 1265/ (1265+135)) is 0.9 and its specificity (true negative correctly identified as such, i.e. Correct Rejection / (Correct Rejection + False Alarm) = 1400/ 1400+0 = 1.

		Signal (Probe application)	
		Present	Absent
Re-sponse	Present	1365/1400 = 0.90	0
	Absent	135/1400 = 0.096	1400/1400= 1

Table 5: *Signal detection results*

The above test result shows a clear discrimination of the signal (real test) from the noise (sham test) occurred: no participant falsely detected the probe when it was not applied on the plantar surface. Given the absence of false alarms no measure of d' score was performed and the following analyses were performed on Hit rates.

6.3.1.2 Test-retest Pearson coefficient correlation

Reliability, the consistency of a test or measurement, is frequently quantified in research literature

e.g. test-retest Pearson coefficient correlation. A test is given at some time and the same test under the same conditions is repeated after a designated time period [114]. The score of both tests are then correlated. This correlation is known as the test-retest Pearson coefficient correlation or the coefficient of stability. A correlation coefficient tells us to what extent people obtain relatively stables scores across two testing occasions [114]**.** A reliability coefficient above 0.70 is considered relatively stable over time and a reliability coefficient between 0.80 and 0.90 suggests strongly reliable results [114].

To assess the reliability and repeatability of the PerSeNT system, the following analysis was carried out, based on the Hit rates using the same data acquired in section 6.3.1. The Hit is the sub-session when the probe was physically applied to the plantar surface of the participants.

In the table 6, the first column is the number of participants and the next ten columns contain the number of hit responses to the 98mN force applied by the probe out of 5 probes applications in each trial. The value 1 stands for the correct detection of all the five probes, 0.8 means 4 out of 5 probe hits has been correctly detected and 0.6 is the score for 3 out 5 probe acknowledgements. The last two columns are the mean and standard deviation for each participant across the 10 trials. While the bottom two rows show the mean and standard deviation values across participants for each sub-session.

It can be seen that the means per subject vary from 0.66 to 1 across the 28 participants for the 10 trials, while means varied between 89% and 91% across trials for the 28 participants.

On the basis of hit ratio, the 280 cells in table 6 could be categorised into *A*, *B* and *C* categories as shown in table 7. Category *A* represents 3 out of 5 hit ratio, *B* represents 4 out of 5 hit ratio and *C* represents 5 out of 5 hit ratio i.e. 0.6, 0.8 and 1 respectively.

	Session1		**S2**		**S3**		**S4**		**S5**			
	Subsession (sub)1	**Sub2**	**Sub3**	**sub4**	**Sub5**	**Sub6**	**Sub7**	**Sub8**	**Sub9**	**Sub10**		
	Hit	**Hit**	**Hit**	**Hit**	**Hit**	**Hit**	**Hit**	**Hit**	**Hit**	**Hit**	**Mean**	**STDEV**
1	0.8	0.8	0.8	0.8	0.8	0.8	0.8	0.8	0.8	0.8	**0.8**	**0**
2	0.8	0.8	0.8	0.8	0.8	0.8	0.8	0.8	0.8	0.8	**0.8**	**0**

3	1	1	1	1	1	1	1	1	1	1	**1**	**0**
4	1	1	1	1	1	1	1	1	1	1	**1**	**0**
5	0.8	1	1	1	1	0.8	1	1	0.8	0.8	**0.92**	**0.1**
6	1	1	1	1	1	1	1	1	1	1	**1**	**0**
7	1	1	1	1	1	1	1	1	1	1	**1**	**0**
8	0.8	1	1	1	0.8	1	1	1	1	1	**0.96**	**0.08**
9	0.8	0.8	0.8	0.8	0.8	0.8	0.8	0.8	0.8	0.8	**0.8**	**0**
10	0.8	1	0.8	0.8	0.8	1	0.8	1	1	1	**0.9**	**0.11**
11	1	1	1	1	1	1	1	1	1	1	**1**	**0**
12	0.8	1	0.8	1	1	1	1	0.8	0.8	0.8	**0.9**	**0.11**
13	0.8	0.8	0.8	0.6	0.8	0.8	0.6	0.6	0.6	0.8	**0.72**	**0.1**
14	1	1	1	1	1	1	1	1	1	1	**1**	**0**
15	0.8	1	0.8	1	1	0.8	1	1	1	1	**0.94**	**0.1**
16	0.8	0.8	0.8	0.8	0.8	0.8	0.8	0.8	0.8	0.8	**0.8**	**0**
17	1	1	1	1	1	1	1	1	0.6	0.6	**0.92**	**0.17**
18	0.8	0.8	0.8	0.8	0.8	0.8	0.8	0.8	0.8	0.8	**0.8**	**0**
19	1	1	1	1	1	1	1	1	1	1	**1**	**0**
20	1	1	1	0.8	1	1	1	0.8	1	1	**0.96**	**0.08**
21	1	1	0.8	1	1	0.8	1	1	1	1	**0.96**	**0.08**
22	0.8	0.8	0.8	0.8	0.8	1	1	1	1	0.8	**0.88**	**0.1**
23	0.8	0.6	1	0.6	0.6	1	1	1	0.6	0.6	**0.78**	**0.2**
24	0.6	0.6	0.6	0.6	0.8	0.8	0.6	0.6	0.6	0.8	**0.66**	**0.1**
25	1	1	1	1	1	1	1	1	1	1	**1**	**0**
26	1	1	1	1	1	1	1	1	1	1	**1**	**0**
27	0.8	0.8	0.8	0.8	0.8	0.8	0.8	0.8	0.8	0.8	**0.8**	**0**
28	1	1	1	1	1	1	1	1	1	1	**1**	**0**
Mean	**0.89**	**0.91**	**0.9**	**0.89**	**0.91**	**0.92**	**0.92**	**0.91**	**0.89**	**0.89**		
STDEV	**0.11**	**0.13**	**0.12**	**0.14**	**0.12**	**0.1**	**0.13**	**0.13**	**0.15**	**0.13**		

Table 6: *Real trial test statistics*

Table 7 and Figure 71 show that the performance mode is category C i.e. 5 out 5 real trials correctly detected by participants (one at toe, three at metatarsals and one at heel).

Category	Hit Ratio	N. of Cells
A	0.6	18
B	0.8	99
C	1	163

Table 7: *Categorisation of participant base on the Hit Ratio*

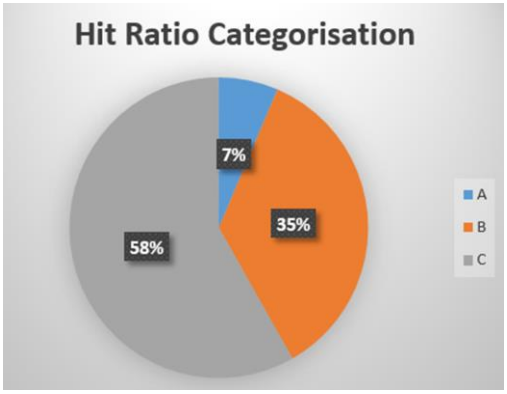

Figure 71: *Pi Chart representing the Hit Ratio amongst categories A (100 hits rate), B (80% hits rate) and C (60% hits rate).*

The next table, table 8, consists of the mean of first five real trials and the last five real trials shown in table 6 for each participant (Sub1-5 and Sub6-10). The last column provides the difference between Sub1-5 and Sub6-10. Figure 72 shows Graphical representation of two test groups' correlation.

	Sub1-5	Sub6-10	Differences Sub1-5 and Sub6-10
1	0.800	0.800	0.00
2	0.800	0.800	0.00
3	1.000	1.000	0.00
4	1.000	1.000	0.00
5	0.960	0.880	-0.08
6	1.000	1.000	0.00
7	1.000	1.000	0.00
8	0.920	1.000	0.08
9	0.800	0.800	0.00
10	0.840	0.960	0.12
11	0.800	0.800	0.00
12	0.920	0.880	-0.04
13	0.760	0.680	-0.08
14	1.000	1.000	0.00
15	0.920	0.960	0.04
16	0.800	0.800	0.00
17	1.000	0.840	-0.16
18	0.800	0.800	0.00
19	1.000	1.000	0.00
20	0.960	0.960	0.00
21	0.960	0.960	0.00
22	0.800	0.960	0.16

23	0.720	0.840	0.12
24	0.640	0.680	0.04
25	1.000	1.000	0.00
26	1.000	1.000	0.00
27	1.000	1.000	0.00
28	1.000	1.000	0.00
Mean			***0.007***
Correlation			**0.832**

Table 8: *Correlation between first five real tests and last five real tests*

The test-rest reliability coefficient or the coefficient of stability or Pearson's correlation coefficient *r* between the first five and last five sub-sessions is 0.832, which is quite high and shows a strongly reliable performance of the test. A second analysis was performed to assess test re-test stability. Given that it is possible to have a perfect test re-retest correlation when there is a constant difference between performance at time 1 and time 2 (e.g. each participant detects 100% hits at time 1 and 80% hits at time 2), the extent to which performance was reliable and stable in absolute terms was assessed. To this aim the performance for the first 5 trials was subtracted from the performance for the last 5 trials. This was done for each participant and their mean was calculated. If performance is stable and constant over time, this difference should be close to zero. Indeed, this difference was found to be negligible, i.e. 0.007 (t = 0.55, p > .10). Therefore, participants showed reliable test retest performances that were very similar in precision across test and retest sub-sessions.

A further analysis was performed to identify any systematic patterns in sites where correct detection was hard. The overall miss ratio, out of 1400, at toe, first, fifth, central metatarsal phalangeal joints and heel were 0.5%, 1.29%, 0.86%, 0.64% and 6.35%, respectively.

Taking into account the total of the 135 Miss events, it appears that the Miss ratio at the toe was 5.19%; at the first metatarsal phalangeal

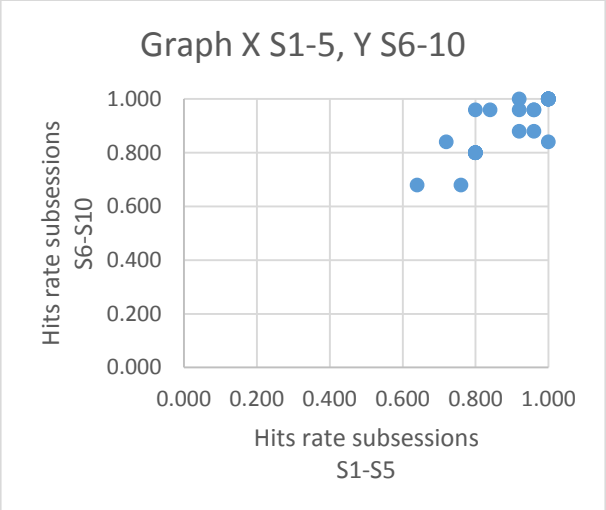

Figure 72*: Graphical representation of two test groups' correlation*

joint area was 13.3%; at fifth metatarsal phalangeal joint area was 8.88%; at the central metatarsal was 6.66%; and at the Heel it was 65.9% as shown in Figure 73. This means contribution of Heel in miss ratio is higher.

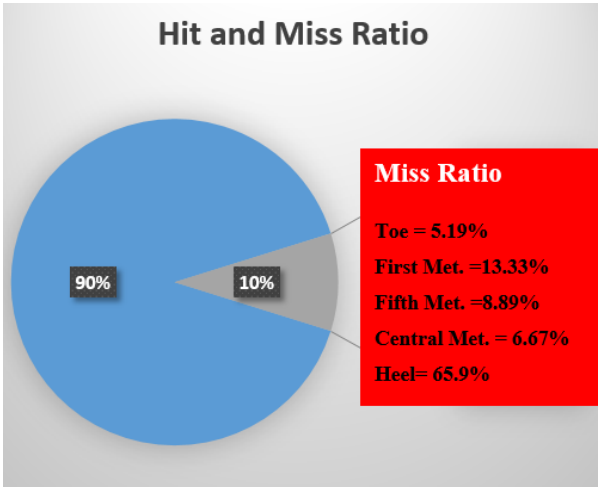

Figure 73: *Pi Chart representing the Hit and Miss Ratio*

From the above test, it is evident that an area of concern for accurate detection using PerSeNT is the Heel. This phenomenon also confirmed by the podiatrist that the heel is the least sensitive area. J. Clifford et al. [115] and W. I. Rhee et al. [116] also showed that heel is the least sensitive site, with 1/6th the sensitivity of the most sensitive toes. A large proportion to the failure in recognising the probe at heel leads to the question for further study, which is beyond the scope of this report. Further research must be done to either revisit the magnitude of the force (98mN) applied at heel or perhaps reconsider the heel as being an important pressure point to detect neuropathy.

6.4 Conclusion

The automated SWME replica, PerSeNT, was compared with the manual SWME through a number of tests. In test1, the proposed system was found 100% accurate in selection of suitable test points and about 4 times more efficient in terms of latency. Further comparison of PerSeNT was made with a commercially available pressure plate in test 2. A high success rate of 97.7% was achieved and showed that all the extracted test points by PerSeNT were from pressure regions of the plantar surface. Test 3 consisted of two phases; phase 1 signal detection theory test was exercised and it was found that no false alarm had been detected. In phase 2, it has been observed that out of 28 healthy volunteers, most (58%) have recognised the probe and 35% recognise probe at 4 pressure regions while 7% failed to recognise at 2 out of five pressure regions. Further investigation revealed that the heel is the area where most of recognition failures occurred in category A and B. This was expected as heel is the least sensitive area. Further investigation must be carried out to either reconsider the magnitude of force at heel or reconsidered the heel as being an important pressure point to detect sensory neuropathy. These tests evaluations support the system repeatability, reliability and efficiency.

CHAPTER 7. Conclusion

Diabetes Mellitus is a chronic illness and may lead to peripheral neuropathy. Lack of proper care and management of peripheral neuropathy may result in amputation. The current direct cost of patient care for those living with diabetes is estimated at £10 billion which is 10% total UK National Health Service budget. Regular screening of diabetic patients is required for the assessment of peripheral sensory neuropathy. The Semmes–Weinstein Monofilament Examination (SWME) is one of the most common methods to test pressure points at specific weight-bearing areas, namely the toe (Hallux), metatarsal and heel (Calcaneum) and the test incurs its own downsides. The key disadvantage is the potential misjudgement of acceptable force. The precision of the accepted 10g force is based on the practitioner's guess by observing the perceived bend or buckle of the filament i.e. observing the 10 mm bend through the naked eye. Therefore, there is a clear need to further, simplify and automate the testing procedure that is, autonomous, repeatable, and simplifies the testing procedure with the storage capacity of photographic evidence of patients' feet and their condition over time.

Selection of pressure points from the chosen pressure regions is vital and provides key information to be used in medical diagnosis associated with satisfactory function in the foot. Plantar pressure measurements systems range from simple scheme e.g. ink prints, clay, sensitive films to more complex innovations such as pedobarograph, force transducers, capacitive sensors, resistance sensors, piezoelectric sensors, piezoresistive sensors and strain gauge mechanical systems. These systems come into two categories: design platform and in-shoe. Further these can be classified into qualitative and quantitative measurements. Though their research objectives are diverse, the methods followed by those referenced involved manual intervention and seems impractical to embed automated probe application mechanism.

The Thesis presents as far as the author is aware, the first complete off the-shelf system for automated selection of pressure points for peripheral neuropathy assessment of a diabetic patient's plantar surface using optical imaging and binary processing techniques. In this approach a scanner is used to obtain the patients plantar surface image in RGB colour space. Then via developed image

processing using a specific colour space that represents skin colour and three largest size of contours, the orientations of pressure points are identified. This information is then sent to a robotic arm holding a monofilament probe. The robotic arm is used to conduct the Semmes–Weinstein Monofilament Examination (SWME) procedure as it is exercised in hospital or health care centre manually. Patient's feedback is recorded to identify the insensate area of plantar surface. All ethnic groups were considered and tested. The proposed method performs a thresholding process and bounds the foot image in a rectangle followed by contours. Plantar pressure points are then obtained using a combined approach of optical imaging over the HSV three-dimensional colour space and plantar anthropometry. The algorithm was successfully applied on 70 participants with a 100% success result, regardless of the patient's race, age or gender. The introduction of foot grove method embedded in perforated sheet mitigated the issues related to the original foot stopper (FS) but at the same time foot placement is dependent on the toe groove. It is sometimes difficult to locate the toe groove easily, thus new approach was considered. The foot sectorisation algorithm, subsequent image processing and grid information algorithms presented reliably identify the plantar surface sensory neuropathy pressure points on a given patient's foot. This approach is generic and accommodates flat and non-flat feet as well as different ethnicities.

Due to the automation of the system, obvious care had to be taken to ensure lesions are detected (or characteristics that could be a lesion) and the probe is not applied to those areas. A layered approach of LBP and SVM is used in previously developed automated peripheral sensory neuropathy assessment using optical imaging to avoid probe application on lesion on plantar surface. Several different types of plantar lesions were taken from appropriate internet sites and the collaborating podiatrists' collection. These were then experimentally superimposed on plantar surface images of feet already stored. The proposed approach successfully detected all of the lesions available in database.

The efficiency, reliability and validation stages were the final set of tests. The study was approved by the university ethics committee. Three different tests carried out, Test 1 was the verification of PerSeNT selection of test point and a trained podiatrist, the results showed 100% success rate. In test 2 a comparison has been made between PerSeNT and commercially available pressure plate

to make sure the PerSeNT extracts test points from plantar pressure region. A high success rate of 97.7% was observed. Signal detection test was carried out in test 3, phase 1 was executed to find out the discrimination of true and false alarm, it was observed that no false alarm been detected. In phase 2, it has been observed that out of 28 healthy volunteer, most (58%) have recognised the probe and 33% recognise probe at 4 pressure region while 25% failed to recognise at 2 different pressure region. Further investigation revealed that the heel is area where category A and B most of the time was failed to recognise the probe. This was expected as heel is the least sensitive area. Further investigation must be carried out to either reconsider the magnitude of force at heel or reconsidered the heel as being an important pressure point to detect sensory neuropathy. These tests evaluations support the system repeatability, reliability and efficiency.

CHAPTER 8. Appendix

8.1 Portable scanner

Copy Cat is a handheld, portable scanner used to capture books, papers, photos and other documents on the go with high-resolution up to 600 DPI and saves files to an included micro SD card. Copy Cat also has a USB cable to connect the portable scanner to the RPi as a USB drive.

It inherits a limitation in terms of scanner mode and memory mode. It serves as a scanner when disconnected with RPi and serves as a USB drive when connected to RPi. A hardware arrangement is designed and code is developed to toggle it in between two modes i.e. scanner and USB drive.

8.2 Usbmount.sh

A bash script (usbmount.sh) is written so that RPi's operating system (Debian wheezy) can mount the USB drive mode of portable scanner.

```
#!/bin/bash
Sudo chmod 775 /media/usbstick
for ch in {a..z}
do
s='sd'
d=$ch
num='1'
drivename=$s$d$num
sudo moun –t vfat –o uid=pi,gid=pi /dev/$drivename /media/usbstick
done
```

8.3 USBUNmount.sh

It is a bash file that is used to unmount the USB drive (scanner in USB mode) from RPi safely. The script runs immediately after the image is fetched from the scanner SD card by a c++ code

8.4 C/C++ Image processing code

C/C++ Image processing code (getPlantarImage.cpp) is developed to extract pressure points of plantar surface. Another C/C++ code (SerialComm.cpp) is written to establish the serial communication between RPi and Arduino. First a connection is established by the code

```
cs=open("/dev/ttyACM0", O_RDWR | O_NOCTTY);
struct options_at;
```

tcgetattr(cs, &options_at);

speed_t bdrate = B9600;

cfsetispeed(&options_at, bdrate);

cfsetospeed(&options_at, bdrate);

The image processing code runs in RPi in waiting mode.

while (signal !='$')

{ signal=readFromArduino(); }

As the "getPlantarImage.cpp" gets a signal from Arduino to indicate that the Arduino has run the scanner and connected the scanner with RPi and toggled it into USB drive mode.

"getPlantarImage.cpp" fetches the image

*CvCapture *pCapturedImage =*

cvCaptureFromFile("/media/usbstick/DCIM/100MEDIA/image1.jpg");

frame = cvQueryFrame(pCapturedImage);

The "getPlantarImage.cpp" extracts pressure points using optical imaging and plantar anthropometry these points are sent to Arduino sketch in a stream of characters each digit in a pair is separated by " ' " and each pair in the character string is separated by " : ".

8.5 Arduino_Serial_Communication.ino

The code on Arduino side receives the string from "getPlantarImage.cpp" and convert the string into respective digits to represent the special domain of pressure point. It stores the x coordinate into xx variable and y coordinate into yy variable. The xx represents row number of perforated sheet while yy represents the column number of the perforated sheet e.g. if a string consists of 4,7:3,5:

The variable xx will contain 4 and yy will contain 7, it represents the hole on perforated sheet at 4th row and 7th column. And similarly 3,5 represent hole on perforated sheet located at 3rd row and 5th column

intinput,num,xx,yy;

intbuff[5];

int j=-1;

void setup() {

Serial.begin(9600);

```
        pinMode(ledx, OUTPUT);
        pinMode(ledy, OUTPUT);
        Serial.println('$');}
intcalc() {
intnum=0,x=0;
    for(x;x<=j;x++)
      num=num+(buff[x]-48)*pow(10,j-x);
   return num;
}

void loop() {
  if(Serial.available()>0)
  {  input=Serial.read();
     if(input==',') {
        xx=calc();    // Row number of
        j=-1;
        Serial.print(xx);
        Serial.println( " , ");
        for(inti=0; i<xx; i++)  {
        digitalWrite(ledx, HIGH);
        delay(500);
```

```
      digitalWrite(ledx, LOW);
      delay(500);
       }   }
   else if(input==':')  {
      yy=calc();
      j=-1;
      Serial.println(yy);
     for(inti=0; i<yy; i++)   {
      digitalWrite(ledy, HIGH);
      delay(500);
      digitalWrite(ledy, LOW);
      delay(500);
       } }
   else      {
      j++;
      buff[j]=input;
 }
} }
```

8.6 PerSeNT information form

London South Bank University

PARTICIPANT INFORMATION SHEET: UREC No. 1438

Peripheral Sensory Neuropathy Tester (PerSeNT): A machine to test for loss of sensation in the extreme regions of the foot, Toes, heel, foot surface.

Invitation

You are invited to participate in a research study for the improvement and validation of a novel machine PerSeNT that automatically test for Peripheral Sensor Neuropathy (PSN) or a lack of sensation, in the foot. It has been reviewed and ethically approved by the London Southbank University Research Ethics Committee.

The study is part of an inter-school research project between Applied Health and Engineering. The work is being sponsored by the university's enterprise centre (contact Mr. Peter Hadfield) and is being conducted by Dr Sandra Dudley-McEvoy (Principal Lecturer, EED), Mr Hafeez Siddiqui (PhD student, EED), Dr Michelle Spruce (Fellow, Health) and Dr Steve Alty (Senior Lecturer, EED).

Before you decide whether or not you wish to participate in this study, it is important for you to understand why the research is being done and what it will involve. Please take the time to read the following information carefully and discuss it with others if you wish.

1. What is the purpose of this study?

The purpose of the study is to assist the research team to improve and validate a novel LSBU automated system that tests for peripheral sensor neuropathy (PSN) in patients.

Currently the accepted method is the Semmes–Weinstein Monofilament Examination (SWME) where a practitioner holds a patient's foot and decides upon their foot pressure points. The practitioner then applies a 10g monofilament probe to the plantar surface (underside) of the foot to the areas he/she recognised as the pressure points, normally the toe, heel and metatarsal areas. Once the practitioner notes a bend in the monofilament representing (what they believe to be) a 10g force, the patient is required to say where they can feel the probe or not.

The proposed automated machine works without a practitioner present and replicates the visual pressure point detection in an automated way using optical imaging (scanner) and signal processing techniques. The optical scanner of the PerSent system takes a digital image of your foot. Following this an automated mechanical probe of 10g will be applied to each foot. No investigations apart from the automated pressure point detection and manual recognition of the probe will be requested. This study aims to (a) validate the pressure point imaging technique against a commercial system and (b) the repeatability of a mechanical probe to apply 10g or 98mN of pressure.

2. Why have I been invited to participate in this study?

We are asking healthy post-graduate students and staff to participate. You are eligible to participate in this study because you are a postgraduate student or staff member at London South Bank University.

3. What if I don't want to take part in this study, or if I want to withdraw later?

Participation in this study is voluntary. It is completely up to you whether or not you participate.

If you wish to withdraw from the study once it has started, you can do so at any time and at any stage without having to give a reason. At your test you will be given a code that matches your foot image, probe recognition, sex, age, and ethnicity information. This will be used to remove your data. We will not have details of names or addresses.

4. What does this study involve?

If you agree to participate in this study, you will be asked to sign the Participant Consent Form.

This study will be conducted for 30 mins over 3 days. You will only be required for one of those 30 minutes' sessions.

Once you have signed the consent for you will be asked to do the following.

a) You will be provided with a demonstration prior to the test.

b) You will be asked to place your right foot first on the scanner in front of you. You will be verbally guided (ONLY) to place your foot in the correct position. You do not need to apply any pressure. You can be seated or standing this is up to you.

c) The scanner will then take an optical image of your foot and a digital scanned foot image will be presented on the screen in front of you.

d) Once the scan is completed a pressure map of your foot is automatically produced again on the screen in front of you.

e) Once the test is completed the machine will return to its initial position.

f) Following this, the mechanical probe will start. This will apply 98mN (10g) of pressure to 5 places on your foot using the info found in (d). You will be asked to press a button to declare whether you have felt the probe or not. Nothing else will be asked of you.

a) Once your right foot is completed you will be asked to do the same again for your left foot

b) Following this you will be asked to stand with both feet on the commercial plate and a pressure point scan will be conducted.

c) You will be provided with your results and asked to comment on your experience.

5. How is this study being paid for?

The study is being sponsored by LSBU. No money is paid directly to individual researchers.

6. Are there risks to me in taking part in this study?

There are no visible risks to the study and you will not be asked to do anything except present a bare foot onto the PerSeNT box and commercial pressure plate.

7. Will taking part in this study cost me anything, and will I be paid?

Participation in this study will not cost you anything. A voucher for a soft beverage will be provided and which will be issued upon completion of your visit.

8. What will happen to my scanned image after they have been used?

The anonymised digitally scanned images of feet will be stored until the completion of the study (1 year). You will be provided with a code once you start the test. This will match your data as explained in 3 above. No names will be taken.

9. How will my confidentiality be protected?

All testing will be anonymous. No names or addresses will be taken. You will be asked for your age, ethnicity and sex prior to starting the test. Only Dr Sandra Dudley-McEvoy, Dr Michelle Spruce and Mr Hafeez Siddiqui will know whether or not you are participating in this study. Only the researchers named above will have access to those details and results will be held securely at LSBU. Please be aware names or addresses **will not be taken.**

10. What happens with the results?

If you give us your permission by signing the consent document, we plan to discuss/publish the results at peer reviewed IEEE journals and to provide evidence for future research grants.

In any publication, information will be provided in such a way that you cannot be identified. Published results of the study will be provided to you, if you wish.

11. What should I do if I want to discuss this study further before I decide?

When you have read this information, the researchers Dr Sandra Dudley-McEvoy

(dudleyms@lsbu.ac.uk, 020 7815 7124) and Mr Hafeez Siddiqui (siddiqh3@lsbu.ac.uk) will discuss it with you and any queries you may have. If you would like to know more at any stage, please do not hesitate to contact them.

Finally, if you remain unhappy and wish to complain formally, you can contact the Chair of the University Research Ethics Committee. Details can be obtained from the university website: https://my.lsbu.ac.uk/page/research-degrees-ethics

Thank you for taking the time to consider this study.

If you wish to take part in it, please sign the attached consent form.

This information sheet is for you to keep.

8.7 Participant Consent Form

Department of Engineering and Design

London South Bank University

Study Title: PerSeNT

Participant Consent Form: UREC No. 1438

Research Team: Dr. Sandra Dudley-McEvoy (Principle Investigator): dudleyms@lsbu.ac.uk Tel. ext:7124

Dr. Michelle Spruce (Principle Practice Investigator): (michelle.spruce@btinternet.com)

Mr. Hafeez Siddiqui (PhD Student) siddiqh3@lsbu.ac.uk: Tel. ext:7545

Research Ethics Committee: (ethics@lsbu.ac.uk)

Please circle Y or N

(a) I have read the attached information sheet on the research in which I have been asked and agree to participate and have been given a copy to keep. I have had the opportunity to discuss the details and ask questions about this information
(Y/N)

(b) The Researcher has explained the nature and purpose of the research and I believe that I understand what is being proposed
(Y/N)

(c) I understand that my personal involvement and my particular data from this study will remain strictly confidential. Only researchers involved in the study will have access.
(Y/N)

(d) I consent that scanned digital images using an optical scanner will be taken of my feet and

securely stored at LSBU.
(Y/N)

(e) I understand that I am free to withdraw from the study at any time without giving a reason.
(Y/N)

(f) I consent that a mechanical probe will be brushed against my foot.
(Y/N)

(g) I understand that the images will be anonymised, only sex, age and ethnicity will be recorded.
(Y/N)

If you have any questions, please ask.

I **consent** taking part in this study

Participants name (Block Capitals) _____

Participants name (Signature) _____

Witness Name (Block Capitals) _____

Signature of Witness: _____

Date: _____

9. REFERENCES

[1] NHS (2012, November 6th). "Failings in diabetes care 'cost thousands of lives,".nhs.co.uk. Available from: http://www.nhs.uk/news/2012/11November/Pages/Failings-in-diabetes-care-cost-thousands-of-lives.aspx [Accessed 10/22/13].

[2] Diabetes: Fact And Stats, Daibetes UK Care. Connect. Campaign.

[3] N. Hex, C. Bartlett, D. Wright, M. Taylor and D. Varley. (2012). "Estimating the current and future costs of Type 1 and Type 2 diabetes in the UK, including direct health costs and indirect societal and productivity costs," Diabeteic Medicine DOI: 10.1111/j.1464-5491.2012.03698.x

[4] A. J. M. Boulton, D. G. Armstrong, S. F. Albert, R. G. Frykberg, R. Hellman, M. Kirkman, L. A. Lavery, J. W. Lemaster, J. L. Mills, M. J. Mueller, S. Peter, K. W. Dane, "Comprehensive Foot Examination and Risk Assessment", Diabetic Care, Vol. 31, Pp. 1679-1685.

[5] K.P. Mothiram, B.M. Vasanth, M.B. Mahesh, R. Parivalavan, V.B. Narayanamurthy and V.S. Ganesan, "New Methods And Parameters For Dynamic Foot Pressure Analysis In Diabetic Neuropathy", 19th International Conference IEEE EMBS, Chicago USA, Pp. 1826-1828, Nov. 2, 1997.

[6] CDA (2013, April) "Nerve Damage (Diabetic Peripheral Neuropathy)," http://www.diabetes.ca. Available from: http://www.diabetes.ca/diabetes-and-you/complications/nerve-damage-diabetic-peripheral-neuropathy [Accessed 05/9/14].

[7] HSCIC (2012) National Diabetes Audit 2011–12. Report 2: Complications and Mortality.

[8] M. S. Irene, I. A. Amanda, H. W. N. Andrew, R. M. David, E. M. Susan, A. C. Carole, H. David, C. T. Robert, R. H. Rury, "Association of glycaemia with macrovascular and microvascular complications of type 2 diabetes (UKPDS 35): prospective observational study," the biomedical journal, vol. 321, August 2000. http://www.bmj.com/content/321/7258/405 [Accessed 2014].

[9] Khanolkar, MP et al. (2008) The Diabetic Foot. QJ Med 101: 685– 695

[10] G. David, N. Singh, Armstrong, A Benjamina, Lipsky. (2005 Jan). "Preventing Foot Ulcers in Patients With Diabetes" The Journal of the American Medical Assoication Available: http://jama.jamanetwork.com/article.aspx?articleid=200119 [Accessed 04/08/2012].

[11] NHS (2014, October). "Improving the Care of the Diabetic Foot Ulcer – Better prevention, diagnosis, treatment". Available from: http://www.sbrihealthcare.co.uk/wp-content/uploads/2014/10/SBRI_8_Diabetic_foot_ulcer_Brief.pdf. [Accessed 12/12/14].

[12] E. B. Mathew, U. Jagdeesh, K.P. Henri, B. D. Charlotte, A. G. Crystal, A. W. Sheila, I. V.

Aaron, "Diabetic peripheral neuropathy: How reliable is a homemade1-g monofilament for screening?, " the Journal of family practice. [online]. vol 55. No. 6, pp.505-508, 2006, available: http://www.jfponline.com/fileadmin/jfp_archive/pdf/5506/5506JFP_Article3.pdf

[13] S. R. Shah and K.M. Patil, "Processing of foot pressure images and display of an advanced clinical parameter PR in Diabetic Neuropathy," in Proc. IEEE EMBS-NE, Arlington, VA, 2005, pp. 56-59.

[14] C. Hile, and A. Veves, (2003, December). Diabetic neuropathy and microcirculation. [Online]. 3(6), pp. 446–451. Available: http://download.springer.com/static/pdf/684/art%253A10.1007%252Fs11892-003-0006-0.pdf?auth66=1405185542_9da3fb9347fa1165e1d2003b027ccfe6&ext=.pdf

[15] M. Bharara, J. E. Cobb, D. J. Claremont. (2006). Thermography and thermo-metry in the assessment of diabetic neuropathic foot: a case for furthering the role of thermal techniques. SAGE. 5(4), pp. 250–260. Available: http://ijl.sagepub.com/content/5/4/250.long

[16] G. Bove. (2006, September). Mechanical sensory threshold testing using nylon monofilaments: The pain field's 'Tin Standard'. ScienceDirect. [Online]. 124(1-2), pp 13-17. Available: http://www.sciencedirect.com/science/article/pii/S0304395906003435

[17] B. A. Perkins, D. Olaleye, B Zinman, V. Bril "Simple screening tests for peripheral neuropathy in the diabetes clinic", Diabetes Care. pp. 250-256, 2001.

[18] "Neurometer: Clinical and Research update (2010-2011)".[Online], Pp. 1-9, Available: http://www.neurometer.com/

[19] G. David, N. Singh, Armstrong, A Benjamina, Lipsky. (2005 Jan). "Preventing Foot Ulcers in Patients with Diabetes" The Journal of the American Medical Association Available: http://jama.jamanetwork.com/article.aspx?articleid=200119 [Accessed 04/08/2012].

[20] A. B. Craig, M. B. Strauss, D. Avron, S. S. Miller, "Foot Sensation Testing in the Patient with Diabetes: Introduction of the quick & easy assessment tool", Wounds, vol. 26(8), pp. 221-231, 2014.

[21] A. Nather, S.H. Neo, B.C. Siok, C.F. Stanley. Liew, Y.S. Eileen, L.L. JOCELYN L.L. CHEW (2008). Assessment of sensory neuropathy in diabetic patients without diabetic foot problems, Journal of Diabetes and Its Complications, pp. 126-127.

[22] K.P. Mothiram, B.M. Vasanth, M.B. Mahesh, R. Parivalavan, V.B. Narayanamurthy and V.S. Ganesan, "New Methods And Parameters For Dynamic Foot Pressure Analysis In Diabetic Neuropathy", 19th International Conference IEEE EMBS, Chicago USA, Pp. 1826-1828, Nov. 2, 1997.

[23] N. K. Rana. "Application of Force Sensing Resistor (FSR) in Design of Pressure Scanning", 2009.

[24] J. Jacqueline et al., "A portable insole plantar pressure measurement system," Jour of rehabilitation research and development, vol. 29 (1), pp.13-18, 1992.

[25] L. Shu, T. Hua, Y. Wang, Q. Li, D. D. Feng and X. Tao, "In-Shoe Plantar Pressure Measurement and Analysis System Based on Fabric Pressure Sensing Array," IEEE

Transactions on Information Technology in Biomedicine, vol. 14, no. 3, pp. 767-775, 2010.

[26] S. Solomon, B. Toby, Fundamentals of digital image processing A practical approach with Example in Matlab.

[27] Thomas M. Deserno, "Fundamentals of Biomedical Image Processing" in Biomedical Image Processing (Biological and Medical Physics, Biomedical Engineering),Springer, 2011.

[28] M. Peter, H. Davis, (2013) Learn Raspberry Pi with Linux, Ed. 1st. Berkly/US, aPress.

[29] K. Andreas, A. Mongi, "" in Digital Color Image Processing, Wiley Interscience.

[30] B. P. Michael, F. Lindsay, "A comparison of foot arch measurement reliability using both digital photography and calliper methods", Journal of Foot and Ankle Research, pp. 3/6, (2010).

[31] C. Solomon, T. Breckon, (2011). Fundamentals of Digital Image Processing: A Practical Approach with Examples in Matlab, Wiley-Blackwell, Ed. 1st.

[32] S. Jayaraman, S. Esakkirajan, T. Veerakumar, "Binary Image Processing," in Digital Image Processing, 1st ed., New Delhi: Tata Mc Graw Hill, 2009, pp. 544–545.

[33] R. Edward Dougherty, J. Astola, "Basic Binary Operations ," in An Introduction to Nonlinear Image Processing, 1st ed., Bellingham: SPIE Press. 1994, pp. 6-10.

[34] R. Edward Dougherty, "Statistical Properties of Discrete Morphological Filters," in Mathematical Morphology in Image Processing, 1st ed. vol. (34), New York: Taylor & Francis Inc. 1992, pp. 93-104.

[35] Y. S. Frank "Introduction to Mathematical Morphology," in Image processing and Mathematical Morphology fundamental and applications, 1st ed., NCRC Press. 2009, pp. 1-6.

[36] R. W. Arthur, "Image Geometry and Morphological Filters", in Fundamentals of Electronic Image Processing, IEEE-SPIE: New York, Pp. 294-386, 1998.

[37] H. Zhou, J. Wu, J, Zhang, "Morphological Image Processing" in Digital Image Processing: Part II, pp. 30-61, 2010.

[38] A. Yadav, P. Yadav, "Morphological Image Processing" in Digital Image Processing,1sr ed., Pp. 121-123, 2009.

[39] D. Geoff, Digital Image Processing for Medical Applications, California State University, Channel Islands.

[40] A. Yasrib et. al., "Image Processing in Medical Applications", Journal of Information Technology Impact, vol. 3(2), pp.63-68,2003.

[41] T. Ross, H. Handels, J. Kreusch, H. Busche, H.H. Wolf, S.J. Poppl. "Automatic classification of skin tumors with high resolution surface profiles," in Computer Analysis of Images and patterns, Proc. 4th Int. Conference on Computer Analysis of Images and Patterns, vol. 970, pp. 368-375, 1995.

[42] H. Wang, W. Hsu, K. Guan Goh, M. L. Lee, "An Effective Approach to Detect Lesions in Color Retinal Images" proc. In Computer vision and Pattern recognition, Hilton Head Island, SC, vol. 2, pp. 181-186, 2000.

[43] A. A. A. Al-abayechi, R.Logeswaran X. Guo and W. Tan, "Lesion Border Detection in Dermoscopy Images U sing Bilateral Filter", IEEE International Conference on Signal and

Image Processing Applications (lCSIPA), Melaka, pp. 365-368, 2013.

[44] X. Shen, K. Sun, S. Zhang, "lesion detection of electronic gastroscope images based on multiscale texture feature", Signal Processing, Communication and Computing (ICSPCC), Hong Kong, pp.756-759, 2012.

[45] S.M. S. Ebrahimi, P. Hossein, A. Mohssen, (Nov. 2010). Lesion Detection in Dermoscopy Images Using Sarsa Reinforcement Algorithm, 978-1-4244-7484-4/10/2010 IEEE.

[46] H. Rui, M .Q. Courtney, Z. George, (Sep 2012). Lesion Border Detection in Buruli Ulcer Images, 34th Annual International Conference of the IEEE EMBS San Diego, California USA, 28 August - 1 September, 2012.

[47] How robust is the SVM wound segmentation?

[48] A. Chodorowski, U. Mattsson, M. Langille and G. Hamarneh, "Color Lesion Boundary Detection Using Live Wire, Medical" in proc. Medical Imaging, San Diego, Pp. 1589-1596, 2005.

[49] A. A. A. Al-abayechi, R. Logeswaran, X. Guo and W. Tan, "Lesion Border Detection in Dermoscopy Images U sing Bilateral Filter" proc. In ICSIPA Melaka, Pp. 365-368, 2013.

[50] R. M. Sri, K. M. M. Rao, "Novel Image Processing Techniques to Detect Lesions using Lab View " in proc. IEEE INDICON, Hyderabad, Pp. 1-4, 2011.

[51] N. Szekely and B. Pataki, "Detecting Lesions in a Mammogram" in Proc. 4th EURASIP Conference on Video Image Processing and Multimedia Communications, Zagreb, Crotia, Pp. 113-118, 2003.

[52] C. Artur, G. Tomas and M. Ulf, "Support vector machine for oral lesion classification," IEEE international symposium on biomedical imaging, Pp. 173-176, 2002.

[53] X. Yuan, Z. Yang, Z. George, and M. Nizar, "SVM-based Texture Classification and Application to Early Melanoma Detection, " in proc. IEEE EMBS, New York Pp. 4775-4778, 2006.

[54] B. A. Abdullah, A. A. Younis, P. M. Pattany, E. Saraf-Lavi, "Textural Based SVM for MS Lesion Segmentation in FLAIR MRIs", Open journal of medical imaging, Pp. 26-42, 2011.

[55] http://www.nhs.uk/conditions/Multiple-sclerosis/Pages/Introduction.aspx

[56] N. Abdullah, U. K. Ngah, S. A. Aziz, "Image Classification of Brain MRI Using Support Vector Machine" in proc. IEEE international conference on Imaging systems and techniques, pp.242-247, 2011.

[57] L. Wang, P. C. Pedersen, D. M. Strong, B. Tulu, E. Agu, and R. Ignotz, "Smartphone-Based Wound Assessment System for Patients With Diabetes", IEEE Transactions On Biomedical Engineering, Vol. 62, NO. 2, 477-488, 2015.

[58] E. B. Mathew, U. Jagdesh, K. P. Henri, B. D. Charlotte, A. G. Crystal, A. W. Sheila, I. V. Aaron, "Diabetic Peripheral Neuropathy: How reliable is a homemade 1-g monofilament for screening:", The Journal of Family Practice, Vol. 55, NO 6, pp. 505-508, (June 2006)

[59] K. D. Smith, G. J. Emerzian, O. Petrov, "A comparison of calibrated and non-calibrated 5.07 nylon monofilaments," Foot Ankle Int. vol. 21(10), pp. 852-855, 2000.

[60] R. Yong, T. J. Karas, K. D. Smith, O. Petrov, "The durability of the Semmes-Weinstein 5.07 monofilament," Jour. Foot Ankle Surgery, vol. 39(1), pp. 34-38, 2000.

[61] Y. Itsarachaiyot, J. Suthakorn, C. Guerineau, S. Vera, W. Sirisopha and C. Wilasrusmee.

"Development of A Novel Robotic Monofilament Probe for Diabetic Neuropathy Screening", Asian Journal of SurgeryVolume 33 , Issue 4, October 2010,pp. 193–198, 2009.

[62] G. Venugopal, J. P. Biren, K. Rajanna and M. M. Nayak, "Multi-point Sensing System for Plantar Pressure Measurement", IEEE SENSORS Conference, Atlanta GA, Pp. 978-981, Oct. 2007.

[63] MacWilliams, B.A.; Armstrong, P.F. Clinical Applications of Plantar Pressure Measurement in Paediatric Orthopaedics. In Proceeding of Paediatric Gait, 2000. A New Millennium in Clinical Care and Motion Analysis Technology, Chicago, IL, USA, 22 July 2000; pp. 143–150.

[64] A.H.A Razak, Z. Aladin, K.B. Rezaul, and W. Yufridin, "Foot Plantar Pressure Measurement System: A Review", in Sensors, 2012, pp. 9884-9912

[65] R. P. Betts, T. Duckworth, "A Device For Measuring Plantar Pressures Under The Sole Of The Foot", Engineering in Medicine, Vol 7 no. 4, Pp. 223-228, Oct. 1978.

[66] R. M. Queen, A. N. Abbey, J. I. Wiegerinck, J. C. Yoder, J. A. Nunley, "Effect of shoe type on plantar pressure: a gender comparison", Gait Posture, Vol. 31, Issue 1, Elsevier, January 2010, Pp. 18–22.

[67] R. L. William, J. B. Shofer, M. S. Cowley, J. H. Ahroni, V. Cohen, J. B. Edward, "Diabetic foot ulcer incidence in relation to plantar pressure magnitude and measurement location", Vol. 27, Issue 6, Elsevier, December 2013, Pp. 621–626.

[68] A. Gioftsidou, P. Malliou, G. Pafis, A. Beneka, G. Godolias, C.N. Maganaris, "The effects of soccer training and timing of balance training on balance ability", European Journal of Applied Physiology, Vol. 96, Issue 6, Springer Link, April 2006, Pp. 659-664.F

[69] Plantar pressure distribution measurements technical background and clinical applications.

[70] B. L. Davis, R. M. Cothren, P. Quesada, S. B. Hanson, J. E. Perry, "Frequency content of normal and diabetic plantar pressure profiles: implications for the selection of transducer sizes", Journal of Biomechanics, vol. 29(7) pp.979-983, 1996.

[71] A. Gefen, "Pressure-sensing devices for assessment of soft tissue loading under bony prominences: Technological concepts and clinical utilization", in Wounds, 2007, Vol. 19, 350–362.

[72] G. V. Zammit et al., "Reliability of the TekScanMatScan® system for the measurement of plantar forces and pressures during barefoot level walking in healthy adults," Jour. of foot and ankle research, vol. 3, 2012.

[73] J. K. Gurney, et al., "Between-day reliability of repeated plantar pressure distribution measurements in a normal population," Gait and Posture, vol. 27, pp. 706-709, 2008.

[74] A. Meyring, et al., "Dynamic plantar pressure distribution measurements in hemiparetic patients", Clinical Biomechanics, vol. 12, No.1, pp. 60-65, 1997.

[75] Cousins, et al., "The reliability of plantar pressure assessment during barefoot level walking in children aged 7-11 years," jour. Of foot and ankle research, vol. 1, pp 1-8, 2012.

[76] G. V. Zammit et al., "Reliability of the TekScanMatScan® system for the measurement of plantar forces and pressures during barefoot level walking in healthy adults," Jour. Of foot

and ankle research, vol. 3, 2012.

[77] A. Agić, V. Nikolić, B. Mijović, (2006, Dec). Foot anthropometry and morphology phenomena. CollAntropol. [Online]. 30(4), pp.815-821. Available: http://www.ncbi.nlm.nih.gov/pubmed/17243556.

[78] F. T. Cheng, D. B. Perng, (1999, Nov). A systematic approach for developing a foot size information system for shoe last design. [Online]. 25(2), pp.171-185. Available: http://www.sciencedirect.com/science/article/pii/S0169814198000985.

[79] L. Vern, C. Thongpop, (n.d) Footwear Study, NYU School of Medicine Preventing Rehabilitation Engineering Research Center: http://www.med.nyu.edu/rehabengineering/research/usmilfootwearstudy.html [Accessed 04/08/2013].

[80] T. G. McPoil, B. Vicenzino, M. W. Cornwall and N. Collins, (2009, Oct). Can foot anthropometric measurements predict dynamic plantar surface contact area?, J Foot Ankle. [Online]. 2(1). Available: http://www.ncbi.nlm.nih.gov/pmc/articles/PMC2936827/.

[81] B. Y. S. Tsung, M. Zhang, Y. B. Fan, D. A. Boone, (2003, Dec). Quantitative comparison of plantar foot shapes under different weight-bearing conditions, JRRD. [Online]. 40(6), pp. 517-526. Available: http://www.rehab.research.va.gov/jour/03/40/6/Tsung.html.

[82] G. Oladipo, I. Bob-Manuel, G. Ezenatein: Quantitative Comparison Of Foot Anthropometry Under Different Weight Bearing Conditions Amongst Nigerians. The Internet Journal of Biological Anthropology. 2009 Volume 3 Number 1. DOI: 10.5580/90e.

[83] S. C. Cobb, C. R. James, M. Hjertstedt, J. Kruk "A Digital Photographic Measurement Method for Quantifying Foot Posture: Validity, Reliability, and Descriptive Data", Journal Of Athletic Training. Pp 20-30, (Jan 2011).

[84] N. A. Mall, W. M. Hardaker, J. A. Nunley, R. M. Queen, "The reliability and reproducibility of foot type measurements using a mirrored foot photo box and digital photography compared to caliper measurements", National Center for Biotechnology Information. Vol. 40(6), (Jul. 2007).

[85] T.G. McPoil, M. W. Cornwall, M Lynn, V. Bill, F.Kelly.,H. Dana, "Arch height change during sit-to-stand: an alternative for the navicular drop test", National Centre for Biotechnology Information. Vol. 1, pp. 3, (May 2009).

[86] I. Pitas, "Digital Image Processing Algorithms and Applications", John Wiley and Sons Ltd, (2000).

[87] H. R. Siddiqui, S.R. Alty, S. M. Spruce, Sandra E. Dudley,(Jan 2013) 'Automated Peripheral Neuropathy Assessment of Diabetic Patients using Optical Imaging and Binary Processing Techniques', International IEEE Conference on IEEE Point-of-Care Healthcare Technologies (PHT) Bangalore, India, 16 - 18 January, 2013.

[88] E. Upton, G. Halfacree, "Connecting the Board" in Raspberry Pi User Guide, 2nd Ed. John Wiley & Sons, 2014.

[89] http://euspyshop.com/ion-copy-cat-handheld-document-scanner-wand-153-p.asp [Accessed 04/03/2014].

[90] NICE. (2014, Apr.). Pressure ulcers: Prevention and management of pressure ulcers.

[Online]. Available: http://www.nice.org.uk/guidance/cg179resources/guidance-pressure-ulcers-prevention-and-management-of-pressure-ulcers-pdf.

[91] G. M. Bove, "Mechanical sensory threshold testing using nylon monofilaments:The pain field's 'Tin Standard'," Int. Assoc. Study Pain, vol. 124, pp. 13–17, 2006.

[92] B. Garry, K. Adrian, "Learning opencv computer vision with opencv library", Newgen Publishing and Data Services, Ed. 1st. 2008.

[93] Paul, (1988) [WWW] Calculating the area and centroid of a polygon Available from: http://paulbourke.net/geometry/polyarea/ [Accessed 01/08/12].

[94] W. Burger, M. J. Burger., (2008), Digital Image Processing: An Algorithmic Introduction Using Java, Springer, pp. 239.

[95] Y. Liu, G. Chen, M. Ying, (July 2005), Fuzzy Logic, Soft Computing and Computational Intelligence, V 2, pp. 1020-1021.

[96] A. C. Frery, T. Perciano, "Image Data Formats and Color representation," in Introduction to Image Processing Using R 1st Ed., vol. 1, Springer, NewYork, (2013, February), pp. 22.

[97] B. S. D. Sagar, "Mathematical Morphology: An Introduction," in Mathematical morphology in Geomorphology and GISci, 1st Ed. vol. 1, New York: Chapman & Hall/CR, 2013, pp. 32.

[98] N. Habili et al., "Segmentation of the Face and Hands in Sign Language Video Sequences Using Color and Motion Cues," IEEE Trans. on Circuits and Sys. for Video Technology, vol. 14(8), pp. 1086-109, 2004.

[99] Tim D. Jones and Peter Plassmann, (Dec. 2000). An Active Contour Model for Measuring the Area of Leg Ulcers, IEEE Transaction on Medical Imaging, Vol. 19, No. 12.

[100] A. P. Dhawan, B. Alessandro, S. Pawardhan, and N. Mullani, "Multispectral Optical Imaging of Skin-Lesions for Detection of Malignant Melanomas", IEEE EMBS Conference, NJ, pp. 5352-5355, (September 2009).

[101] A. A. A. Al-abayechi, R. Logeswaran, X. Guo, and W.H. Tan, "Lesion Border Detection in Dermoscopy Images Using Bilateral Filter",IEEE International conference on Signal and Image Processing Application (ICSIPA), pp 365-368, Melaka (October, 2013).

[102] X.Yuan, Z. Yang, Z. George, and M. Nizar, "SVM-based Texture Classification and Application to Early Melanoma Detection, " in proc. IEEE EMBS, New York Pp. 4775-4778, 2006.

[103] X. Shen, K. Sun, and S. Zhang, "Lesion Detection Of Electronic Gastroscope Images Based On Multiscale Texture Feature", IEEE International conference on Signal processing, Communication and Computing (ICSICC), pp 756-759, Hong Kong(2013).

[104] Z. Zhang, W. V. Stoecker, and R. H. Moss, "Boarder detection on digitized skin tumour mages", in IEEE Trans. Med. Imaging, 19(11), pp.1 128-1143, 2000.

[105] T.D. Jones, "Improving the precision of leg ulcer area measurement with active contour models", PhD thesis, University of Glamorgan, 2000.

[106] M. Kolesnik and A. Fexa, "Segmentation of wounds in the combined color-texture feature space", in Proc. of SPIE Medical Imaging 2004: Image Processing, February, 2004, San Diego, CA, pp. 549-556.

[107] T. Ojala, M. Pietikainen, and D. Harwood, "A Comparative Study of Texture Measures

with Classification Based On Feature Distributions," Pattern Recognition, Vol. 29, No. 1, pp. 51-59, 1996.

[108] M. Pietikainen, A. Hadid, G. Zaho, T. Ahonen, "Local Binary Pattern for Still Images" in Computer Vision Using Local Binary Pattern,Vol 40, Springer Link, London, pp. 13-47, 2011.

[109] Z. Li, G. Liu, Y. Yang, and J. You, "Scale- and Rotation-Invariant Local Binary Pattern Using Scale-Adaptive Texton and Subuniform-Based Circular Shift", IEEE Transaction On Image Processing, Vol. 21, NO.4, pp. 2130-2140, April 2012.

[110] E. Issam, Y. Yang, M.N. Wernik, N. P. Galatsanos, R.M.Nishikawa, "A Support Vector Machine Approach for Detection of Microcalcifications", IEEE transaction on Medical Imaging, Vol.21, NO. 12, December 2002.

[111] O. Chapelle, P. Happner, and V.N. Vapnik, "Support Vector Machine for Histogram-Based Image Classification", IEEE transaction on Neural Network, Vol 10, NO. 5, pp.1055-1064, 1999.

[112] X. Uan, Z. Yang, Z. George, N. Millani, "SVM-based Texture Classification and Application to Early Melanoma Detection", IEEE EMBS conference proceeding, New York, pp.4775-4778.

[113] footscan®PLATES, Available from: http://www.rsscan.co.uk/systems.php [Accessed 15/06/15].

[114] I. Song, J. Bae, S. Y. kim "An Overview to Signal detection theory" in Advanced Theory of Signal Detection Weak Signal Detection in Generalised Observations,1st ed., Pp. 3-6, 2002.

[115] S. E. R. Kurpius, M. E. Stafford, "Reliability-The same Yesterday, Today, and Tomorrow" in TESTING and MEASUREMENT A User-Friendly Guide,1st ed., Pp. 121-140, 2005.

[116] J. Clifford, M. James, M. Mark, "Sensory Threshold of Normal Human Feet", FOOT & ANKLE International, Vol 21(6), Pp.501-4, jun (2000).